Alma Mater Studiorum - Università di Bologna

SCUOLA DI INGEGNERIA

DIPARTIMENTO DI INGEGNERIA DELL'ENERGIA ELETTRICA E DELL'INFORMAZIONE "GUGLIELMO MARCONI"

MASTER'S DEGREE IN ELECTRIC VEHICLE ENGINEERING

MASTER THESIS

in

Automotive Power Circuits and Electric Motor Design

Optimized Finite Element Mapping of Multiphase Bearingless Motors

Candidato:
Luca Malagoli
Mat. 0001102710

Relatori:
Prof. Giacomo Sala

Correlatori:
Prof. Michele Degano
Ing. Gabriele Antonino Cagliari
Dr. Lorenzo Carbone
Dr. Meiqi Wang

Session III
Academic year 2024/2025

A Mario,
alla genialità che lo avrebbe reso
curioso anche di questo lavoro.

Abstract

The current state of the art suggests the adoption of three-phase electrical drives in most industrial and automotive applications. However, studies report that by introducing even more motor phases, it is possible to obtain higher efficiency, increased power density, and enhanced controllability. In this context, multiphase bearingless electric machines represent an innovative solution in the field of electric drives, combining torque production and active control of radial forces for rotor magnetic suspension. These features allow multiphase electric drives to be employed in several industrial applications requiring precise control, high efficiency, and reliability. Consequently, an accurate design validation process is essential to ensure consistent and satisfactory performance. Before prototyping, this validation typically relies on electromagnetic simulations performed with finite-element software, often involving thousands of computationally intensive runs. This work aims at increasing the efficiency of the design stage by reducing the computational effort required for the full finite-element simulation of a bearingless permanent magnet machine, thereby enabling the generation of look-up tables for control simulations with minimal resource usage. After an introductory overview of multiphase and bearingless machines, a detailed analysis of the electromagnetic mapping of multi-sector surface-mounted permanent magnet motors is developed, considering also the effects of eccentricity on the machine under analysis. Strategies for the reduction of computational load are then proposed and evaluated, achieving a significant reduction in terms of simulation time and number. However, further studies and experimental validation remain necessary to fully assess the accuracy and reliability of the proposed approach in real-world applications.

Contents

List of Figures

Chapter 1

Introduction

1.1 Overview of Multiphase Electric Machines

Multiphase electric machines represent a natural evolution of traditional machines when they are no longer directly connected to the standard three-phase grid, allowing an arbitrary number of phases $n > 3$ to be chosen as a design variable. Each additional phase introduces an extra degree of freedom, which can be exploited to implement more complex controls, increasing performance, reliability and control flexibility [10].

An intrinsic advantage of multiphase machines is the possibility of distributing the total power between several phases, reducing the load on each electronic component of the single converter, that can be modularized into more separate units. For example, a three-phase double-layer machine with two series-connected coils per phase can be reinterpreted as a six-phase machine, powered by two independent three-phase converters, halving the required voltage or current load on the switching devices (Figure 1.1). This approach is advantageous for both high-power applications (electric marine propulsion, turbo-compressors) and low-voltage applications. Multiphase systems can be combined with multilevel converters for further benefits in the sizing of power electronic devices. The aerospace industry aims to significantly reduce CO_2 and NO_x emissions, external noise and environmental impact throughout the entire life cycle of aircraft, prioritizing the increase of efficiency in propulsion and auxiliary systems: developing hybrid-electric and fully electric aircraft could help halve the carbon footprint by 2050.

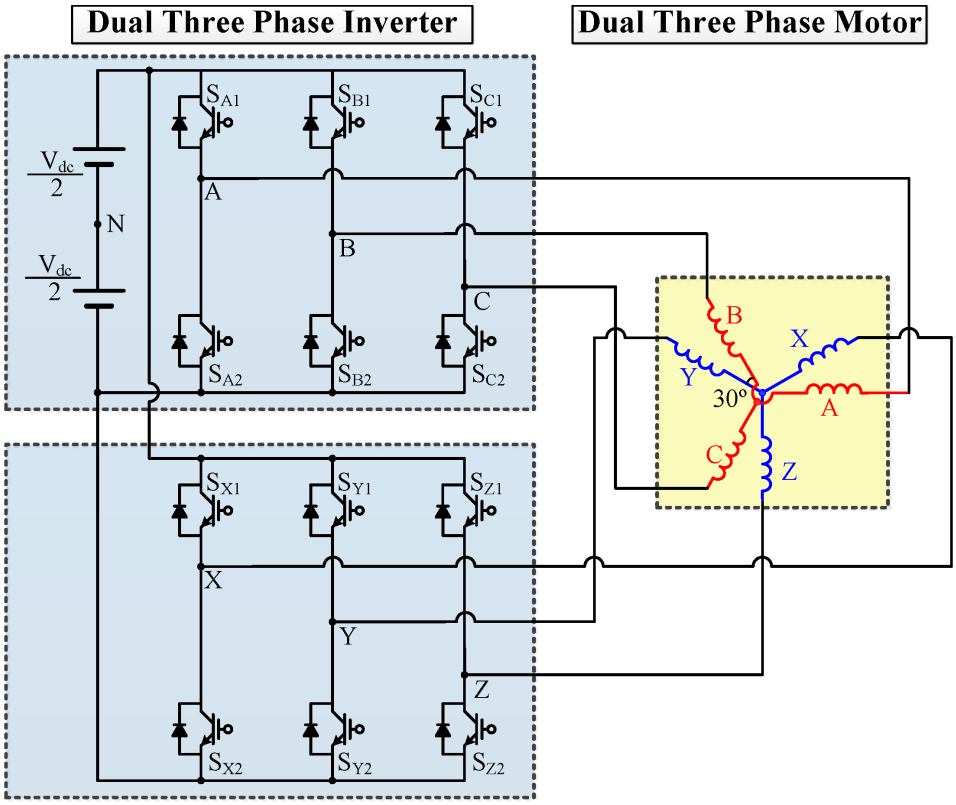

Figure 1.1: Example of dual three-phase machine [1].

The electrification of aircraft makes the reliability and efficiency of the onboard electrical network, generators and drive systems crucial, stimulating numerous university and industrial projects such as More Electric Aircraft (MEA), More Electric Engine (MEE) and All Electric Aircraft (AEA), and European programmes such as Clean Sky, aimed at reducing emissions and noise through electric motors and advanced electrical systems [11].

The transition to multiphase machines requires a rethinking of the design and control of currents. The additional phases can be strategically positioned, often in completely new winding configurations, to inject more independent currents and control more harmonics of the magnetic field in the air gap.

In three-phase machines, the star connection limits the number of independent currents to two, while in a multiphase machine with a single star connection, the independent currents are $m - 1$, and with multiple stars, $m - N_{\text{star}}$ [11]. This allows additional magnetic field harmonics to be controlled, improving performance and reducing ripple and noise. The instantaneous distribution of the magnetomotive force depends on the position of the phases and the currents in each phase. In multiphase designs, the aim is to maximize fundamental harmonics and minimize non-fundamental harmonics, often exploiting higher harmonics through current harmonic injection techniques to increase average torque, reduce ripple and minimize losses and noise. Increasing the number of phases of a symmetrical winding layout is unarguably the most elegant option to allow the

independent production of multiple controllable magnetomotive force (MMF) harmonics [12]. This is particularly important in aeronautical and naval applications, where reliability and stability are priorities.

Multiphase machines offer internal redundancy: in the event of a phase failure, the other phases can compensate for the missing power, minimizing performance loss and preventing complete machine failure. The main faults include:

- high resistance connections, open circuits, short circuits in the coils;
- rotor eccentricity, bearing failures, demagnetization of permanent magnets;
- sensor failures.

Open-circuit management in three-phase systems is well established, often through the coordinated opening of all inverter branches, but in advanced multiphase machines it is possible to maintain appropriate currents in healthy phases to improve fault tolerance. The management of more complex faults, such as demagnetization or rotor defects, still requires sophisticated control and modeling methodologies [5].

In summary, multiphase machines allow for the design and control of electrical systems that are more efficient, reliable and flexible than traditional three-phase machines, making them particularly suitable for critical applications such as marine propulsion, electric vehicles and electric aircraft.

1.2 Bearingless Multiphase Machines

Electric machines capable of simultaneously generating torque and controlled suspension forces represent one of the most promising solutions for high-speed applications, in extreme environments or in systems where the use of mechanical bearings is problematic or undesirable. In this context, bearingless permanent magnet synchronous machines (BEL-PMSM) are a category of growing interest, as they integrate both the function of a rotary actuator and that of an active magnetic suspension device into a single structure [13]. Through appropriate control of the stator currents, these machines are capable of simultaneously developing the driving torque and the two-dimensional radial forces that allow the rotor to levitate, eliminating the need for mechanical contacts. The main advantages offered by bearingless technology include:

- elimination of friction and lubrication;
- elimination of mechanical wear and the need for periodic maintenance;
- greater compatibility with sterile chambers or high-cleanliness environments;
- a significant increase in motor service life;

- the possibility of reaching very high speeds without constraints imposed by structural resonances or critical limits due to mechanical bearings.

These characteristics make BEL-PMSMs suitable for a wide range of applications, from turbomachinery to microfluidics and from medical pumps to high vacuum systems. Since there is no mechanical component to sustain the rotor in the stator reference frame, the motor will be prone to eccentricity: this word is used to describe the eventuality in which the rotor axis does not coincide with the stator axis, a common event also for conventional machines.

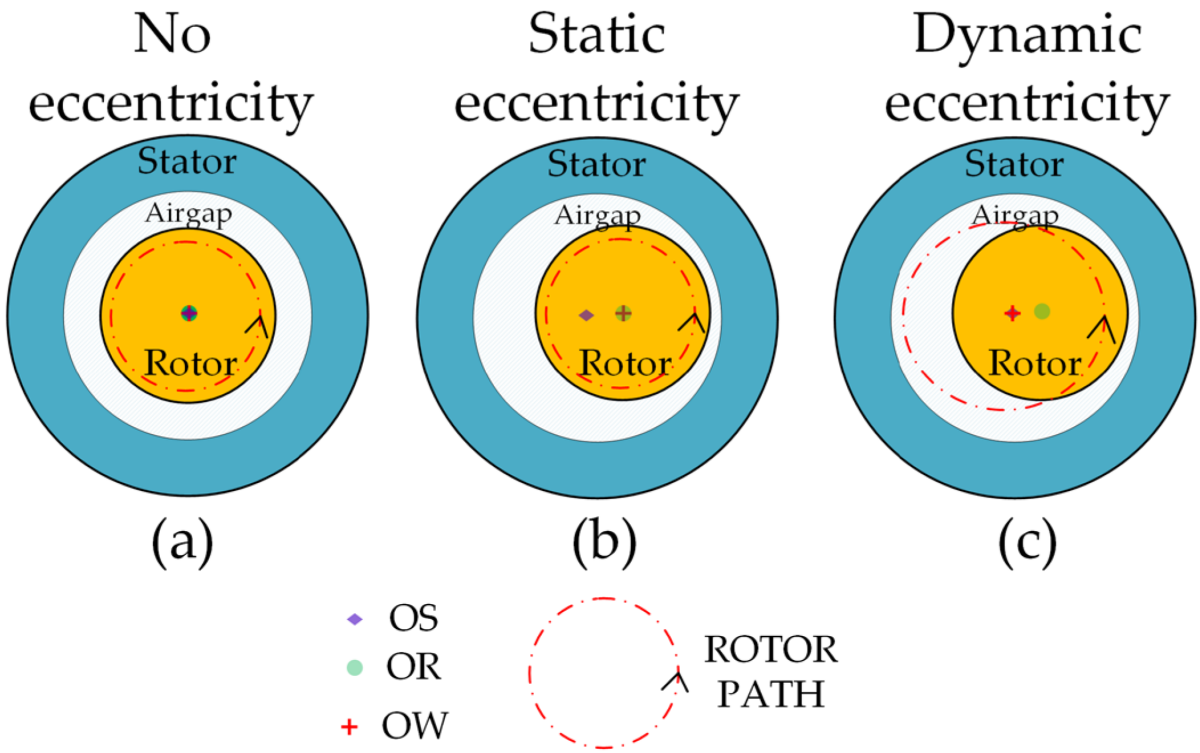

Figure 1.2: Static (a) and dynamic (b) eccentricity [2].

The rotor eccentricity can be either static or dynamic, depending on whether the displacement between the rotor and stator centres is constant or whether it is moving (usually spinning along a circular path with the same speed as the rotor). Figure 1.2 shows the difference between static and dynamic eccentricity: eccentricity can be caused by a not-perfect rotor centering during the manufacturing process, an inaccurate rotor balancing, stator ovality, or a misalignment introduced in the manufacturing process. In conventional machines, the rotor eccentricity can result in a reduced lifetime of the machine due to bearings wear and additional mechanical stresses on the rotating components.
Rotor eccentricity causes non-uniform airgap flux density distribution, and subsequently the development of electromagnetic forces between the rotor and stator [10].

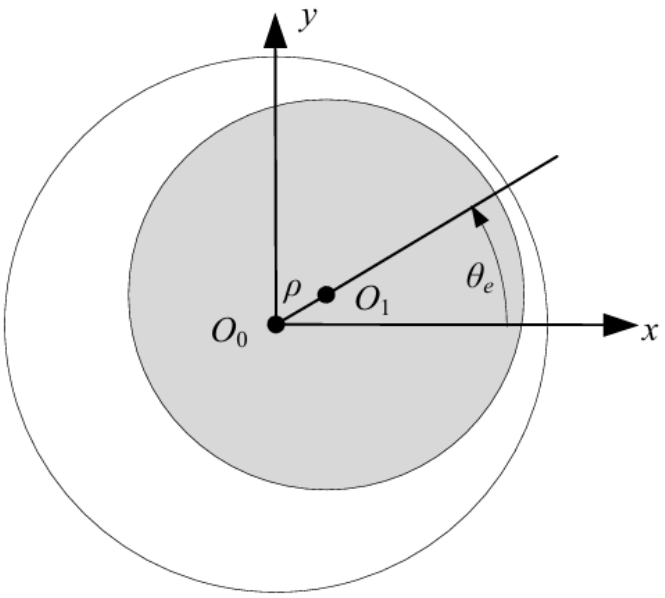

Figure 1.3: Rotor eccentricity model [3].

This undesired disturbance, known as unbalanced magnetic pull (UMP), can also be caused by the combination of poles and slots number, and can damage the rotor in case of collision with the stator frame. When the motor is eccentric, the airgap can be computed, referring to Figure 1.3, as:

$$g(\theta_m) = g_0 - \rho cos(\theta_m - \theta_\epsilon) \tag{1.1}$$

Where ρ is the eccentric distance of the motor, which will be called "eccentricity radius" r_ϵ in this thesis work, θ_ϵ is the eccentricity angle, and θ_m is the rotor mechanical angular position.

Usually, stable control needs radial displacement sensors, as will be shown in 5, while self-sensing methods eliminate physical sensors, which makes the hardware less complicated, the system cheaper, and improves reliability [4]. Self-sensing (sensorless) state estimation of bearingless motors depends on non-zero rotor x and y displacements that change the machine's electromagnetic properties: by carefully exploiting the winding terminal voltages and phase currents, advanced algorithms can figure out the unmeasured displacement state. The first implementations of bearingless machines were based on a clear separation of the two mechanisms for generating electromagnetic quantities: a winding dedicated to torque production (motor winding) and a second independent winding for developing suspension forces (suspension winding) [12].

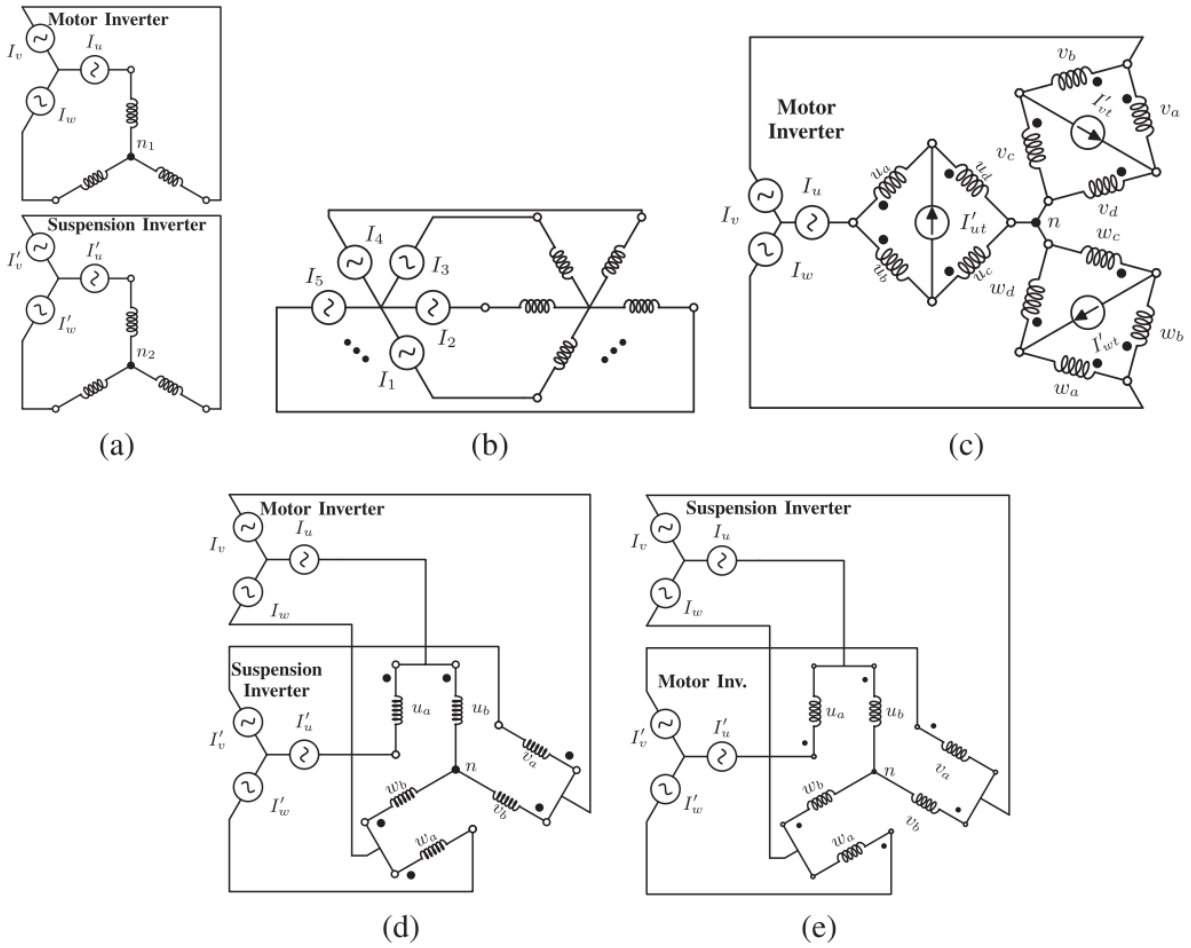

Figure 1.4: Bearingless winding topologies: (a) separated, (b) multiphase, (c) bridge, (d) parallel DPNV, and (e) mid-point current injection (MCI) [4].

Although this approach allowed good independent control of the two functions, it resulted in a significant increase in size, construction complexity, and the amount of copper required. Furthermore, the use of two separate power converters increased costs and potential points of failure. To address these limitations, more compact topologies have been introduced, such as bridge or parallel configuration windings, dual-purpose no-voltage (DPNV) windings, and multiphase solutions divided into stator sectors. Among these, multi-three-phase architectures, consisting of multiple electrically independent three-phase sets distributed in sectors along the stator, are particularly relevant ([8], [5]). In these configurations, each sector is capable of contributing to both torque and radial force generation, giving the system high redundancy and natural fault tolerance.

The multiphase approach has numerous advantages:

- reduced overall dimensions, thanks to the elimination of dedicated windings;
- possibility of using standard three-phase inverters for each sector;
- greater modularity, which facilitates maintenance and scalability;

- excellent fault tolerance, which allows operation to continue even in the event of the loss of one or more sectors;
- possibility of managing torque, power, and radial forces separately, distributing them among the various modules.

Accurate determination of the radial forces produced by the machine is one of the main challenges in the design and control of BEL-PMSMs, especially in the presence of multiphase or multi-sector architectures. The waveform of the magnetic field in the air gap is influenced by numerous factors: the geometry of the rotor, the distribution of the windings, the magnetizing action of the stator currents, the presence of mechanical eccentricities, and the saturation effects of the magnetic circuit.

Simplified analytical models, often used in the early stages of study, assume a linear relationship between current and radial force, neglecting rotor eccentricity or load effects. Such models provide useful insight into the dynamics of the system, but are not adequate in real operating conditions or at high speeds, where the interaction between the spatial harmonics of the magnetic field becomes significant. More advanced methodologies use Maxwell's stress tensor (MST) to calculate the magnetic pressure distribution along the stator perimeter, thus obtaining accurate models of radial force even in the presence of eccentricity, non-sinusoidal currents, and strong interactions between sectors [3].

The integration of MST along the circumference of the stator allows a clear link to be established between the current profile in the various windings and the generation of force in the $x - y$ reference frame, thus enabling the development of high-precision control strategies.

Further complexities arise from the need to generate torque and force simultaneously through the same winding system. This inevitably leads to electromagnetic couplings between the two phenomena, making it difficult to achieve complete decoupling between the effects of torque and those of suspension [14]. Differences in rotor position, magnetization, or machine parameters can cause variations in the direction of application of radial force, generating tracking errors or instability if not adequately compensated.

1.2.1 Design and control aspects of Multiphase Bearingless Machines

Multiphase machines offer the opportunity to implement advanced control strategies thanks to the possibility of managing multiple independent current vectors. Three fundamental functions are required in bearingless systems [15]:

1. generation of driving torque for speed or angular position control;

2. generation of radial forces in the two orthogonal axes;

3. compensation of dynamic disturbances and attenuation of vibrations.

The most common approaches are two: the first one, called Pseudoinverse Matrix Method (PIM), exploits the Moore–Penrose pseudoinverse of the machine model matrix formulation to obtain the $\alpha - \beta$ reference currents that generate the required force and torque, while minimizing the Joule losses; the second one exploits the Space Vectors technique to generate appropriate magnetic field harmonics for both torque (order p) and radial force generation ($p+1$ and $p-1$). Both the mentioned methods aim at achieving a two degrees of freedom bearingless operation [16]. The presence of multiple independent three-phase systems also allows the implementation of fault-tolerant control strategies. In the event of a single-phase open-circuit (SPOC) or three-phase open-circuit (TPOC), it is possible to redistribute the current components among the remaining sectors, maintaining both levitation and motor capacity, while limiting torque and force ripple even under conditions of saturation or reduced current capacity [9]. Another area of development concerns active vibration control: multiphase machines can be used not only for levitation but also for the suppression of residual mechanical vibrations in systems still equipped with traditional bearings, thanks to the controlled application of multiple independent radial forces[15]. This approach is particularly useful in high-speed applications, where exceeding critical frequencies can cause significant instability.

The magnetic complexity and strong interdependence between torque and force generation make the BEL-PMSM design process an inherently multi-objective problem. Modern design workflows typically include a combination of:

- simplified analytical models to quickly explore the design space;
- multi-objective optimizations based on evolutionary algorithms or surrogate techniques;
- high-fidelity FEM simulations for validating candidate solutions.

It is possible to qualitatively state that the torque of the considered motor is generated in the same way as a standard three-phase PMSM, with the only difference being that each sector winding contributes $\frac{1}{n_s}$ to the total torque, being n_s the number of sectors of the machine. Furthermore, independently controlling the current in each sector enables the flux density distribution of the air gap to be unbalanced, producing a net radial force. It is also interesting to examine the principles of torque and force generation by analyzing the interactions between the different spatial harmonics of the magnetic field in the air gap. To produce a net torque in a PM machine, the harmonic orders of the armature and PM fields have to be identical. The main PM mechanical harmonic order, n_{PM}, is usually

related to the number of pole pairs (p). On the other hand, controllable radial force can be produced by commanding a magnetic field of mechanical order $n_w = n_{PM} \pm 1$ [10].

The main objectives deserve careful balancing:

- maximization of torque density;
- maximization of radial force generation capacity;
- minimization of unwanted coupling between torque and force;
- reduction of losses and increase in overall efficiency;
- implementation of modularity and fault tolerance;
- compatibility with advanced control strategies.

Different combinations of number of poles, phase distribution, winding pitch, and spatial harmonics generated by the sectors can, in fact, favor torque production over force production or vice versa, significantly influencing control complexity, fault robustness, and the quality of the forces produced.

1.3 Machine under study

A conventional 18-slot, 6-pole, surface-mounted permanent magnet synchronous machine (PMSM) was available at the Power Electronic and Machines Centre (PEMC) facilities at the University of Nottingham. It features three single-layer full-pitch distributed three-phase windings, with independent star connections, located 120 mechanical degrees apart in three stator *sectors* ($n_s = 3$): within each sector, phases v and w are located $\mp$ 20 mechanical degrees apart from phase u. In this work, for the sake of simplicity and brevity, phases $u_1, v_1, w_1, ..., u_3, v_3, w_3$ will be indicated with the correspondent number from 1 to 9. Featuring 18 slots, 3 pole pairs and 9 phases, 3 for each sector, the number of slots per pole per phase is $q = 1$.

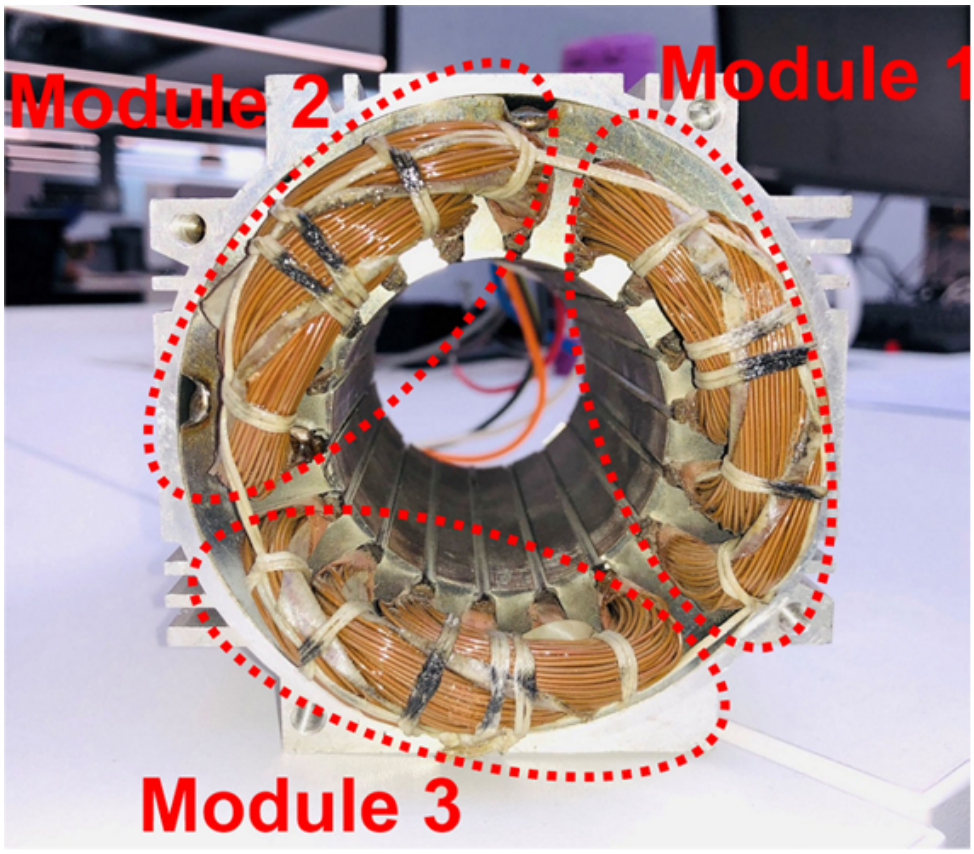

Figure 1.5: Stator of the analyzed machine, with focus on winding arrangement [5].

The magnets are surface-mounted and radially magnetized. Surface-mounted PMSMs are well known for their high efficiency and power density, and are widely investigated for bearingless applications due to their relatively simple control system. [10].
The specifics of the machine are presented in Table 1.1 and the stator structure is shown in Figure 1.5, highlighting the winding layout. Figure 1.6 shows a cross-section of the machine in question, including the rotor and highlighting the magnetic axes of the machine phases.

MACHINE PARAMETERS			
Pole number	$2p$	6	–
PM material	–	NdFeB	–
PM remanence flux density	B_{res}	1.24	T
PM relative permeability	μ_r	1.031	–
Power rating	P_{nom}	1.5	kW
Peak current	I_{rated}	20	A_{pk}
Rated speed	n_{rated}	3000	rpm
Turn/coil	N_c	22	–
PM flux of one sector	${}^s\Lambda_{PM}$	0.0284	Wb
Torque constant	k_T	0.128	Nm/A
Line-to-line voltage constant	k_V	15.5	V/krpm
Outer stator diameter	–	95	mm
Inner stator diameter	–	49.5	mm
Axial length	l	90	mm
Airgap length	g_0	1	mm
Magnet thickness	h_m	4	mm

Table 1.1: Machine parameters used in the model

The signs + and - in front of the phase labels indicate, respectively, current flowing out of and into the plane, while the magnetic axes are represented in terms of their angular position in mechanical radians. From this detail, it's interesting to notice that the magnetic axis of the phase u of each sector is represented with a positive sign, conversely to the rest of the sector phases (Fig. 1.6b), due to the winding configuration: for this reason, the flux generated by the exact same current flowing in phase v or w will have the opposite direction with respect to the one obtained by feeding u [6]. Each of the three-phase sectors has a full-pitched distributed winding with an isolated star point, that provide six degrees of freedom for currents control. The left superscript s will be adopted to denote the quantities related to the single s^{th} sector. The machine under investigation has a number of sectors $n_s = p$, where p is the pole pairs number.

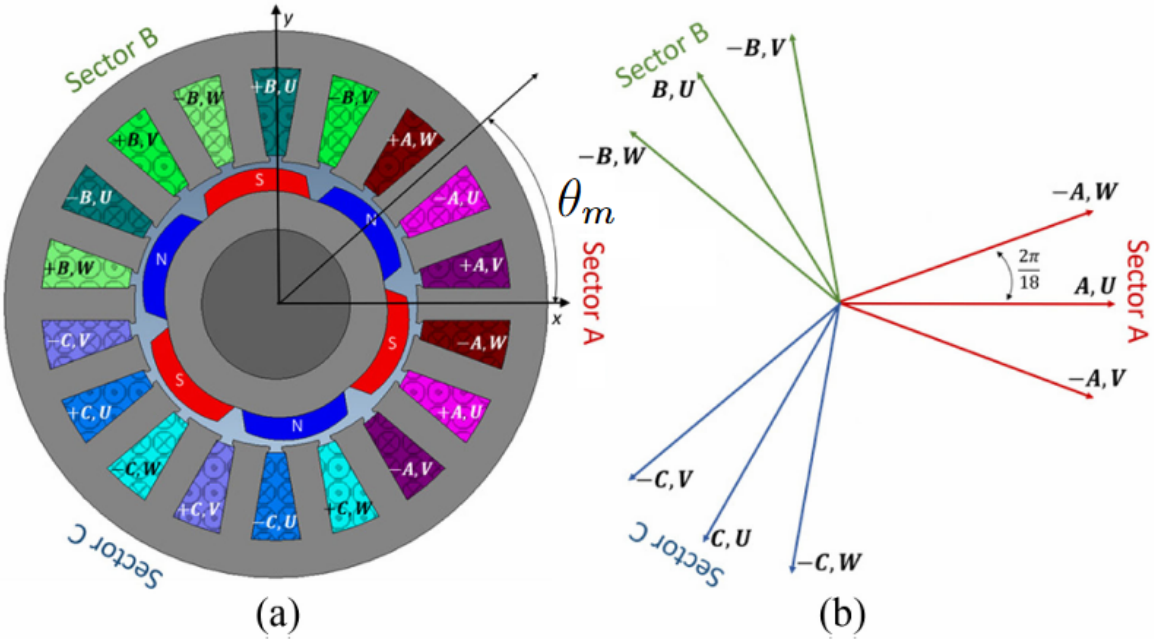

Figure 1.6: Radial cross-section of the multi-sector SPM machine (a), and the magnetic axes of the nine phases (b) [6].

The angular position of the generic sector s with respect to the x axis is given by

$$^{s}\gamma = (s-1)\frac{2\pi}{n_s} + \gamma_0 \tag{1.2}$$

where γ_0 defines the angular position of the magnetic axis of sector 1 with respect to the x-axis; for this machine, as shown in Figure 1.6, it is 0°.
According to the literature sources that dealt with the machine under analysis, the rotor is axially divided into three segments, with a skewing angle equal to half a slot pitch.

$$\alpha_{skew} = \frac{\alpha_{slot}}{2} = \frac{\frac{360}{18}}{2} = 10^{\circ} \tag{1.3}$$

According to the available information, the second and third rotor segments were assumed to be shifted by 5° and -5°, respectively, relative to the first segment. As previously mentioned, the radial forces are generated by unbalancing the flux density at the airgap, by acting on the d-axis currents. For example, since $\gamma_0 = 0°$, strengthening the flux density in the airgap facing sector 1, while weakening it in correspondence with sectors 2 and 3, produces a resultant force in the positive x-axis direction. In the analyzed machine, where $p = 3$, the interaction of the third PM field harmonic with the second and fourth armature magnetic field harmonics produces the radial force. An important feature of this machine is indeed the absence of bearings sustaining the rotor during motor operation, but it's paramount to specify that a backup bearing at the shaft is present to sustain the rotor while the machine is not operating, and prevent damaging the magnets due to collision

with the stator frame. Such a toroid-shaped bearing, which limits the shaft displacement with respect to the stator axis on the $x - y$ plane, causes the maximum rotor eccentricity to be r_ϵ=150 μm, corresponding to 15% of the mechanical airgap thickness $g_0 = 1$ mm.

Chapter 2

Electromagnetic model of the machine under study

2.1 Machine mapping wiht FEMM

In the context of this work, mapping a motor refers to the action of defining its behaviour, focusing on two main aspects:

1. Wrench vector, composed by radial forces on the $x-y$ plane and produced torque, which will be represented as
$$W = [F_x, F_y, T]^T \tag{2.1}$$

2. Linked fluxes on each phase, and consequently the resulting inductance matrix. The result of the mapping procedure is a 9x9 inductance matrix L. Such matrix will not be circulant due to the winding arrangement, that is not spatially symmetric [8]. The phase matrix inductance L_{ph} of the triple three-phase SPMSM can be represented as
$$L_{ph} = \begin{bmatrix} L & M & M \\ M & L & M \\ M & M & L \end{bmatrix} \tag{2.2}$$
where the sector self-inductance is
$$L = \begin{bmatrix} L_{uu} & M_{vu} & M_{wu} \\ M_{uv} & L_{vv} & M_{wv} \\ M_{uw} & M_{vw} & L_{ww} \end{bmatrix} \tag{2.3}$$

and the sector mutual inductance is

$$M = \begin{bmatrix} -M_c & M_c & M_c \\ M_c & -M_c & -M_c \\ M_c & -M_c & -M_c \end{bmatrix} \tag{2.4}$$

The behaviour of the machine was studied by performing finite element simulations using the software FEMM (Finite Element Method Magnetics), which solves electromagnetic field problems by applying the finite element method to a two-dimensional (2D) or axisymmetric model of the machine under study. The idea of finite elements is to break the problem down into a large number of triangular-shaped regions, in which the solution is approximated by a linear interpolation of the values of potential at the three vertices of the triangle. If enough small regions are used, the approximate potential closely matches the exact solution. The advantage of breaking the domain down into a number of small elements is that the problem becomes transformed from a small but difficult-to-solve problem into a big but relatively easy-to-solve problem [17]. Material properties, such as relative permeability, conductivity or permanent-magnet magnetisation, are then assigned to each region of the mesh.

FEMM formulates Maxwell's equations in magnetostatic, electrostatic or time-harmonic form as a boundary-value problem. These equations are then converted into a system of algebraic equations by integrating them over each element using the chosen shape functions. Boundary conditions (Dirichlet, Neumann or mixed) are then applied to the edges of the computational domain to ensure the problem is well-posed. For example, this might involve forcing the magnetic potential to a fixed value or constraining the flux to flow tangentially.

Once assembled, the global system of equations is solved numerically for the unknown field quantities, which are typically the magnetic vector potential. From this solution, FEMM derives secondary quantities such as flux density, field lines, inductances, forces and torques. For example, the magnetic flux density B and the magnetic field intensity H can be obtained by differentiating the magnetic vector potential A, exploiting Maxwell's equations[17]. This approach enables FEMM to provide an accurate spatial distribution of electromagnetic fields based on the physics of the model and the local material characteristics.

A key assumption in this study was that the magnetic materials were linear, hence considering the B-H curve of the iron within its linear region. This simplification allowed neglecting magnetic saturation and, more importantly, applying the superposition principle. These assumptions were crucial for streamlining the analysis and reducing the computational complexity while still providing meaningful insights into the machine's performance. The machine model was created on FEMM according to the machine parameters from Table

1.1, and finally the materials were defined.

MATERIALS

Material	μ_x	μ_y	H_c [kA/m]	σ [S/m]
Copper	1	1	0	5.858×10^7
Air	1	1	0	0
IronLin	5000	5000	0	0
Iron M235-35A	0	0	0	0
Recoma 30HE	1.0636	1.0636	849.23	0
NeFeBo 38/23	1.03081	1.03081	958.08	0

Table 2.1: FEMM model materials

As visible from 2.1, the Iron $M235-35A$ was not defined in the same way as the other materials: its $B-H$ curve, shown in Figure 2.1, was imported as a vector instead.

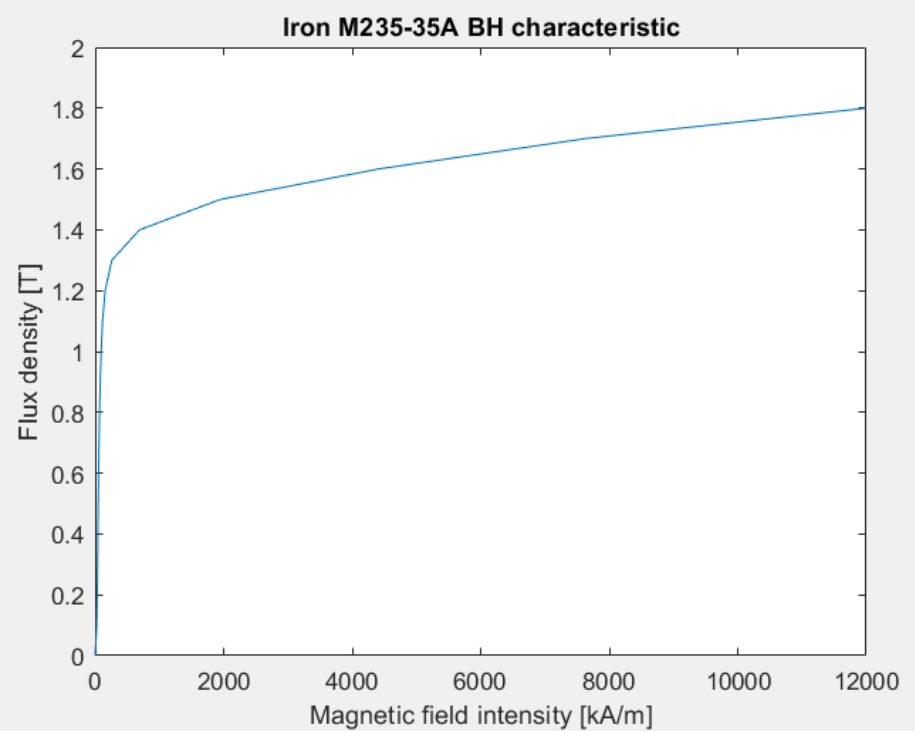

Figure 2.1: IronM235-35A BH curve.

The first version of the FEMM model is shown in Figure 2.2 in the software interface, from which is possible to observe the thickness of the mesh in correspondence of sharp edges and, most importantly, at the airgap: the model would feature 138k nodes.

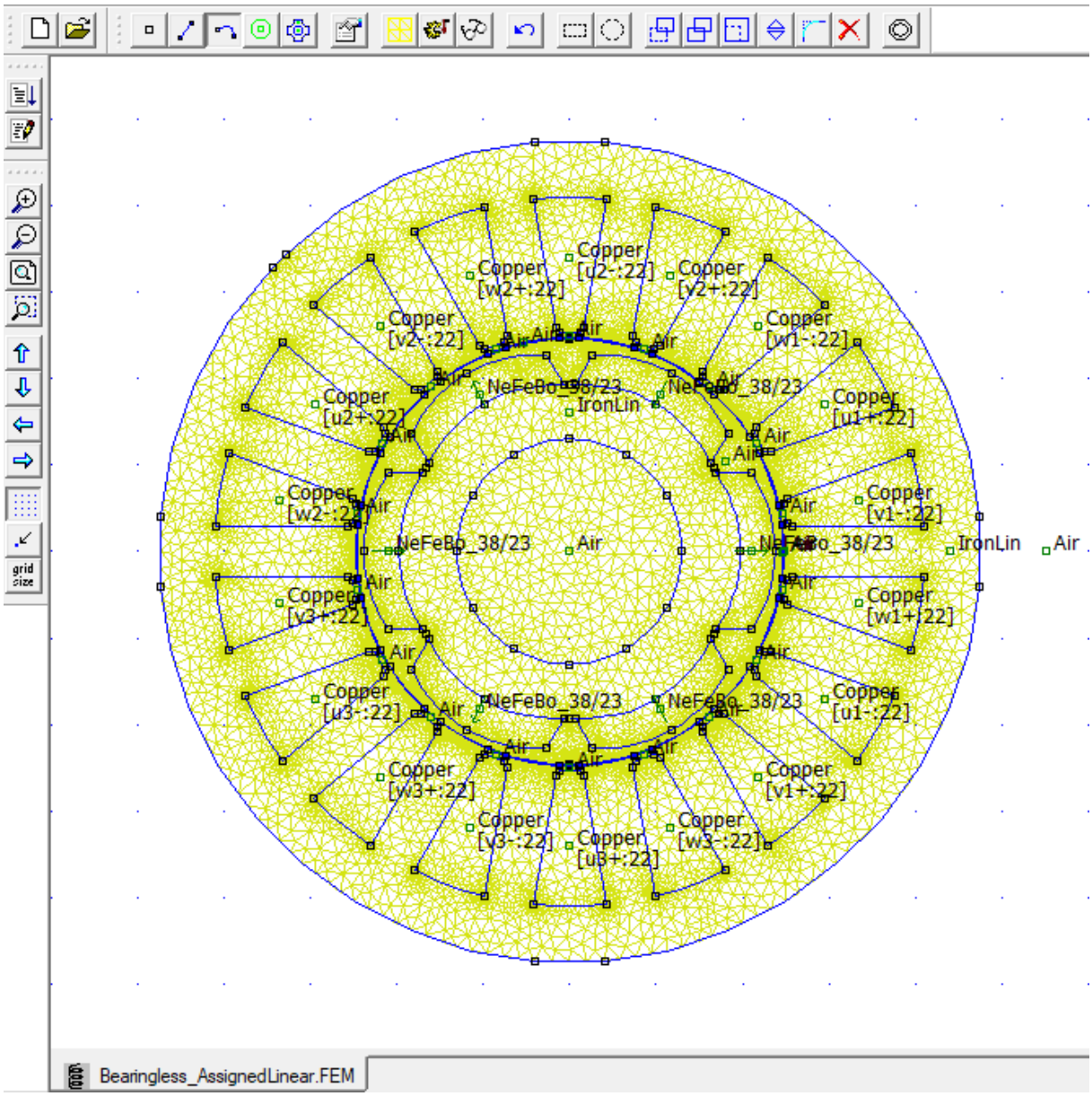

Figure 2.2: Mesh detail of FE model first version.

The magnetic vector potential method has been employed to compute the flux linkages: this method is computationally efficient and well-suited to implementation in finite element softwares, such as FEMM. The method is explained below using a machine with two slots per pole per phase as an example, where the coils are connected in series.
The linked flux for a given rotor position can be determined using the following integral formulation:

$$\varphi = -\frac{1}{2} N \int_{S_1} \int_{S_2} L_A A_z \, dS_1 dS_2 \tag{2.5}$$

Where:

- φ is the linked flux;
- S_1 and S_2 represent the surface of the corresponding slots' cross-section;

- N denotes the number of turns of the considered phase winding;
- l_z is the axial length of the machine;
- A_z is the magnetic vector potential;

For the machine under analysis, featuring one slot per pole per phase, instead, the linked fluxes were computed as follows: the FEMM instruction $mo\_blockintegral(2)$ performs the integration of the magnetic vector potential A_z according to the active length of the model l_z, and $mo\_blockintegral(5)$ computes the slots surfaces. Then, the flux is obtained as:

$$\varphi = N\frac{\psi_a - \psi_b}{\overline{S_{slot}}} \tag{2.6}$$

Where:

- ψ is the flux linkage of the phase slots (a and b)
- $\overline{S_{slot}}$ represent the average surface of the two slots' surface
- N is the number of winding turns

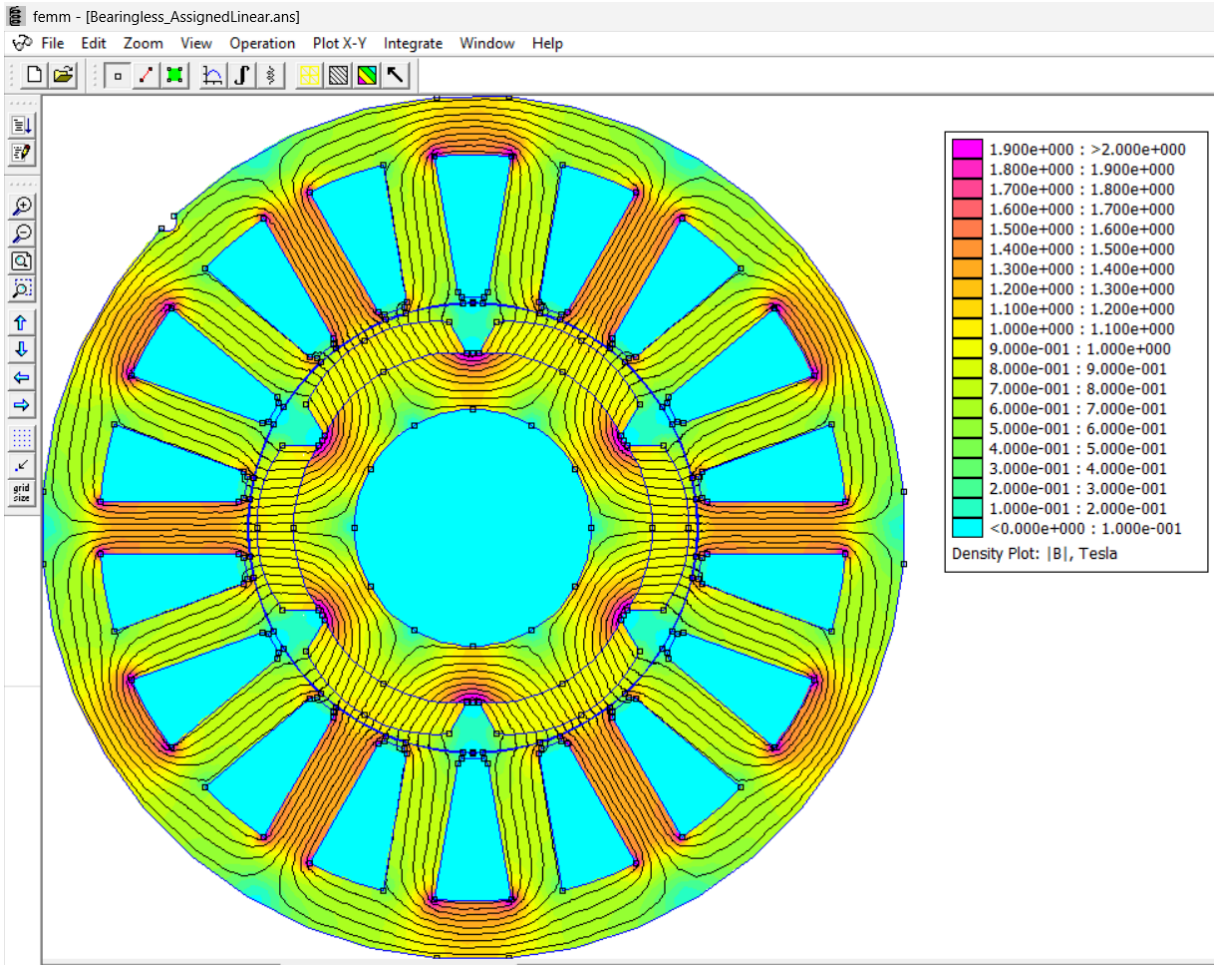

Figure 2.3: Flux density analysis of FE model first version.

The flux linkage ψ is the quantity returned by the FEMM command $mo\_blockintegral(2)$, corresponding to the magnetic field energy in the selected block. The physically rigorous and direct way to obtain the flux linkage of a conductor loop in FEMM is to compute the contour integral of the vector potential:

$$\lambda = \oint_{\partial S} \mathbf{A} \cdot d\ell,$$

so that the phase linkage is obtained as

$$\Lambda_{\text{phase}} = N\Big(\oint_{\Gamma_A} \mathbf{A} \cdot d\ell - \oint_{\Gamma_B} \mathbf{A} \cdot d\ell\Big)$$

where Γ_A and Γ_B represent the areas of the slots in which the phase windings are located in the motor. Since the magnetic flux density B, shown in Figure 2.3, can be expressed in terms of the magnetic vector potential A through the fundamental relation

$$\boldsymbol{B} = \nabla \times \boldsymbol{A},$$

on which the Stokes theorem can be applied:

$$\oint_{\partial S} \mathbf{A} \cdot d\ell = \int_S (\nabla \times \boldsymbol{A}) \cdot \boldsymbol{n} dS = \int_S \boldsymbol{B} \cdot \boldsymbol{n} dS = \varphi$$

to obtain the flux linkage on a single coil turn φ. This direct approach is recommended whenever accuracy and physical interpretability are required.

2.1.1 Maxwell Stress Tensor approach for radial forces computation

For what concerns the wrench vector, the Maxwell stress tensor (MST) method has been employed for its computation, as it allows for an efficient and straightforward evaluation using FEMM, since the software directly provides the force and torque calculation along a defined contour.

- $T = mo\_blockintegral(22)$
- $F_x = mo\_blockintegral(18)$
- $F_y = mo\_blockintegral(19)$

For the sake of completeness, a brief insight on the use of the MST to compute radial forces is provided [3].
Considering the motor as a cylinder, the Maxwell stress tensor σ can be depicted as shown in Figure 2.4:

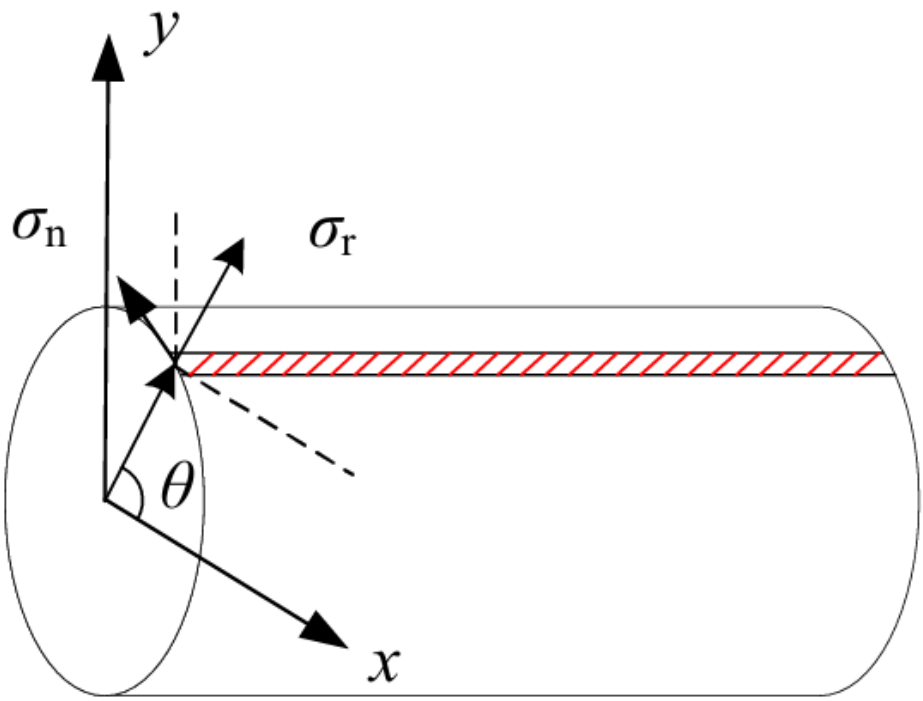

Figure 2.4: Maxwell stress tensor on the motor model [3].

$$\sigma = \sigma_r \boldsymbol{r} + \sigma_n \boldsymbol{n} = \frac{(B_r^2 - B_n^2)}{2\mu_0}\boldsymbol{r} + \frac{B_r B_n}{\mu_0}\boldsymbol{n} \tag{2.7}$$

Where $\boldsymbol{n}$ and $\boldsymbol{r}$ are the tangential and radial unit vectors, and B_n and B_r the related airgap flux density components, μ_0 is the vacuum permeability and θ is the rotor angular position relative to the x axis. Generally, it is possible to simplify (2.7) assuming that $B_r >> B_n$, as:

$$\sigma \approx \frac{(B_r^2)}{2\mu_0}\boldsymbol{r} + \frac{B_r B_n}{\mu_0}\boldsymbol{n} \tag{2.8}$$

Neglecting the saturation of the magnetic field and exploiting the superposition principle, the radial and tangential component of the magnetic flux density B can be rewritten, considering the contributions from permanent magnets and armature currents in the airgap, as:

$$B_r(t,\theta) = B_{r,PM}(t,\theta) + B_{r,w}(t,\theta) \tag{2.9}$$

$$B_n(t,\theta) = B_{n,PM}(t,\theta) + B_{n,w}(t,\theta) \tag{2.10}$$

From these considerations, since the solution of the suspension force using the Maxwell stress tensor method is related to the distribution of the air gap magnetic field, the derivation of the motor suspension force is based on a single sector suspension force. Subsequently, the motor's suspension force can be obtained by vector synthesis of the three sectors. By transforming (2.7) in a rectangular coordinate system, and setting the integral region as the air gap region related to sector 1 $[-\frac{\pi}{3}, \frac{\pi}{3}]$, the radial force resulting

from sector 1 can be obtained as shown in equations 2.11 and 2.12.

$$^1F_x = \int_{\frac{-\pi}{3}}^{\frac{\pi}{3}} dFx = \int_{\frac{-\pi}{3}}^{\frac{\pi}{3}} lr(\frac{B_r^2}{2\mu_0}cos\theta - \frac{B_rB_n}{\mu_0}sin\theta)d\theta \tag{2.11}$$

$$^1F_y = \int_{\frac{-\pi}{3}}^{\frac{\pi}{3}} dFy = \int_{\frac{-\pi}{3}}^{\frac{\pi}{3}} lr(\frac{B_r^2}{2\mu_0}sin\theta + \frac{B_rB_n}{\mu_0}cos\theta)d\theta \tag{2.12}$$

The exact same considerations apply for every sector of the machine, for which the superposition principle can be applied according to the initial assumptions: considering a generic sector s, the total forces and torque will be

$$\vec{F} = \sum_{s=1}^{n_s} {}^s\vec{F} \qquad T = \sum_{s=1}^{n_s} {}^sT \tag{2.13}$$

Where the force $\vec{F}$ is

$$\vec{F} = F_x\,\hat{x} + F_y\,\hat{y} = \left(\sum_{s=1}^{n_s} {}^sF_x\right)\hat{x} + \left(\sum_{s=1}^{n_s} {}^sF_y\right)\hat{y} \tag{2.14}$$

The x and y components of the force for the generic s sector in equation (2.14), as well as the generated torque, can be written in a unique vector ${}^s\overline{W}$, that represents the wrench vector written for the sector s:

$${}^s\overline{W} = \left[{}^sF_x, {}^sF_y, {}^sT\right]^T \tag{2.15}$$

2.2 Model variables

Considering the possibility of applying the superposition effect on the machine, the mapping was performed by supplying one phase at a time with direct current, while all the other currents were set to zero. This was made possible by the linear magnetic behaviour assumed for the machine, that allows to follow such procedure to finally apply the superposition effect to obtain the real-time behaviour of the motor, and by neglecting the magnetic coupling between the three sectors [7].
The principle of superposition states that, in a linear system, the response caused by multiple independent inputs can be determined by adding together the responses produced by each input acting alone when all the other inputs are set to zero. The problem in this case is well-posed for the application of this principle because, of the nine different cases considered, the phase currents were set to zero in all but one, which corresponded to the energized phase. This allows the contributions of each phase to be analyzed independently and then combined to determine the system's overall response. Leveraging this principle enables the model to maintain its validity and general applicability, facilitating a more systematic and structured analysis of the system's behaviour. The finite element mapping

of the bearingless machine was executed featuring five degrees of freedom, corresponding to five model variables:

1. **Number of mapped phases** n_{ph}, initially equal to 9;
2. **Rotor angular position** θ_m [°], covering the whole mechanical period (360°) through a number of steps $n\theta_m$;
3. **Phase current** γ_I, representing the instantaneous current flowing in the phase conductor.
4. **Eccentricity radius** r_ϵ, spanning from 0% to 15% of the nominal airgap $g_0 = 1$ mm, limited by the presence of the backup bearing discussed in Section 1.3.
5. **Eccentricity angle** θ_ϵ, to identify the possible rotor positions on the $x - y$ plane, through a number of steps $n\theta_\epsilon$.

The selection of the dimension of each variable would affect the resolution of the simulation with respect to the corresponding parameter: the higher the number of samples, the higher the accuracy of the model, yet the higher the computational time. The mapping procedure was performed through a chain of nested MATLAB functions, interacting with FEMM to perform the simulations and store the results in two MATLAB structures, one for the fluxes and one for the wrench vector, and finally compute the inductance matrix and wrench. The final steps consisted of performing an interpolation on r_ϵ to extend the results over the available airgap with higher resolution. For a correct execution of this final step, the angular domain defined for the variable θ_m does not include the value of 360°, since the first value is always 0° and the presence of a duplicated sample corresponding to the same physical rotor position might lead to inconsistencies in the interpolation process, potentially compromising the smoothness of the reconstructed waveforms. The workflow can be summarized through the following MATLAB scripts/functions sequence:

1. *MainScript.m*: script acting as user interface to adapt the settings for the simulation, through the four variables discussed above.
2. *OutputsCalculation.m*: a function that sets the FE model characteristics according to the variables setting. It interfaces with FEMM to perform rotor rotation and radial displacement and set phase currents for each combination of [θ_m,γ_I,r_ϵ,θ_ϵ], for each phase. Then, the function performs meshing and, finally, solves the electromagnetic problem. The function is composed of nested *for* loops, to simulate for each combinations of the variables enumerated above.
3. *PostProcessing*: function computing linked flux and wrench through FEMM instructions called by the MATLAB code, finally saving the results into two structures called *Phi.mat* and *WrenchStruct.mat*.

4. *InterpolationScript.m*: function performing spline-based interpolation on the available samples, over the eccentricity radius interval $r_\epsilon = [0 - 15]$ % with 1% resolution, to obtain a refined dataset, with improved granularity and a smooth variation of the interpolated values across the entire span.

As a result, for each considered system output, a 12-dimensional matrix containing the wrench and inductance coefficients was obtained.

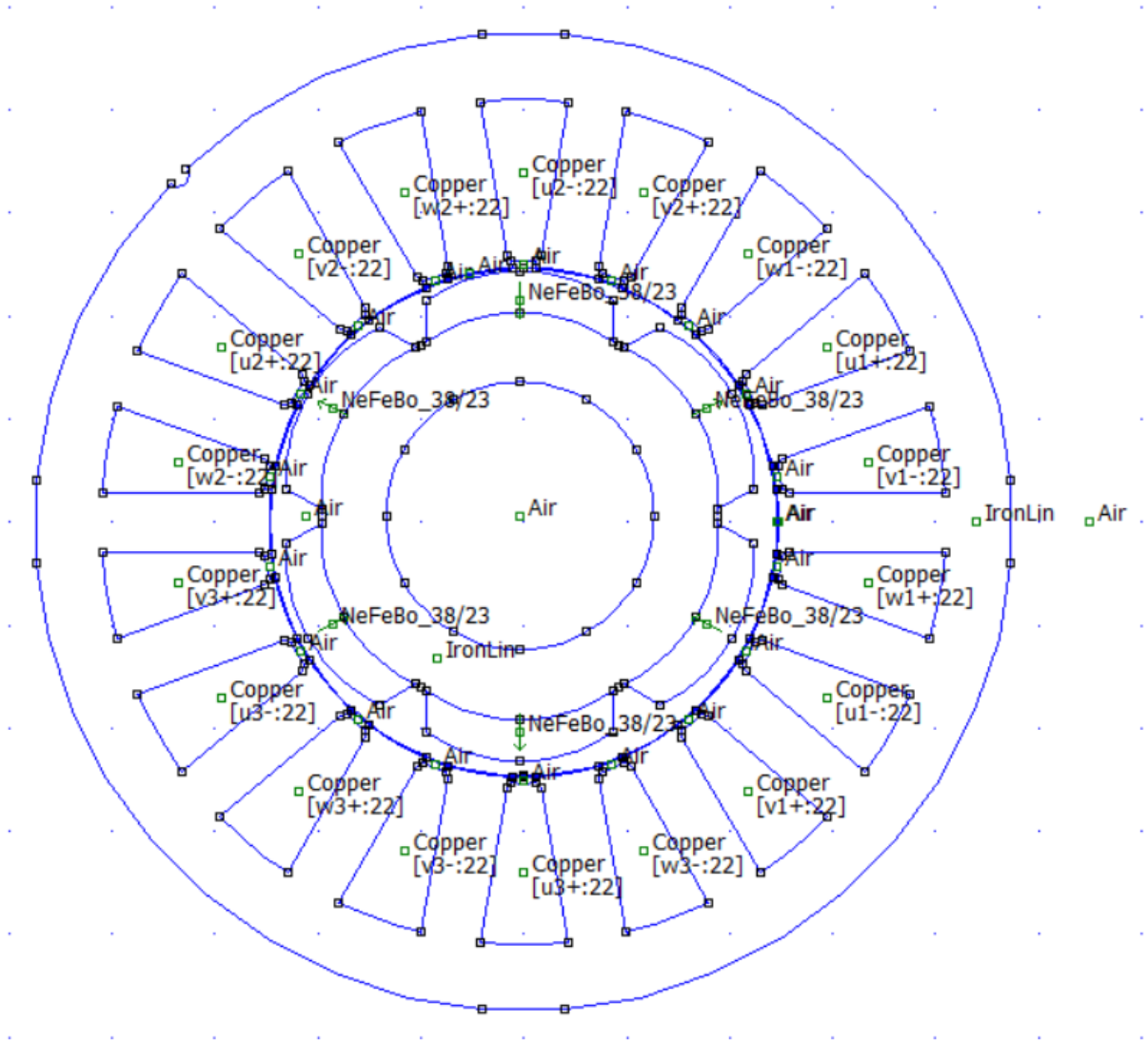

Figure 2.5: Rotor eccentricity in FEMM model (r_ϵ : 90%,θ_ϵ : 90°).

Thanks to the linear relationship between current and generated electromagnetic quantities within the operating region of interest, this normalization is advantageous, as the same coefficient set can be used to simulate any current level. This enables efficient exploration of a wider range of operating scenarios with a single, compact representation. For the wrench, the first dimension represents the rotor position θ_m, the following nine dimensions correspond to the currents of the nine machine phases $[I_1, I_2, \ldots, I_9]$, while the remaining two represent the eccentricity radius r_ϵ, and its direction θ_ϵ. For the inductance,

instead, the first two dimensions correspond to the number of phases (9x9), the following nine represent the phase currents, and the final two dimensions represent the eccentricity radius r_ϵ, and its direction θ_ϵ. This step was fundamental for the development of the machines' numerical models. For what concerns the fluxes, the superposition principle was applied as:

$$\varphi_i(I_1, I_2, \ldots, I_8, I_9, \vartheta_m, r_\epsilon, \vartheta_\epsilon) = \varphi_{i0}(\vartheta_m, r_\epsilon, \vartheta_\epsilon) + \sum_{x=1}^{9} [\varphi_{ix}(I_x, \vartheta_m, r_\epsilon, \vartheta_\epsilon) - \varphi_{i0}(\vartheta_m, r_\epsilon, \vartheta_\epsilon)] \tag{2.16}$$

Where:

- φ represents the linked fluxes to a generic stator phase;
- I_j with $j = 1, 2, ..9$ is the current along the j phase;
- ϑ_m is the rotor position;
- $r_\epsilon, \vartheta_\epsilon$ are the radius and angle of the eccentricity;
- φ_{ix} is the linked flux to a generic stator phase i while feeding only the x phase;
- φ_{i0} is the no-load linked flux to a generic stator phase i

And from fluxes, the generic element of the inductance matrix L_{ij} was computed as:

$$L_{ij} = \frac{\partial \lambda_{ij}}{\partial I_j} = \frac{\phi_{ij}(I_j = I_{nom}) - \phi_{ij}(I_j = 0)}{I_j} \tag{2.17}$$

Regarding the wrench instead, the equations make use of the coefficients obtained during the mapping, exploiting again the linearity assumption to consider phase current values different from the simulated ones (0 and ± 20 A). The wrench coefficients are obtained by normalizing the corresponding wrench element with respect to the machine's rated current (kF_x,kF_y,kT in equations 2.18,2.19,2.20). These allow to apply the superposition effect by considering the contribution of each phase current I_j in terms of radial force on x and y direction, and torque:

$$F_x(I_1, I_2, I_3, I_4, I_5, I_6, I_7, I_8, I_9, \vartheta_m, r_\epsilon, \vartheta_\epsilon) = \sum_{j=1}^{9} kF_{x,j}(\vartheta_m, r_\epsilon, \vartheta_\epsilon) \cdot I_j \tag{2.18}$$

$$F_y(I_1, I_2, I_3, I_4, I_5, I_6, I_7, I_8, I_9, \vartheta_m, r_\epsilon, \vartheta_\epsilon) = \sum_{j=1}^{9} kF_{y,j}(\vartheta_m, r_\epsilon, \vartheta_\epsilon) \cdot I_j \tag{2.19}$$

$$T(I_1, I_2, I_3, I_4, I_5, I_6, I_7, I_8, I_9, \vartheta_m, r_\epsilon, \vartheta_\epsilon) = \sum_{j=1}^{9} kT_j(\vartheta_m, r_\epsilon, \vartheta_\epsilon) \cdot I_j \tag{2.20}$$

The control algorithms implementing the lookup table obtained through this approach in Simulink would use it for the application of the superposition principle, exactly as shown

in equations (2.18), (2.19), (2.20), to obtain the real behaviour of the machine.
The original simulation data set for the mapping procedure would feature:

- $n\theta_m = 36$ rotor angular positions, corresponding to a step $\Delta\theta_m = 10°$, hence mapping $\theta_m = [0°,...,350°]$;
- 3 current values, considering no-load condition (0 A) and nominal current flowing in both directions (± 20 A), to compute no-load flux and reluctance wrench as well as their rated-current equivalents.
- $nr_\epsilon = 3$ eccentricity radius values: $r_\epsilon = [0, 10, 50]$ % with respect to nominal airgap $g_0 = 1$ mm;
- $n\theta_\epsilon = 6$ eccentricity angles: $\theta_\epsilon = [0, \frac{\pi}{6}, \frac{\pi}{3}, \pi, \frac{2\pi}{3}, \frac{5\pi}{6}]$;

The computation of the number of performed simulations (1 for each combination of $[\theta_m,\gamma_I,r_\epsilon,\theta_\epsilon]$ per phase) is quite straightforward:

$$N_{sim} = n\theta_m \cdot n\gamma_I \cdot nr_\epsilon \cdot n\theta_\epsilon \cdot n_{ph} = 36 \cdot 3 \cdot 3 \cdot 6 \cdot 9 = 17496 \tag{2.21}$$

For such a thick-meshed model as the original one, for which FEMM would take about 35 seconds to solve the magnetic circuit, the whole mapping operation would require 7 days to map the whole machine, assuming that the simulation time would coincide with the FEA execution time, with no further delay.

$$T_{sim} = \frac{\frac{35 \cdot 17496}{3600}}{24} = 7.0875 \tag{2.22}$$

The thesis work, through the strategies analyzed in Chapter 3, focused on reducing both the computational effort and the elapsed time for the mapping procedure while maintaining high accuracy with respect to the original results.
The proposed mapping procedure has not been validated against new experimental measurements, since equivalent modeling approaches have already been extensively presented in the scientific literature, often supported by experimental results or as a support itself for the analytical model [12], [5], [8], [15], [16], [9], [6], [18]. Therefore, the validity of the adopted model is supported by the consistent and consolidated use of similar formulations in previous peer-reviewed works.

2.3 Mapping results

As an example, some plots are illustrated in the final part of this chapter to provide some insights and comments on the machine behaviour, as a completion of the descriptions

previously provided.

The interpolation function allowed for obtaining a wider set of eccentricity radii r_ϵ. Indeed, from the interpolation results, the available radii are $r_\epsilon = [0, 10, \ldots, 70, 80]\%$ of the nominal airgap ($g_0 = 1$ mm): even though most of these values exceed the physically feasible eccentricity, that is limited by the backup bearing, it is interesting to delve into the simulations to understand the principles of development of radial forces and torque in the motor.

After the interpolation step, some plots were generated with a MATLAB script: each plot, as titles and legends will clarify, depicts the radial forces generated by feeding a single phase with the machine nominal current of 20 A, for a given eccentricity radius r_ϵ, varying the eccentricity angle θ_ϵ, as if the rotor was following a step-wise circular trajectory around the stator axis. For the sake of clarity, only a few points were simulated to obtain the most intuitive yet readable results possible.

As a first step, the eccentricity radius was fixed at $r_\epsilon = 60\%$, and the rotor was moved towards different directions: figures 2.6 - 2.13 depict this analysis, to investigate the impact of the rotor position relative to the fed phase magnetic axis.

The plots shown in this section, and generally most of the ones included in this work, show the machine main quantities while varying the rotor angular position θ_m, hence while the rotor structure performs a mechanical revolution.

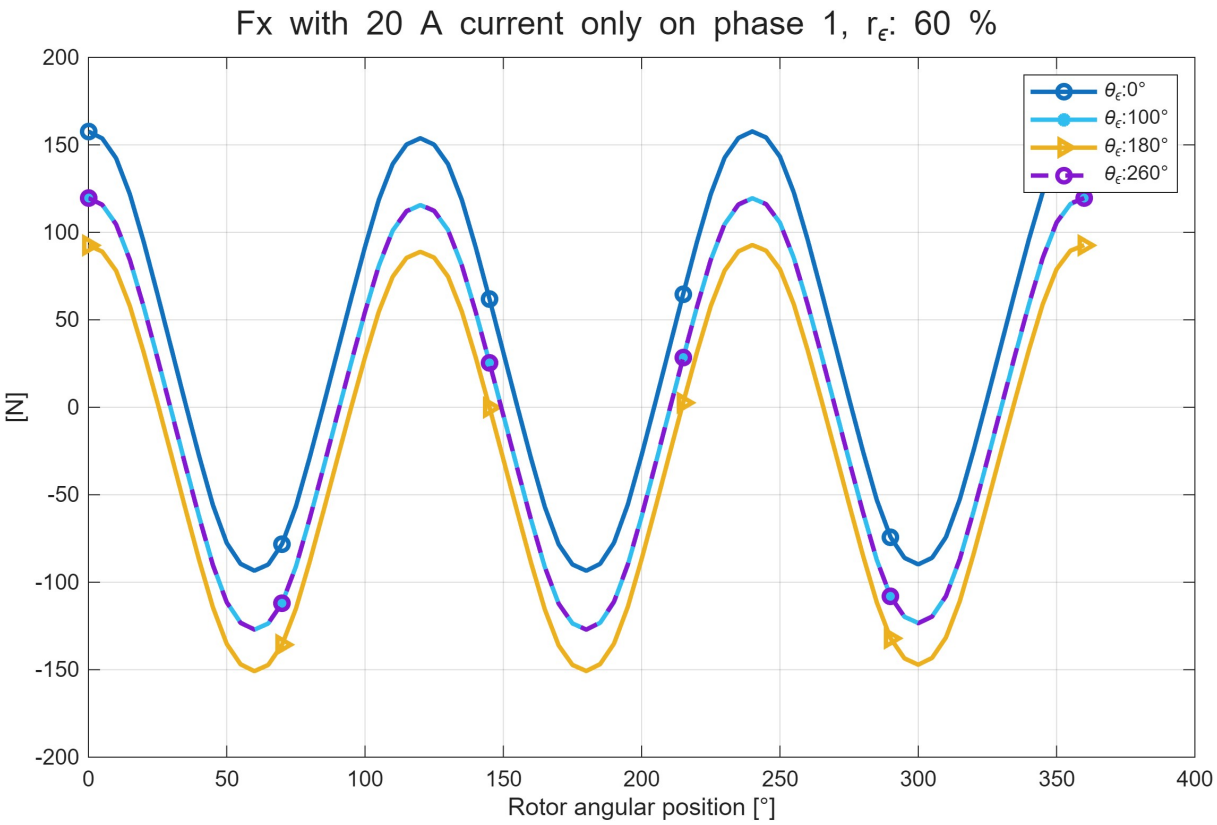

Figure 2.6: Force component on x axis for $r_\epsilon = 60\%$ when feeding phase 1.

Figure 2.6 shows the radial force acting on the x axis for a rotor revolution: the periodicity of the waveform suggests again that a mechanical period is being shown, with three electrical periods within it; a high eccentricity (60%) is simulated while feeding phase 1, having magnetic axis aligned with the x axis, as visible from the motor section depicted in Figure 1.6. This situation causes an interaction between the permanent magnets and the armature currents' flux densities that eventually results in an important unbalance in the flux density at the airgap: the most trivial cases are the ones in which $\theta_\epsilon = 0°$ and $\theta_\epsilon = 180°$, in which the rotor is moved towards and away from phase 1, respectively. It is possible to notice that, besides the oscillating contribution due to the permanent magnets' action, the blue and yellow waveforms present a positive and a negative offset, proving what has been discussed regarding UMP: when the rotor is moved towards the stator in a given direction, the mismatch of the flux densities causes the development of a radial force enhancing the rotor eccentricity even more. For this reason, when the rotor is shifted towards $\theta_\epsilon = 0°$, the average F_x (neglecting the effects of PM) is positive, while when the rotor is moved towards the opposite direction $\theta_\epsilon = 180°$, F_x is negative. The other two represented cases consider two eccentricity angles with the same horizontal component: $\theta_\epsilon = 100°$ and $\theta_\epsilon = 260°$ are symmetrical with respect to the x-axis and then cause the exact same F_x. Another important take away of this section is the conclusion that feeding a given phase with the nominal 20 A current causes attraction force with north-pole magnets, with magnetization direction towards the airgap, and repulsion for south-pole magnets.

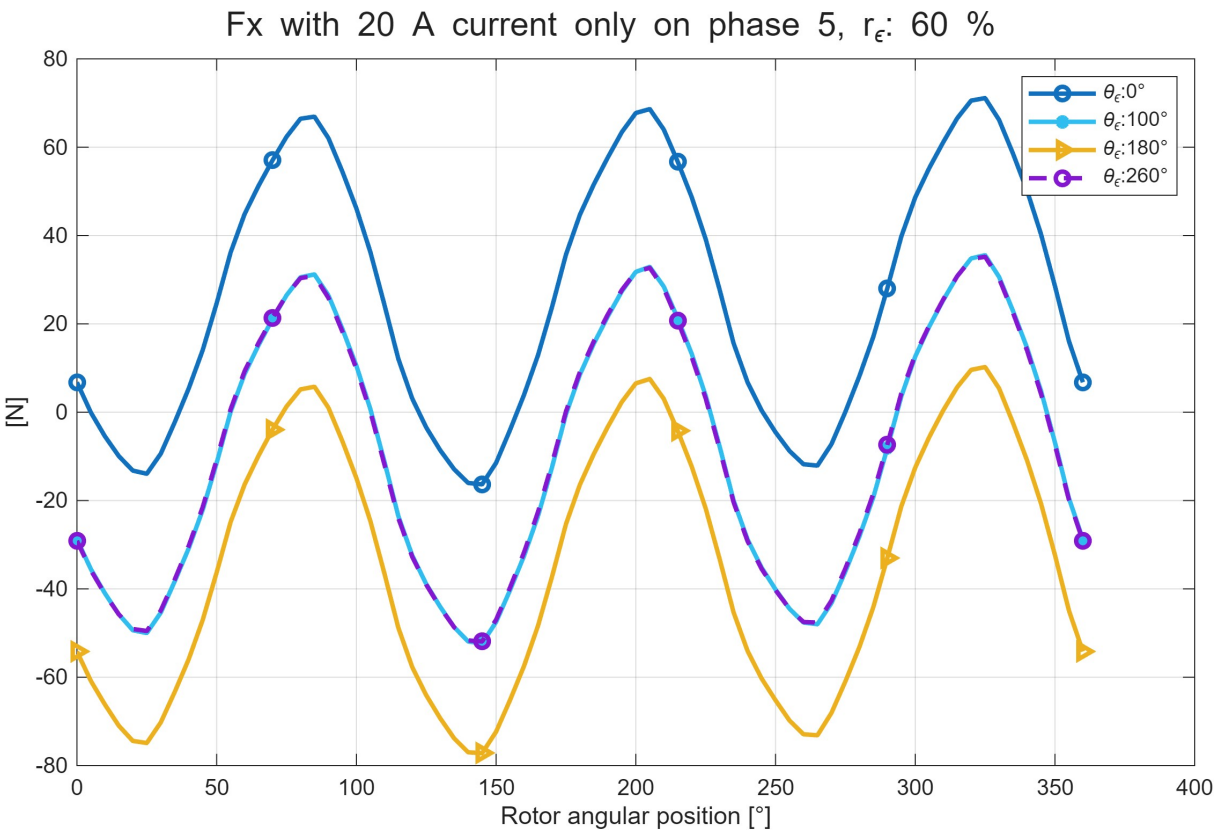

Figure 2.7: Force component on x axis for $r_\epsilon = 60\%$ when feeding phase 5.

When the phase axis is not aligned with one of the axes of the $x - y$ reference frame, the resulting radial forces are no longer sinusoidal, but show the same behaviour with respect to eccentricity as explained for the previous picture. Again, $\theta_\epsilon = 100°$ and $\theta_\epsilon = 260°$ cause the exact same F_x (Figure 2.7).

Analogies can be found when investigating on F_y development, also on the role of the relative position of permanent magnets with respect to the phase axis: as shown in Figure 2.8, when the rotor is displaced towards x axis only, the average F_y is null, yet as soon as the rotor spins and the magnet is not any more aligned to the phase axis, the resultant force contains a y component as well, that becomes null again when the adjacent magnet aligns with phase axis, hence with a 60° period. When the displacement differs from the phase axis, instead, an important offset shows up in F_y as well ($\theta_\epsilon = 260°$).

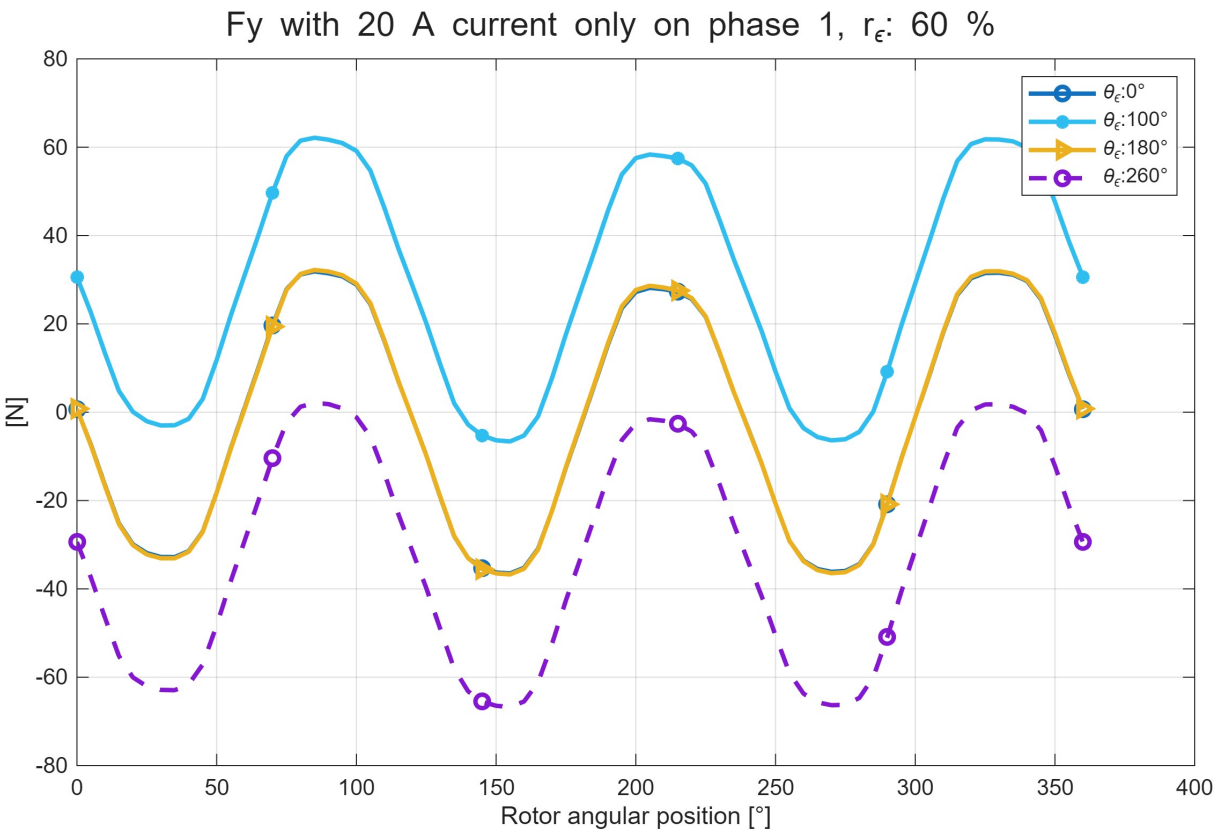

Figure 2.8: Force component on y axis for $r_\epsilon = 60\%$ when feeding phase 1.

Due to the motor structure, there is no phase aligned with y axis, but the one with the most vertical axis is phase 9: Figure 2.9 shows similar behaviour of F_y with the waveform of F_x for phase 1 (Figure 2.6). Opposite vertical eccentricity angles $\theta_\epsilon = 100°$ and $\theta_\epsilon = 260°$ cause opposite force offsets in the exact same way.

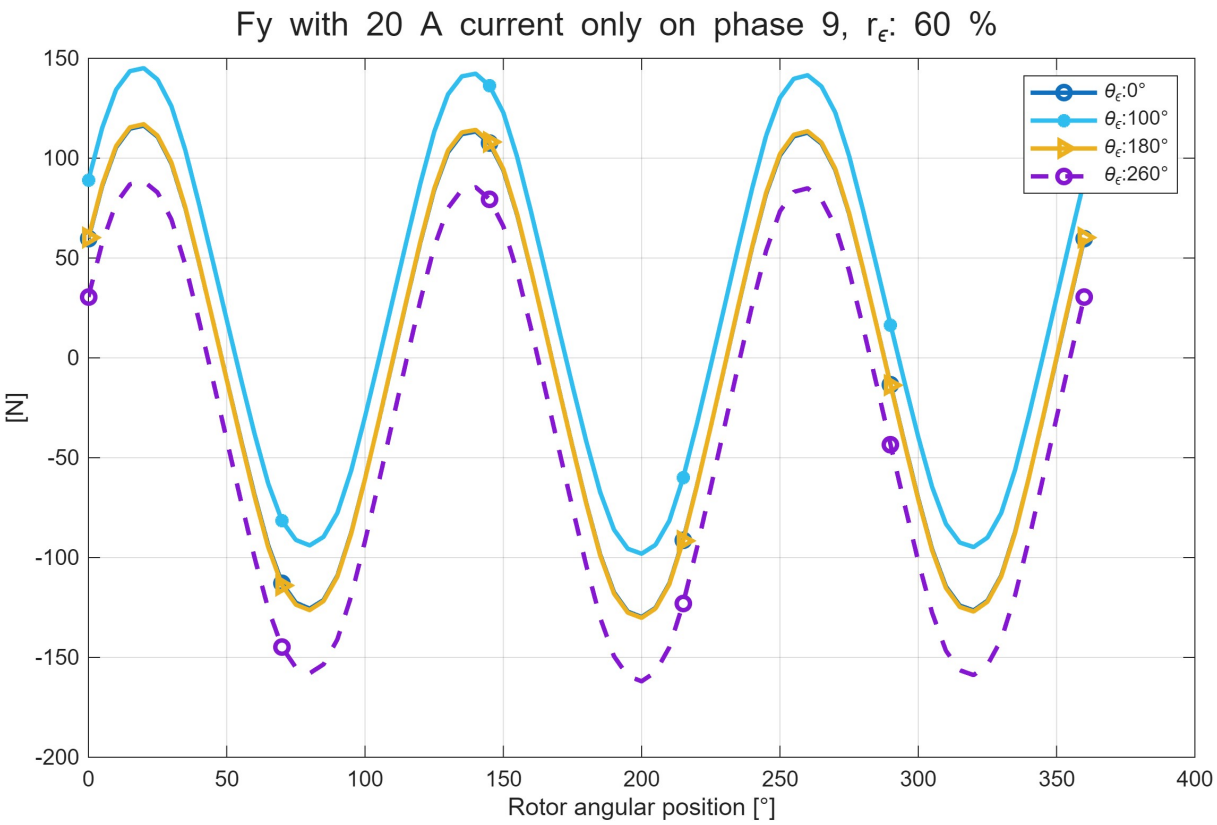

Figure 2.9: Force component on y axis for $r_\epsilon = 60\%$ when feeding phase 9.

As a second step, the opposite procedure was followed: figures 2.10 - 2.12 depict some of the wrench elements for different eccentricity radii, towards a fixed direction, to provide the reader with an insight into the influence of the airgap flux density unbalance of the wrench generated by the machine.

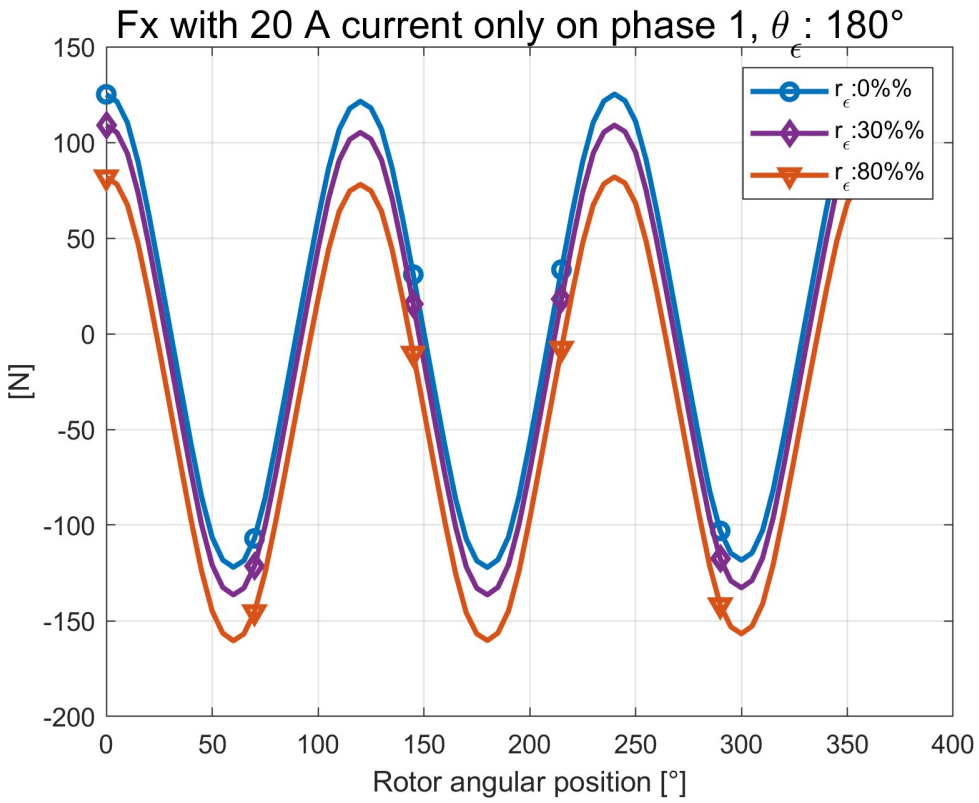

Figure 2.10: Force component on x axis for $\theta_\epsilon = 180°$ when feeding phase 1.

In Figures 2.10 and 2.11, the more the rotor moves towards the negative x direction (higher r_ϵ, $\theta_\epsilon = 180°$), the more intense becomes the force generated by the unbalanced magnetic pull. This is trivially more impactful for the case in which phase 1 is fed, due to the physical disposition of the phase magnetic axis.

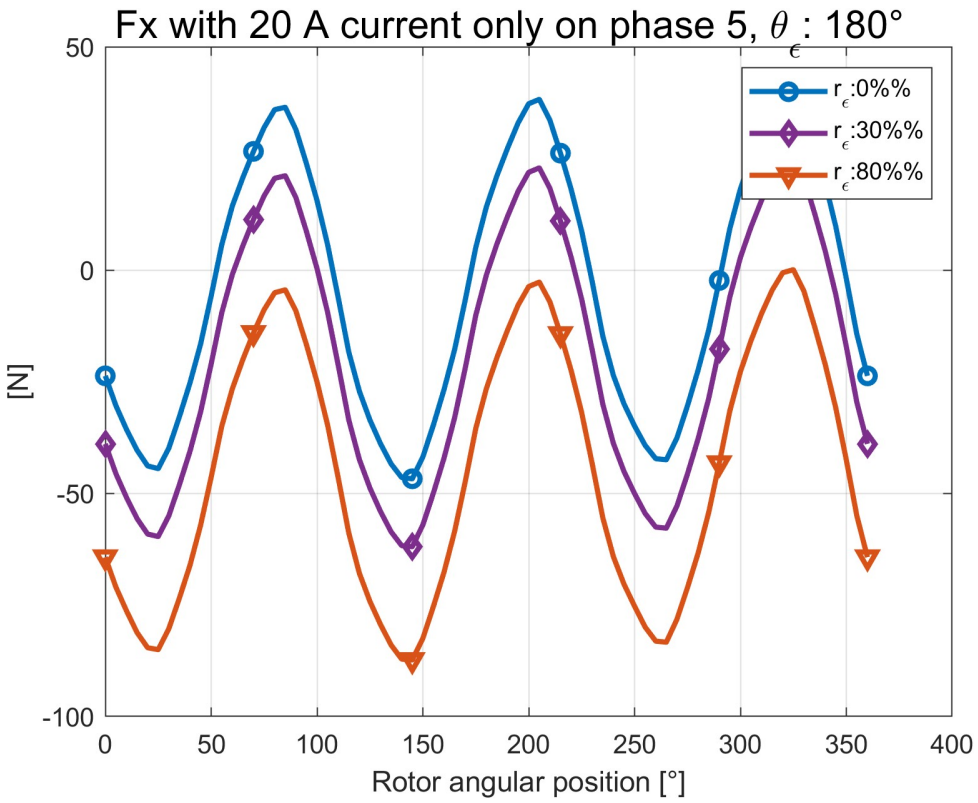

Figure 2.11: Force component on x axis for $\theta_\epsilon = 180°$ when feeding phase 5.

Regarding torque, it is clear from Figures 2.12 and 2.13 that it is not influenced by eccentricity, either radius or angle, besides slight peak variations, but maintains a null average value. The torque peaks appear when the phase axis the interface between two consecutive magnets, where the stator MMF can act the most effectively on the rotor iron core. For phase 9, with axis at 260° and the closest magnet axis at 270°, it verifies after the rotor spins by 50° and faces the next magnet.

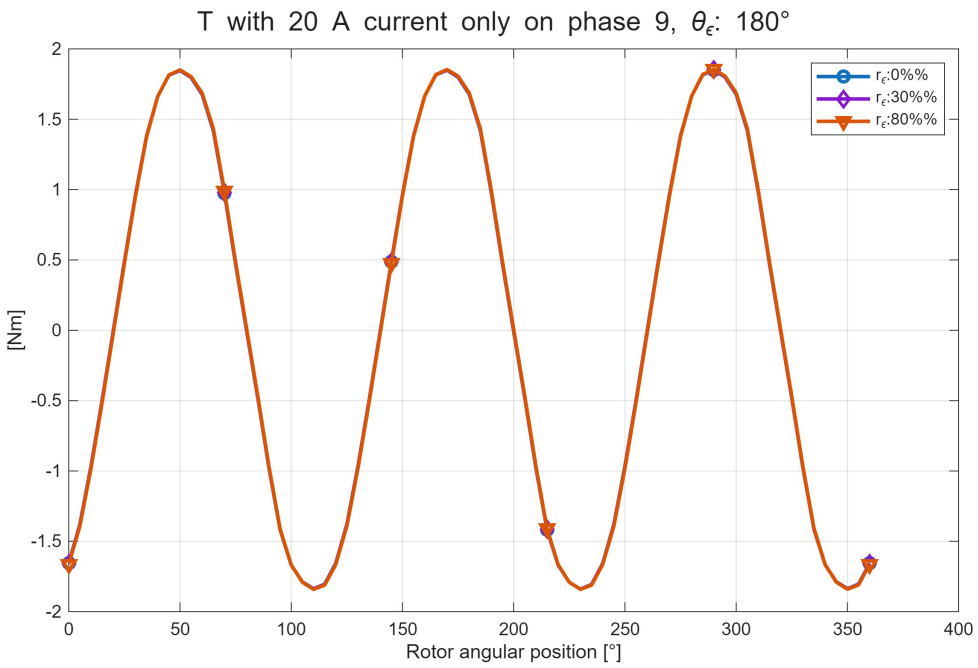

Figure 2.12: Torque for θ_ϵ =180° when feeding phase 9.

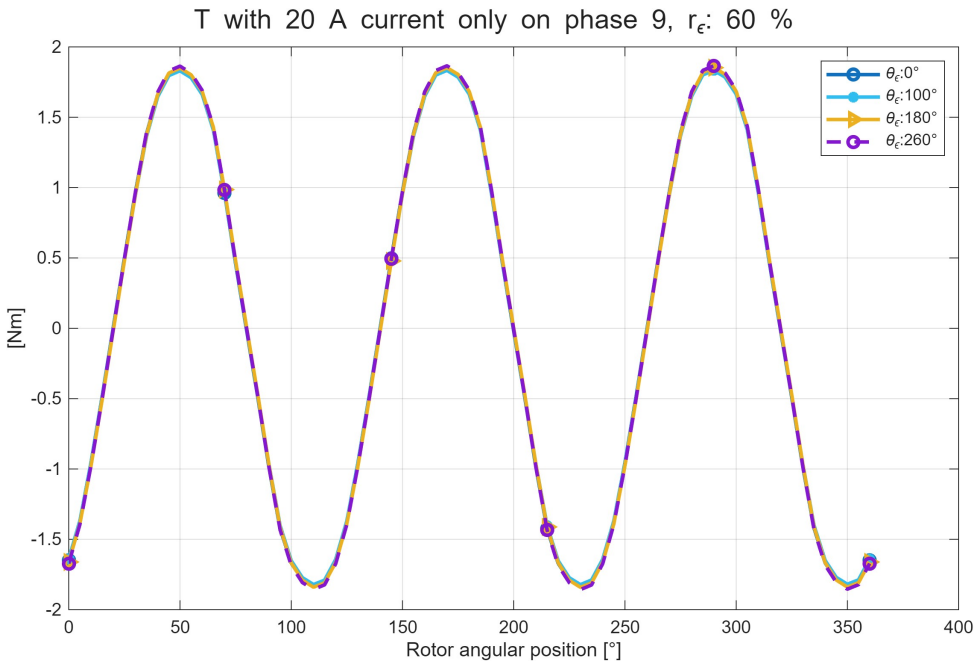

Figure 2.13: Torque for $r_\epsilon = 60\%$ when feeding phase 9.

Regarding flux linkages, the effect of eccentricity consists of an amplification or reduction of the permanent magnets' linked flux on the winding. As an example, the analysis of φ_{11} for different rotor eccentricities is displayed in Figure 2.14, in which the centered case (green plot) is compared with the amplified results in case the rotor is displaced towards the winding's magnetic axis (red plot) and the opposite case, with further rotor, which results in a lower flux linkage intensity (blue plot), as noticeable in correspondence of the waveforms peaks.

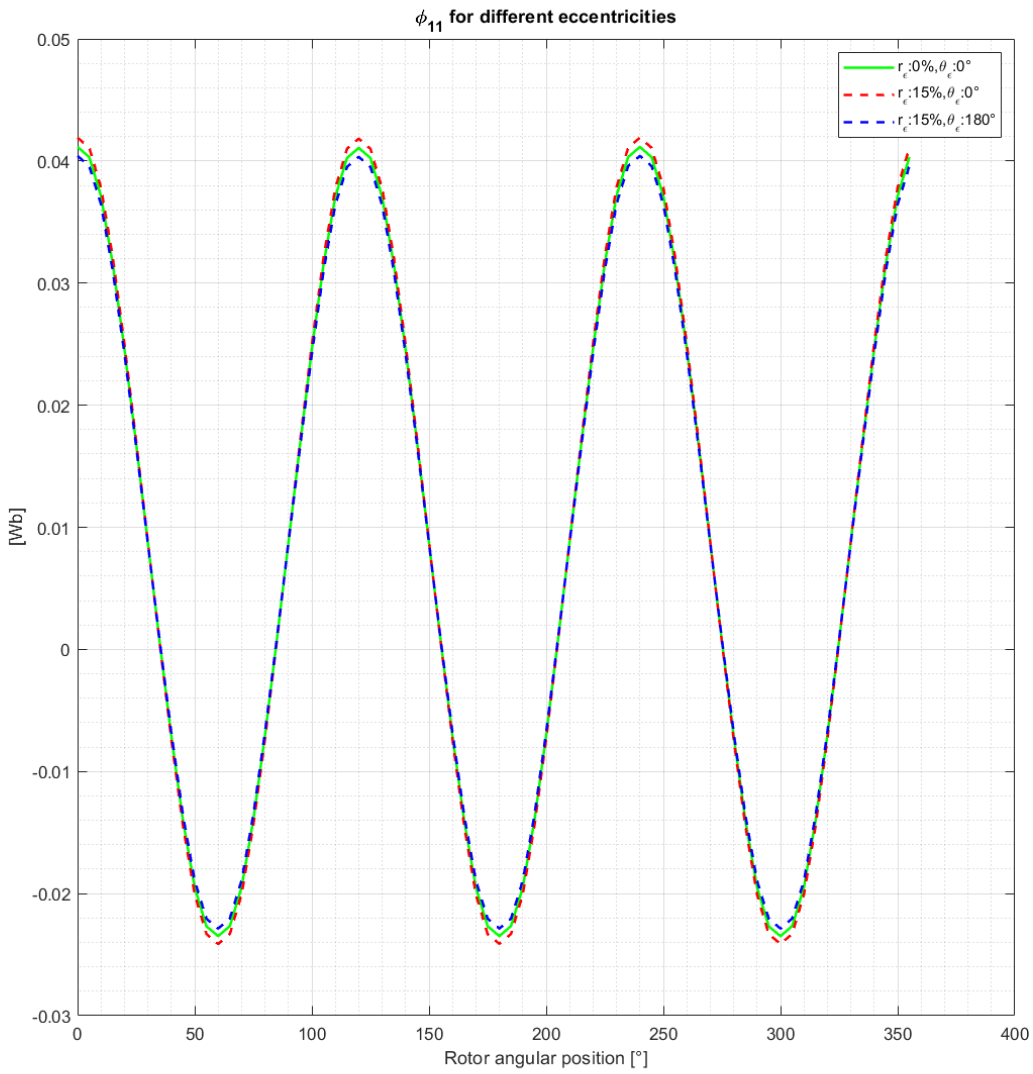

Figure 2.14: φ_{11} vs eccentricity.

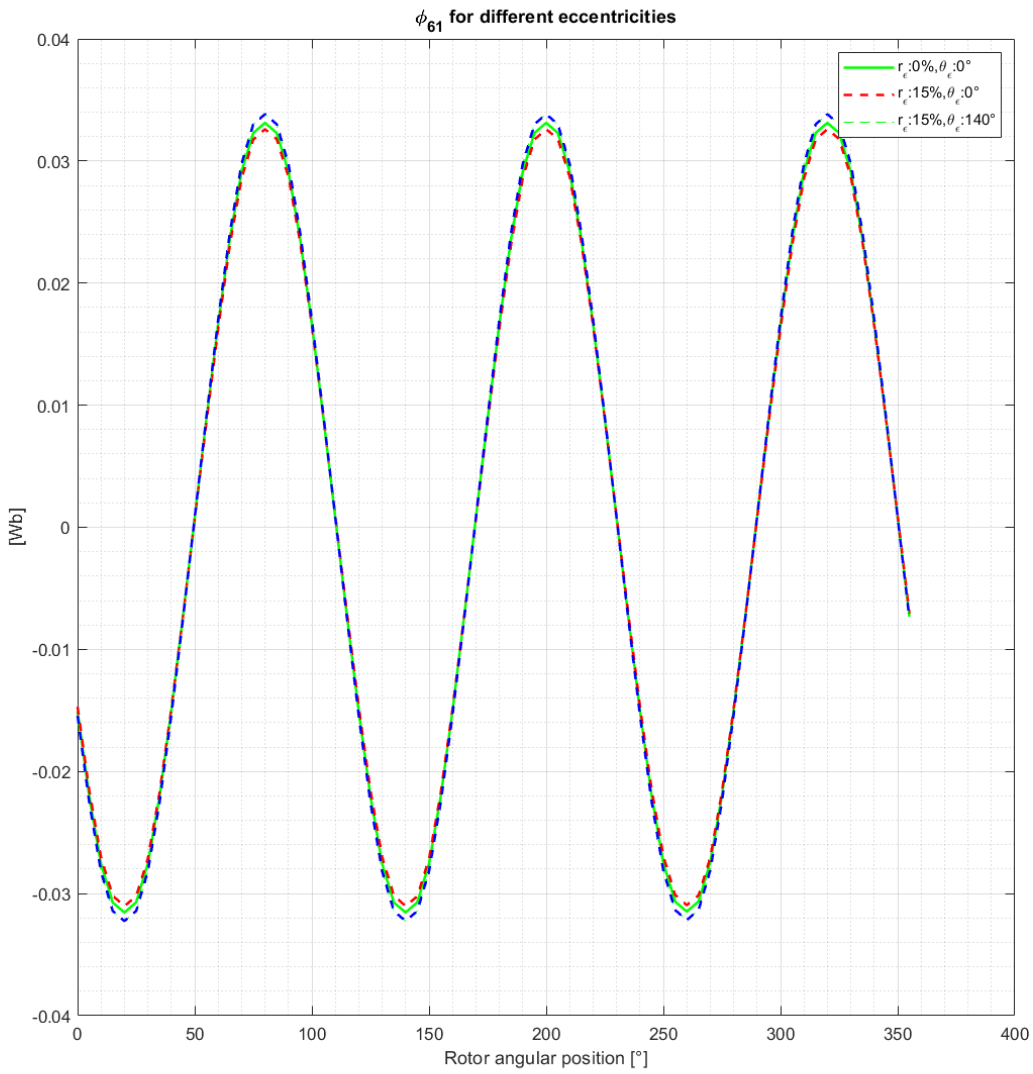

Figure 2.15: φ_{61} vs eccentricity

Again, the analysis of φ_{61} for different rotor eccentricities is displayed in Figure 2.15, comparing the centered case with different rotor displacements with the same criteria of the previous figure, adapting the eccentricity direction to the magnetic axis of phase 6.

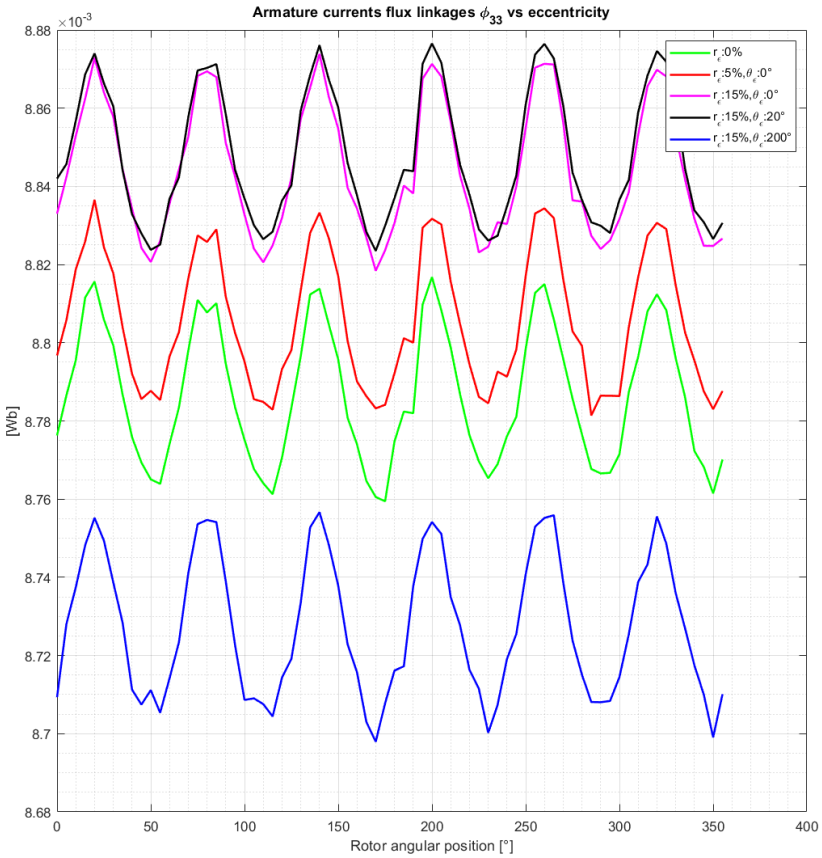

Figure 2.16: Armature flux linkage φ_{33} for different eccentricities.

An analysis of the effects of eccentricity to the flux linkage caused by the armature currents can be performed thanks to the assumption of linear behaviour of the machine, which allows plotting such flux linkages as the difference of on-load and no-load flux linkages. It is possible to notice in Figure 2.16 that when the proximity of the rotor to the winding of phase 3, with a magnetic axis at 20 mechanical degrees, is maximum ($\theta_\epsilon = 20°$, black line), it provides a lower reluctance path for flux lines, causing higher flux linkage for phase 3 φ_{33}. Even though the PM flux contribution was removed, a periodicity due to the magnets is still identifiable in the flux linkage plots due to the reluctance variation that the rotor rotation causes, alternating air gaps and magnets with inherently different magnetic permeability.

Chapter 3

Fast mapping strategies

This chapter deals in detail with all the strategies that were implemented to reduce the computational duty of the mapping procedure and, as a consequence, the simulation time. The modifications included geometrical transformations, model adaptation, mathematical elaborations, and finally the implementation of two different mapping processes for the inductance matrix and wrench vector. During the introduction of each of the adopted strategies, frequent comparisons with previous versions are provided in order to confirm the accuracy of the newly introduced model versions.

3.1 Early optimization strategies

As described in Chapter 2, the original FEMM model had a very thick mesh, featuring approximately 140k nodes, leading to a very computationally heavy simulation. To mitigate this, the original model $Bearingless\_AssignedLinear.FEM$ was modified into $Bearingless\_AssignedLinear\_LowMesh.FEM$, an identical model but with a looser mesh: a strong reduction —by approximately 80% - was applied to the model mesh, resulting in a 33k nodes final model. This modification allowed for a faster magnetic circuit resolution by FEMM, drastically reducing the simulation time by itself. The adoption of the new loose-meshed $.FEM$ model would ensures a reduction in the number of mesh nodes of:

$$100 \cdot (1 - \frac{n_{loose}}{n_{thick}}) = 100 \cdot (1 - \frac{33000}{140000}) \approx 76.4\% \tag{3.1}$$

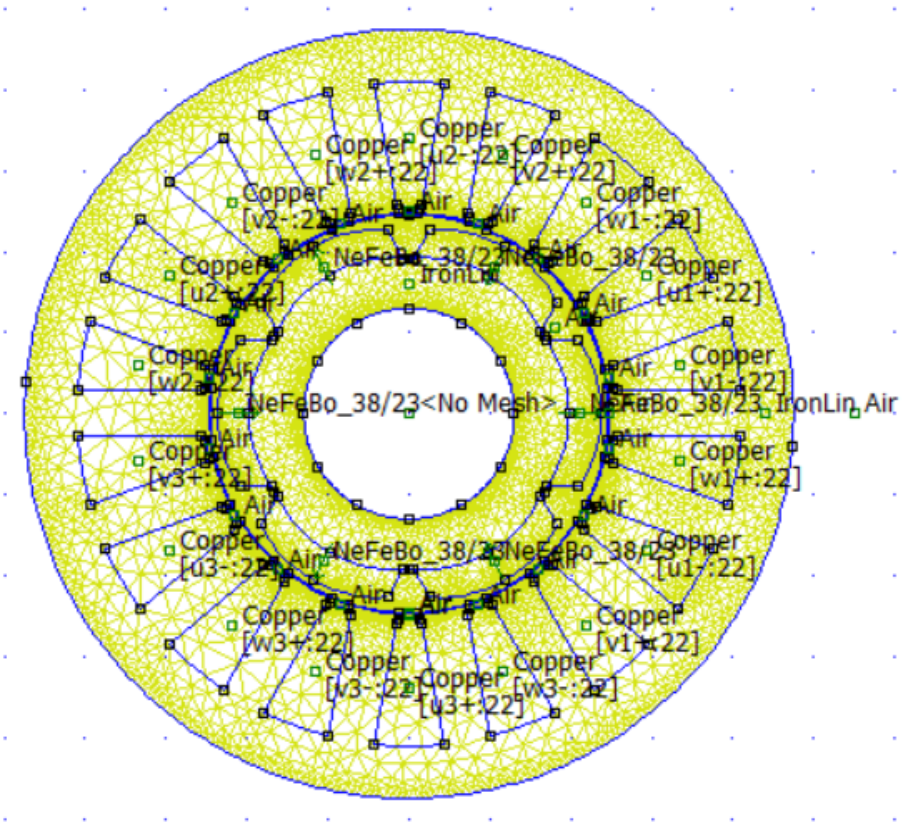

Figure 3.1: Loose-mesh model.

From Figure 3.1, even though the lower mesh thickness is not easily distinguishable with respect to Figure 2.2, it is possible to notice that the mesh was not applied in the rotor shaft, since it would have had no effects besides slowing down the simulation. As will be explained in Chapter 4, these actions did not affect the model accuracy; the resulting wrench and inductance matrix LUTs were compared with the ones obtained from the original $.FEM$ model.

In Chapter 2, the model variables θ_m, γ_I, r_ϵ and θ_ϵ were introduced. While the reduction of the θ_m sample size will be addressed in Section 3.2.3, the assumption of linearity of the machine allows to reduce the size of the currents set γ_I: indeed, for negative current values, the effects obtained from the positive current results can be used with an opposite sign. Under this hypothesis, the currents set can be reduced to $\gamma_I = [0, +20]$ A.

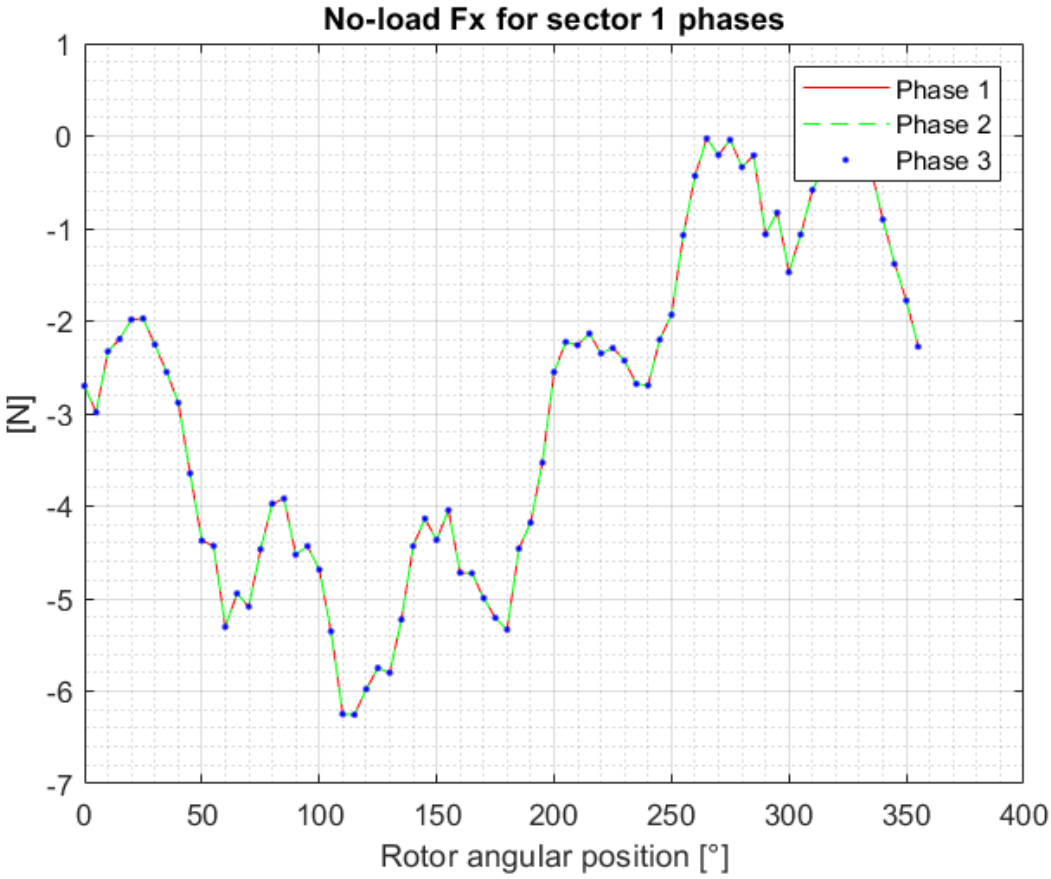

Figure 3.2: No-load F_x for sector 1 phases.

Moreover, as confirmed by analyzing the original mapping results, it was found that the no-load results are the same for every "fed" phase, as the magnetic circuit to be simulated is literally the same for the same eccentricity configuration (Figure 3.2 as an example). This allowed to simulate only one phase in no-load condition to obtain the no-load fluxes and wrench for the whole machine.

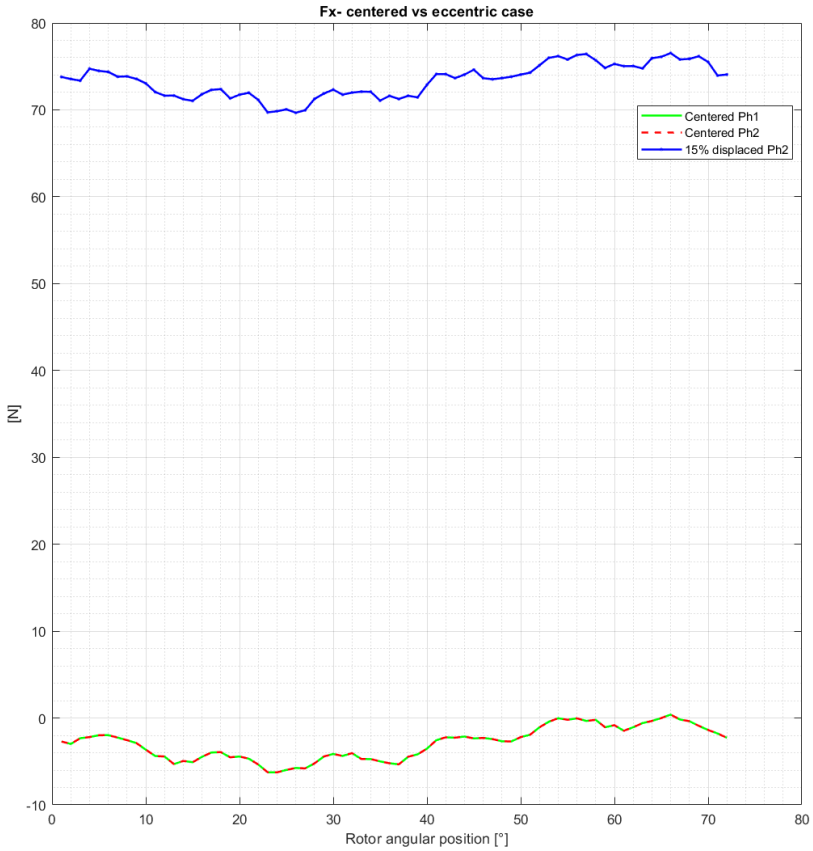

Figure 3.3: Fx in centered and eccentric case.

In eccentricity conditions, instead, some elements of the no-load wrench vary significantly for increasing eccentricity: while important radial forces are generated by the aforementioned unbalanced magnetic pull (UMP) in Figure 3.3, eccentricity has no discernible effect on the reluctance torque as long as it remains within the backup bearing's physical limitations. Indeed, even if the waveforms in Figure 3.4 might slightly differ, it is a matter of hundredths of Nm. Such stability suggests that, under normal operating conditions, the contribution of eccentricity to torque differences is minimal and does not compromise the reliability or predictability of the system's mechanical behaviour in terms of speed, while the radial position control may face stability issues. From these considerations, it could be convenient to avoid computing reluctance torque for eccentric configurations, but this aspect was not exploited to optimize the mapping procedure, since the radial forces would still have to be computed by executing the *PostProcessing.m* function explained in Section 2.2, hence without causing considerable computational savings.

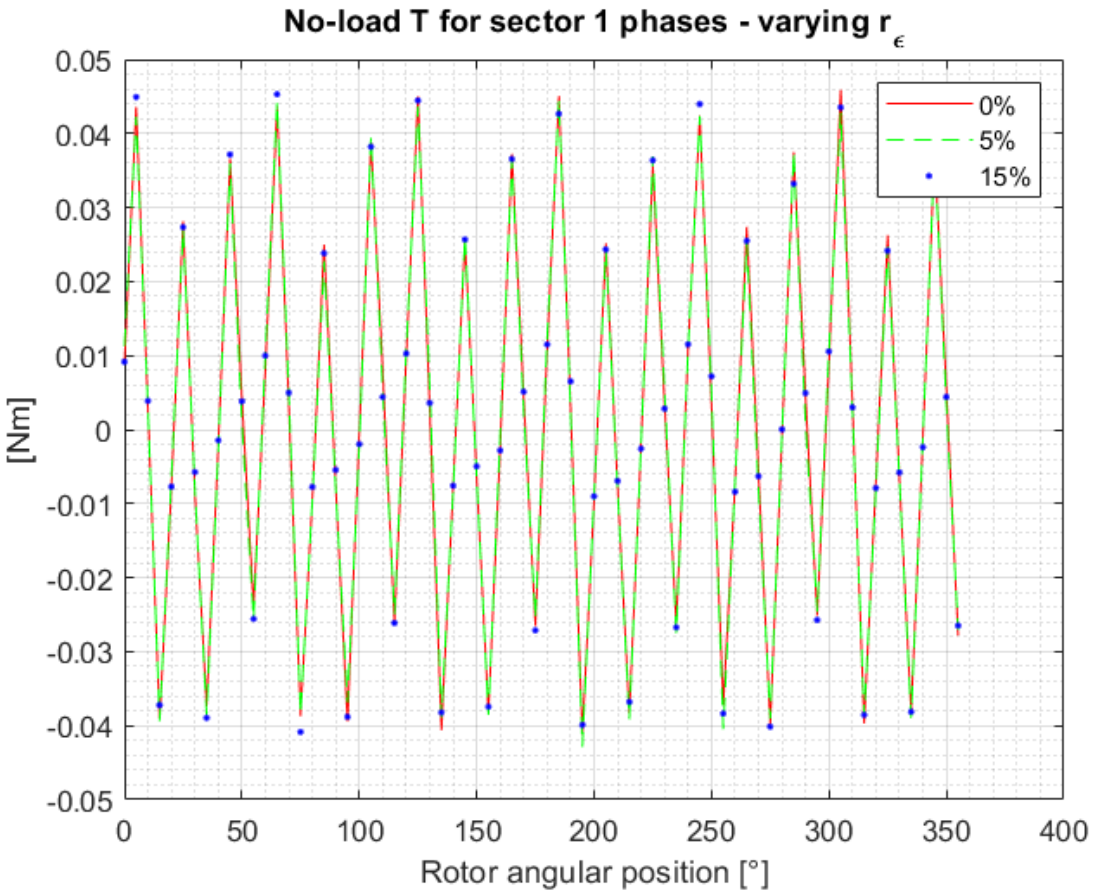

Figure 3.4: No-load torque for phase 1 at different eccentricities.

Another trivial simplification for the mapping procedure that was implemented in the *OutputsCalculation.m* MATLAB code consisted of avoiding simulating the model for all the eccentricity angles θ_ϵ, besides the first value, when the eccentricity radius r_ϵ was null, since all the combinations of $[(r_\epsilon = 0\%),\theta_\epsilon]$ would have identified the same rotor center, coinciding with the stator axis. In the procedure, after simulating the first point, a copy-paste snippet was added to complete the sequence and jump straight to the next rotor eccentric position. All these actions allowed to redefine the number of iterations needed to perform the mapping:

- $\gamma_I = [0, 1] \cdot 20$ A, and no-load analysis ($\gamma_I = 0$) was computed only for phase 1.
- for $r_\epsilon = 0$ %, no iteration over θ_ϵ was performed.

To account for rotor skewing in the FEM simulations, two approaches are possible.

- The first approach consists of simulating one third of the motor's active length and then summing three times the single-segment results, shifted by $\pm$ 5° to reflect the rotor skew.
- The second approach consists of simulating the full active length of the rotor and

then averaging the flux and wrench vectors obtained from the original simulation and two copies shifted by ± 5° with respect to the reference angle θ_m.

Both approaches produce equivalent results while simulating the effect of rotor skewing efficiently. The latter strategy was chosen, and the indexes of the rotor segments were computed according to the number of mapped angular rotor positions $n\theta_m$ for θ_m, starting from the first segment index n_{s1} as:

$$n_{s2} = mod(n_{s1} + \frac{\frac{\alpha_{skew}}{n_{segm}-1}}{\Delta\theta} - 1, n\theta_m) + 1 \tag{3.2}$$

$$n_{s3} = mod(n_{s1} - \frac{\frac{\alpha_{skew}}{n_{segm}-1}}{\Delta\theta} - 1, n\theta_m) + 1 \tag{3.3}$$

where $\Delta\theta = \frac{2\pi}{n\theta_m}$, α_{skew} is the total skewing angle in radians and n_{segm} represents the number of rotor segments. The subsequent sums and subtraction of 1 in the formula can be misleading, but those are essential to avoid software error due to zero-indexing of vectors in MATLAB.

For example, to obtain the linked flux on a given phase considering the three rotor segments, the indexes related to the rotor positions that segments 2 and 3 assume when segment 1 is at $\theta_{m1} = 0°$ ($n_{s1} = 1$), for $n\theta_m = 72$ ($\Delta\theta = 5°$) are:

$$n_{s2} = mod(1 + \frac{\frac{10°}{2}}{5°} - 1, 72) + 1 = 2 \tag{3.4}$$

$$n_{s3} = mod(1 - \frac{\frac{10°}{2}}{5°} - 1, 72) + 1 = 71 \tag{3.5}$$

where $\Delta\theta$ and α_{skew} were presented in degrees instead of radians for better readability. In this case, the resulting wrench and linked fluxes are obtained by averaging the results from samples number 71, 1 and 2, as the full motor length was simulated. Clearly, to implement this feature, it is essential to impose a consistent simulation set in the mapping simulation to ensure including the correct position of each rotor segment: this condition will be addressed in Section 3.2.1.

It is important to highlight that the last described procedure did not improve computational time or the number of iterations. On the contrary, it increased the minimum number of iterations, adding constraints on the mapping set of θ_m, but allowed to obtain a model with a higher level of accuracy regarding the real motor behaviour. Since it was not present in the original model, it was not included in the context of a comparative analysis, since it would have surely increased the error, but it has been implemented in the final model to take into account also this design aspect of the machine.

After all the mentioned strategies to reduce the computational effort of the mapping procedure, the updated simulation set would feature:

- 9 powered phases;

- 72 rotor angular positions, corresponding to a step $\Delta\theta_m = 5°$;
- 2 current values considering nominal current (+20 A) as well as no-load condition (0 A), but computed directly only for phase 1;
- 3 eccentricity radius values: $r_\epsilon = [0, 10, 50]$ % with respect to nominal airgap $g_0 = 1$ mm;
- 6 eccentricity angles: $\theta_\epsilon = [0, \frac{\pi}{6}, \frac{\pi}{3}, \pi, \frac{2\pi}{3}, \frac{5\pi}{6}]$;

The computation of the generalized number of performed simulations (1 for each combination of $[\theta_m,\gamma_I,r_\epsilon,\theta_\epsilon]$ per phase) is not as straightforward as the original one:

$$
\begin{aligned}
N_{sim,opt1} = & \\
& N_{sim}(\gamma_I = 0, r_\epsilon = 0\%, n_{ph} = 1) + N_{sim}(\gamma_I = 0, r_\epsilon \neq 0\%, n_{ph} = 1) + \\
& N_{sim}(\gamma_I = 20, r_\epsilon = 0\%, n_{ph} = 9) + N_{sim}(\gamma_I = 20, r_\epsilon \neq 0\%, n_{ph} = 9) \\
& = n\theta_m + n\theta_m \cdot (nr_\epsilon - 1) \cdot n\theta_\epsilon + n\theta_m \cdot n_{ph} + n\theta_m \cdot (nr_\epsilon - 1) \cdot n\theta_\epsilon \cdot n_{ph} \\
& = n\theta_m \cdot [1 + ((nr_\epsilon - 1) \cdot n\theta_\epsilon) + n_{ph} + ((nr_\epsilon - 1) \cdot n\theta_\epsilon \cdot n_{ph})] \\
& = n\theta_m \cdot [(1 + (nr_\epsilon - 1) \cdot n\theta_\epsilon) \cdot (1 + n_{ph})]
\end{aligned}
$$

The number of iterations can then be computed as:

$$N_{sim,opt1} = 72 \cdot [(1 + 2 \cdot 6) \cdot (1 + 9)] = 9360 \tag{3.6}$$

Where nr_ϵ and $n\theta_\epsilon$ represent the dimension of the mapped eccentricity radius and angle sets, respectively. The computational saving that can be computed focusing on the number of iterations only, and neglecting the computational time difference, is:

$$1 - \frac{9360}{17496} = 46.5\% \tag{3.7}$$

Simulations shown that the adoption of the new loose-meshed $.FEM$ model ensured a reduction in the simulation time of the single iteration, of:

$$100 \cdot (1 - \frac{n_{loose}}{n_{thick}}) = 100 \cdot (1 - \frac{5}{36}) \approx 86.2\% \tag{3.8}$$

The equivalent number of simulations can then be approximated as:

$$N_{sim,fast1} = (1 - 0.764) \cdot N_{sim,opt1} = (1 - 0.764) \cdot 9360 \approx 2209 \tag{3.9}$$

With a reduction of

$$1 - \frac{2209}{17496} = 87.4\% \tag{3.10}$$

```
Bearingless_AssignedLinear.FEM
Solution 1 of 72, Current: 20.0 A, Eccentricity: 0%, Angle: 0.0°
Elapsed time: 0h 0m 36s.
Bearingless_AssignedLinear_LowMesh.FEM
Solution 1 of 72, Current: 20.0 A, Eccentricity: 0%, Angle: 0.0°
Elapsed time: 0h 0m 5s.
fx >>
```

Figure 3.5: Computational time: original FEM model vs loose-meshed one.

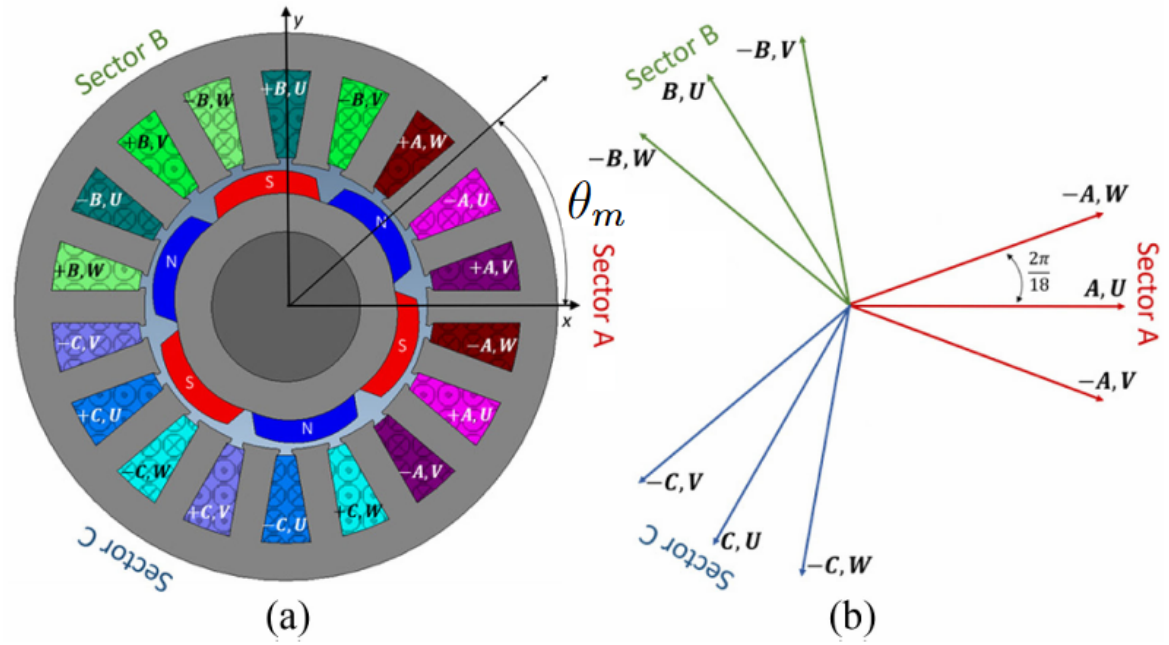

Figure 3.6: Schematic of the bearingless machine (a) and magnetic axes of the nine phases (b) [6].

with respect to the initial required computational effort. A key point to note from this section is that the new mapping has been performed by considering $n\theta_m = 72$ possible values for θ_m, in order for it to be consistent with the rotor skewing application, allowing to include in the simulation a minimum rotation of 5° (equal to $\frac{\alpha_{skew}}{2}$), while the original mapping included $n\theta_m = 36$ rotor positions only. For the same $n\theta_m$, the computational saving would've risen up to 93.7%.

3.2 Advanced inductance matrix mapping optimization

In order to further reduce the computational effort of the mapping procedure, additional optimization can be achieved by employing more advanced or aggressive strategies than

those introduced so far.
As a first step, it is quite intuitive that exploiting the linearity and the symmetry of the machine may allow to generalize the machine behaviour and reduce the initial data set required to perform a mapping. In particular, the motor structure suggests that, while imposing some constraints, the full mapping could be obtained without necessarily simulating the powering of all the nine phases, for example by exploiting the sectorial subdivision of the machine phases. Indeed, recalling Equation 3.1, the only remaining variables that haven't been modified yet are the number of mapped phases n_{ph} and the number of rotor positions $n\theta_m$. Even though it appears that the results obtained from a single sector could be extended to the whole machine with some rotational transformation, this work followed a more aggressive approach, trying to reduce even more the initial data set of the simulation.

3.2.1 Phase mapping optimization

At a first sight, it is possible to identify a repetitive pattern in the flux linkages that are obtained from the original mapping; in particular, the no-load fluxes depend solely on the magnets, which constitute the only source of MMF in the magnetic circuit. As a result, the no-load flux waveforms differ only by their initial phase, and can be aligned simply by applying a phase shift equal to the angular separation between the magnetic axes of the two phases.
The situation for flux linkages when a phase is powered is different: the waveforms are perfectly sinusoidal as expected, with the same period imposed by the permanent magnets, yet those feature slightly different amplitudes. Recalling the inductance matrix introduced in 2.2, it is important to highlight that the coefficients of L are the self and mutual inductances of the phases within the same sector, while M includes the mutual inductances between phases belonging to different sectors [19]. Therefore, the sector self-inductance matrix L, which contains the inductances of the phases within the same sector, can be rewritten as follows:

$$L = \begin{bmatrix} L_1 & M_1 & M_1 \\ M_1 & L_1 & M_{1d} \\ M_1 & M_{1d} & L_1 \end{bmatrix} \tag{3.11}$$

The aforementioned amplitude difference arises from the non-circulant nature of the self-inductance matrix. In a circulant matrix, each row is simply a one-step cyclic shift of the preceding one, a property that does not hold for this machine.
From the stator structure presented in Figure 3.6 it is possible to notice that, in sector 1 (A), the u-phase windings overlap v-phase and w-phase embracing 2 stator teeth; in contrast, only 1 stator tooth is embraced by the overlapping of v-phase and w-phase, which results in a smaller flux linkage between the two phases. Essentially, certain pairs of

phases subtend different spatial angles compared with others, which further accentuates the non-uniform coupling among them. For this reason, the phase inductance L differs from the one of a conventional three-phase motor because $M_{1d} \neq M_1$ [19]. The reason is the non-uniform distribution of the phases' magnetic axes along the stator periphery: as a consequence, the phase inductance matrix exhibits a non-circulant structure. In bearingless machines, where mechanical eccentricity is an intrinsic and often unavoidable condition, this behaviour becomes even more pronounced. This non-circulant feature, which becomes even more pronounced in machines with anisotropic rotor structures or under asymmetric supply conditions (e.g., module faults), implies that the interaction among winding modules cannot be treated using the standard orthonormal transformation that diagonalizes the inductance matrix: such an approach is valid only when the phase inductance matrix exhibits a circulant structure[8]. To overcome this feature of the machine,

$$\vartheta_{ij} = \vartheta_i - \vartheta_j$$

where ϑ_i and ϑ_j represent the angular positions of the magnetic axes of two generic phases i and j, has been computed for the whole machine. The goal was to find the smallest number of phases to simulate to be able to cover all the mutual angles ϑ_{ij} between the machine phases, since the mutual flux linkage between two windings is proportional to the angle between their magnetic axes. The first attempt was performed by feeding only phase 1, looking for a correspondence between the mutual angles (hence mutual flux linkage) over the whole matrix: the impossibility of completing the angular matrix below with a single-phase simulation is trivial, as there is not a complete match between all the phase angles relative to phase 1 magnetic axis ϑ_{j1}.

$$\begin{bmatrix}
 & 1 & 2 & 3 & 4 & 5 & 6 & 7 & 8 & 9 \\
1 & \vartheta_{11} & \vartheta_{21} & \vartheta_{31} & \vartheta_{41} & \vartheta_{51} & \vartheta_{61} & \vartheta_{71} & \vartheta_{81} & \vartheta_{91} \\
2 & \vartheta_{21} & \vartheta_{11} & - & \vartheta_{61} & \vartheta_{71} & - & \vartheta_{91} & \vartheta_{71} & - \\
3 & \vartheta_{31} & - & \vartheta_{11} & \vartheta_{91} & - & \vartheta_{41} & \vartheta_{81} & - & \vartheta_{71} \\
4 & \vartheta_{41} & \vartheta_{61} & \vartheta_{91} & \vartheta_{11} & \vartheta_{21} & \vartheta_{31} & \vartheta_{41} & \vartheta_{51} & \vartheta_{61} \\
5 & \vartheta_{51} & \vartheta_{71} & - & \vartheta_{21} & \vartheta_{11} & - & \vartheta_{61} & \vartheta_{41} & - \\
6 & \vartheta_{61} & - & \vartheta_{41} & \vartheta_{31} & - & \vartheta_{11} & \vartheta_{51} & - & \vartheta_{41} \\
7 & \vartheta_{71} & \vartheta_{91} & \vartheta_{81} & \vartheta_{41} & \vartheta_{61} & \vartheta_{51} & \vartheta_{11} & \vartheta_{21} & \vartheta_{31} \\
8 & \vartheta_{81} & \vartheta_{71} & - & \vartheta_{51} & \vartheta_{41} & - & \vartheta_{21} & \vartheta_{11} & - \\
9 & \vartheta_{91} & - & \vartheta_{71} & \vartheta_{61} & - & \vartheta_{41} & \vartheta_{31} & - & \vartheta_{11}
\end{bmatrix} \tag{3.12}$$

As visible in 3.12, the results obtained from phase 1 cannot be extended to the flux linkages between phases u and v of any three-phase system; hence either L_{vw},L_{wv} and M_{vw},M_{wv} of any sector, as a further confirmation of the non-circulant condition that makes the simulation of a second phase necessary to complete the original inductance matrix from

a limited sample of simulated phases. Indeed, the set of "inter-phase" angles that are obtained from phase 1, in degrees to ensure higher readability, is

$$\vartheta_{set} = [0°, -20°, 20°, 120°, 100°, 140°, 240°, 220°, 260°] \tag{3.13}$$

as introduced in Section 1.3. These angles, thanks to the machine periodicity, allow to complete most of the elements in 3.12, besides the mentioned angles

$$\vartheta_{23} = -40° \qquad \vartheta_{26} = -160° \qquad \vartheta_{29} = 80°$$

$$\vartheta_{53} = 80° \qquad \vartheta_{56} = -40° \qquad \vartheta_{59} = -160°$$

$$\vartheta_{83} = -160° \qquad \vartheta_{86} = 80° \qquad \vartheta_{89} = -40°$$

and their symmetric counterparts, which have not been included for the sake of brevity. A further simulation, including also the powering of the second phase, allows the completion of the mutual angles matrix in 3.12. From this table it's visible that the elements missing from 3.12 are computed from the simulation of phase 2.

$$\begin{bmatrix}
 & 1 & 2 & 3 & 4 & 5 & 6 & 7 & 8 & 9 \\
1 & \vartheta_{11} & -\vartheta_{21} & -\vartheta_{31} & -\vartheta_{41} & -\vartheta_{51} & -\vartheta_{61} & -\vartheta_{71} & -\vartheta_{81} & -\vartheta_{91} \\
2 & \vartheta_{21} & \vartheta_{11} & -\vartheta_{32} & -\vartheta_{81} & -\vartheta_{71} & -\vartheta_{62} & -\vartheta_{51} & -\vartheta_{41} & -\vartheta_{92} \\
3 & \vartheta_{31} & \vartheta_{32} & \vartheta_{11} & -\vartheta_{91} & -\vartheta_{92} & -\vartheta_{71} & -\vartheta_{61} & -\vartheta_{62} & -\vartheta_{41} \\
4 & \vartheta_{41} & \vartheta_{42} & \vartheta_{51} & \vartheta_{11} & -\vartheta_{31} & -\vartheta_{21} & -\vartheta_{71} & -\vartheta_{91} & -\vartheta_{81} \\
5 & \vartheta_{51} & \vartheta_{41} & \vartheta_{92} & \vartheta_{21} & \vartheta_{11} & -\vartheta_{32} & -\vartheta_{81} & -\vartheta_{71} & -\vartheta_{62} \\
6 & \vartheta_{61} & \vartheta_{62} & \vartheta_{41} & \vartheta_{31} & \vartheta_{32} & \vartheta_{11} & -\vartheta_{91} & -\vartheta_{92} & -\vartheta_{71} \\
7 & \vartheta_{71} & \vartheta_{91} & \vartheta_{81} & \vartheta_{41} & \vartheta_{61} & \vartheta_{51} & \vartheta_{11} & -\vartheta_{31} & -\vartheta_{21} \\
8 & \vartheta_{81} & \vartheta_{71} & \vartheta_{62} & \vartheta_{51} & \vartheta_{41} & \vartheta_{92} & \vartheta_{21} & \vartheta_{11} & -\vartheta_{32} \\
9 & \vartheta_{91} & \vartheta_{92} & \vartheta_{71} & \vartheta_{61} & \vartheta_{62} & \vartheta_{41} & \vartheta_{31} & \vartheta_{32} & \vartheta_{11}
\end{bmatrix} \tag{3.14}$$

From this result, a fast mapping procedure was implemented through a MATLAB script, in order to verify the feasibility and the accuracy of the previous considerations. The script completes the inductance matrix with a structure identical to the one shown above, and finally compares it with the original data to investigate on the validity of the approach. Some of the flux linkages are shown and commented.

As an example, the procedure to obtain the linked flux φ_{31} is shown in Figure 3.8: the original fluxes φ_{31} and φ_{13} are shown in Figure 3.7, from which it is possible to notice the feasibility of the approach.

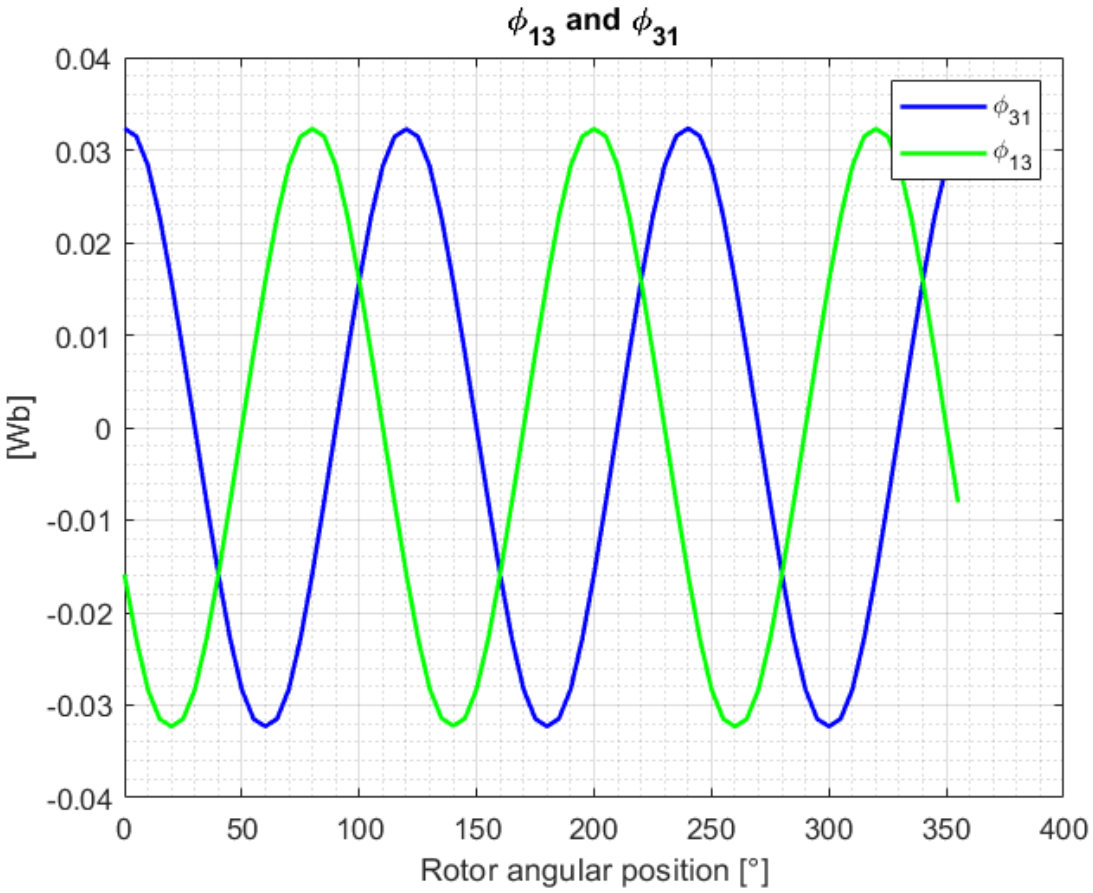

Figure 3.7: φ_{13} and φ_{31} waveforms.

In fact, the waveform of φ_{13} is obtained as in Figure 3.7, by mirroring φ_{31} and shifting its waveform by a number of steps corresponding to the phase shift between phase 1 and 3, to synchronize the reference frames of the two phases. The general shift, in terms of discrete steps along the given variables θ_m and θ_ϵ, is defined as:

$$shift_{\theta_m} = mod(\frac{\Delta\theta_{ij}}{\Delta\theta_m}, n\theta_m), \qquad shift_{\theta_\epsilon} = mod(\frac{\Delta\theta_{ij}}{\Delta\theta_\epsilon}, n\theta_\epsilon) \tag{3.15}$$

Where $\Delta\theta_{ij}$ [°] again represents the mechanical angle between the two considered phases, while $\Delta\theta_m$ and $\Delta\theta_\epsilon$[°] represent the resolution on the simulated variables defined by their sizes $n\theta_m$ and $n\theta_\epsilon$. It is important to clarify that, as discussed in Section 2.2, since the original sample of θ_m does not cover a full periodicity to avoid interpolation issues, the action of mirroring a sample, as if the rotor were rotating in the opposite verse, intrinsically includes a one-step shift that must be compensated on θ_m.

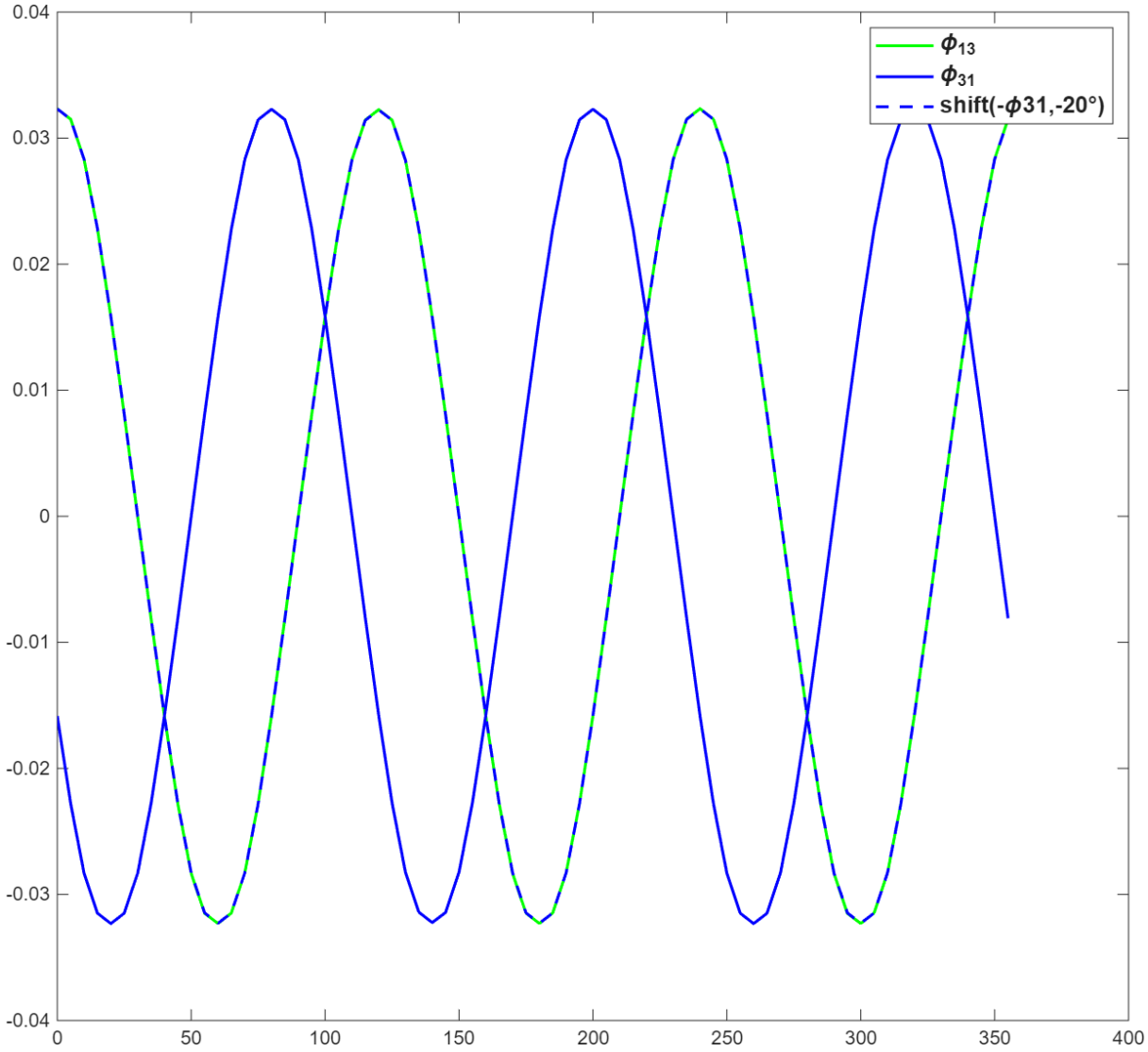

Figure 3.8: φ_{13} from φ_{31} through sign inversion and phase shift.

In fact, if two phases are wound with opposite winding directions, such as phases 1 and 3 (or, for this machine, phase u with respect to phase v, w of any sector, as stated in Chapter 1), the orientation of their reference surfaces (defined through the right-hand rule) is inverted. Although the magnetic flux crossing the two windings is physically identical, the change in reference orientation causes its signed contribution to be evaluated in opposite directions. For this reason, the flux linkage computed for one phase appears with the opposite sign when referred to the other phase, which required particular attention for a proper match of the results. Summarizing the procedure, in some cases it is necessary to invert the sign of the fluxes to take into consideration the sign of the relative angles or the phases' different winding directions, while in simpler cases, such as self-linked fluxes, a $circshift$ command is sufficient to match the waveforms.

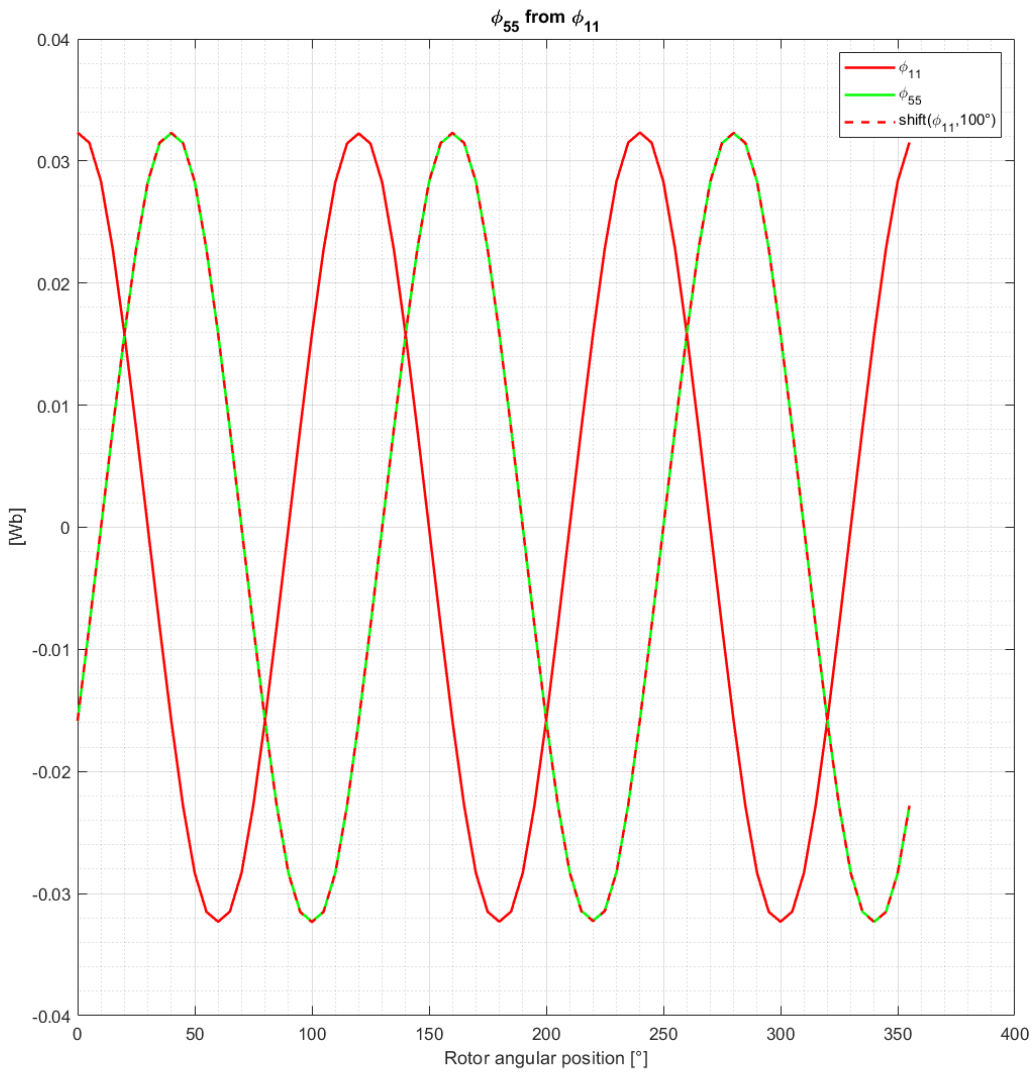

Figure 3.9: φ_{55} obtained from φ_{11}; sign inversion and phase shift.

As a further example, the obtainment of φ_{55} from φ_{11} is displayed in Figure 3.9, to highlight the sign change. Actually, φ_{55} could be easily obtained from φ_{22}, without any phase shift, since the angular displacement between phase 2 and 5 is 120°, equal to an electrical period. This is highlighted in Figure 3.10: to obtain φ_{77} from φ_{11} there is no need for sign inversion (both being phases u of the relative three-phase system) or phase shift due to the electrical periodicity of the machine.

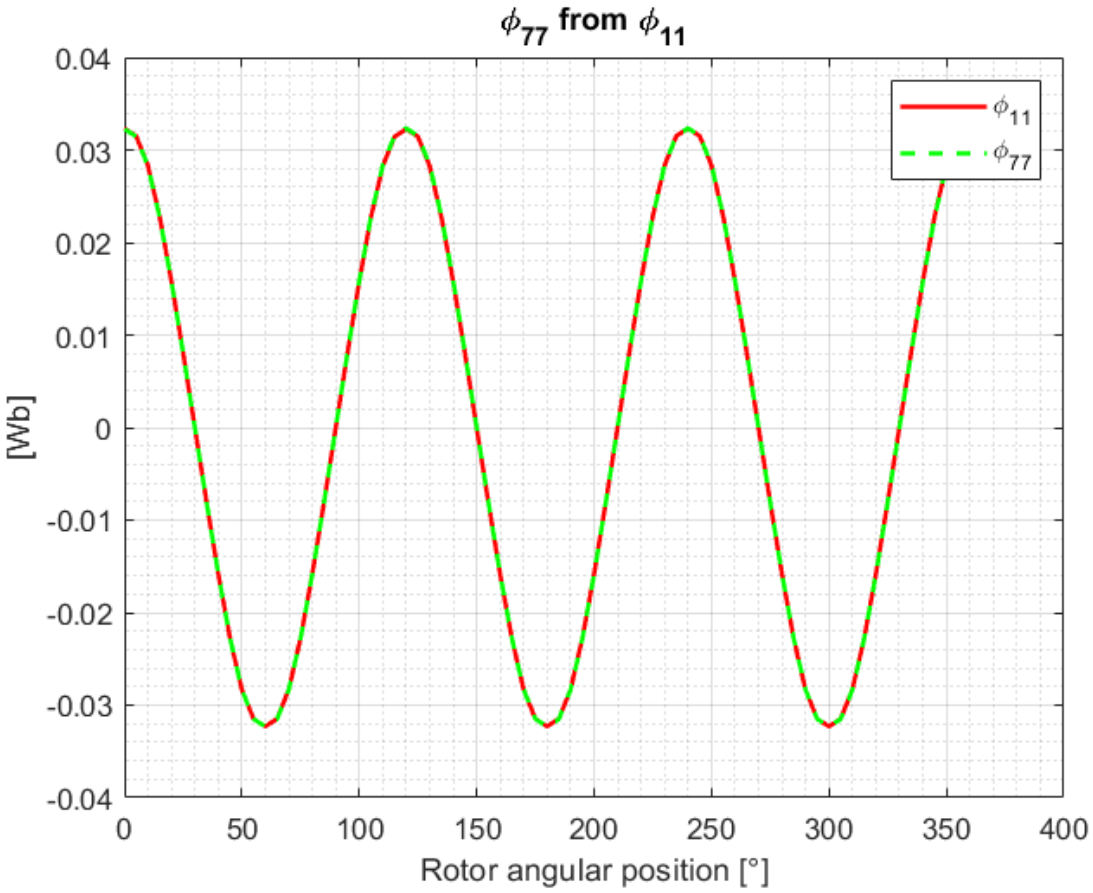

Figure 3.10: φ_{77} obtained from φ_{11}; exactly identical waveforms.

3.2.2 Constraints for fast mapping implementation

In order to correctly extend the results obtained for phases 1 and 2 to the entire machine, the selected combinations of eccentricity angles θ_ϵ and rotor positions θ_m must guarantee that every relative position between the rotor and the magnetic axes of all nine phases is represented within the reduced data set. To ensure this, a set of generalized constraints was introduced in the MATLAB *MainScript.m* script, to constrain the simulation to satisfy a set of initial conditions. Indeed, while the eccentricity radius r_ϵ does not cause any issue with the data replication, the number of mapped angular positions $n\theta_m$ and $n\theta_\epsilon$ must be selected carefully to verify the mentioned conditions: the general goal is to ensure that every phase winding faces the rotor in the exact same positions as the other phases. To do so, it is paramount that the set of angles corresponding to $n\theta_m$ and $n\theta_\epsilon$ include the magnetic axes of all the nine phases in Eq. 3.13.

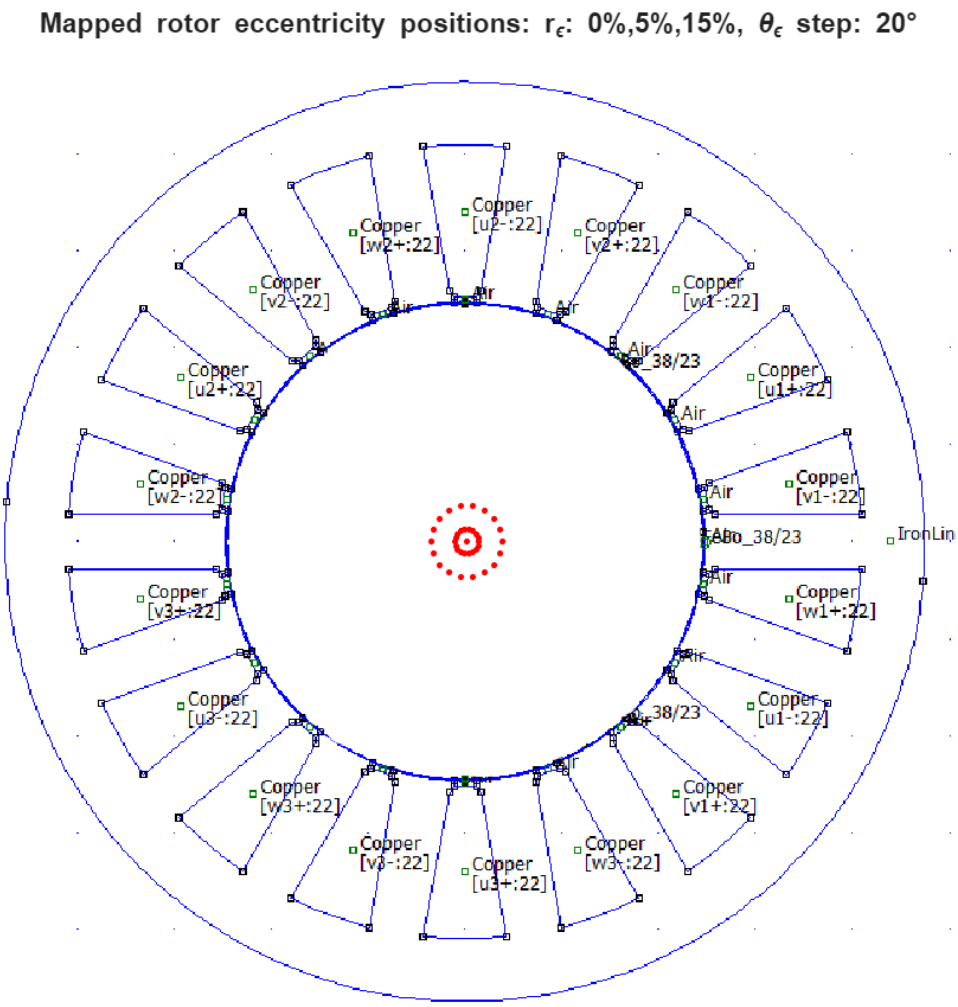

Figure 3.11: Rotor eccentric positions for $\Delta\theta_\epsilon = 20°$ and physically feasible eccentricity values.

To do so, the maximum allowed step for the mentioned angles must be equal to the minimum angular difference between phase axes, $\Delta\theta = 20°$, or a divisor of it: in this way, all the results obtained for the reciprocal positions between phases 1,2 and the rotor are suitable to be replicated for the remaining phases. Moreover, since the rotor segmentation was implemented in the model, the maximum step allowed for θ_m is therefore 5° or a divisor, in order to compute the average between the three segments as already discussed. Then, the minimum dimensions of the sets of simulated angles are respectively $n\theta_m$=72 ($\Delta\theta_m = 5°$) and $n\theta_\epsilon$=18 ($\Delta\theta_\epsilon = 20°$): in this way, the rotor position with respect to all phase axes is consistently mapped by the reduced simulation set.
For a clear representation of the minimal set of rotor positions to achieve fast mapping, Figure 3.13 and 3.12 are presented.

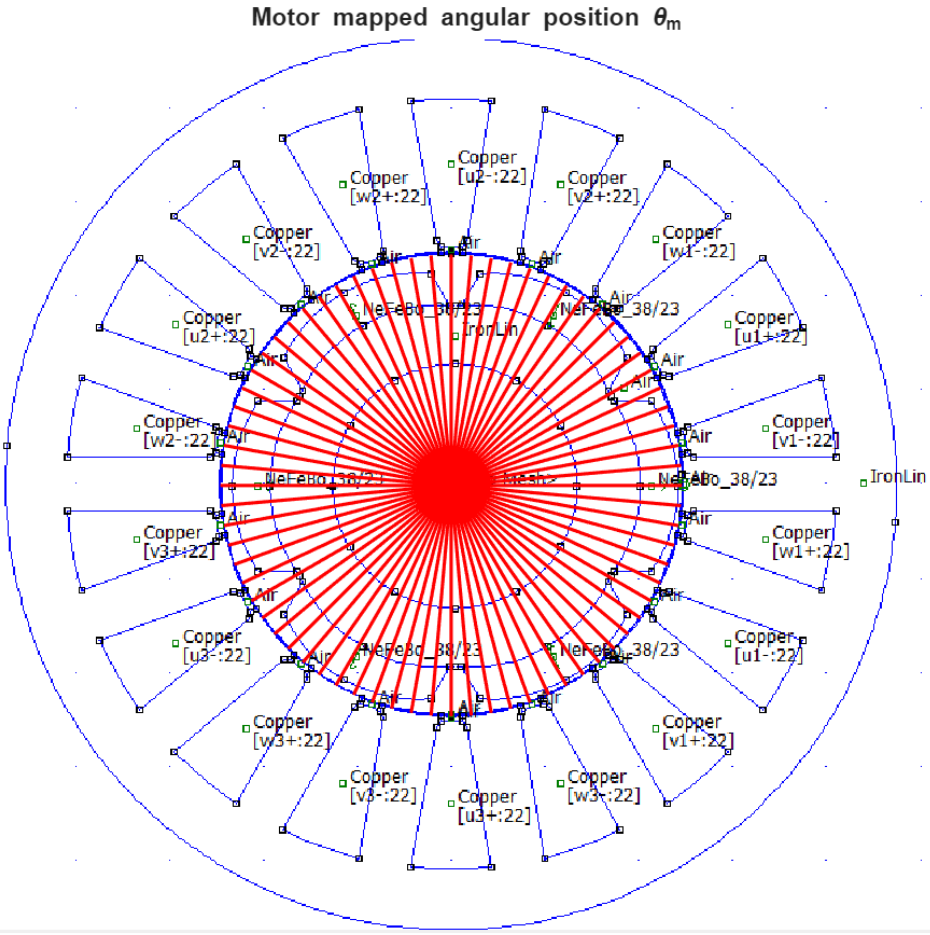

Figure 3.12: Rotor positions step $\Delta\theta_m = 5°$.

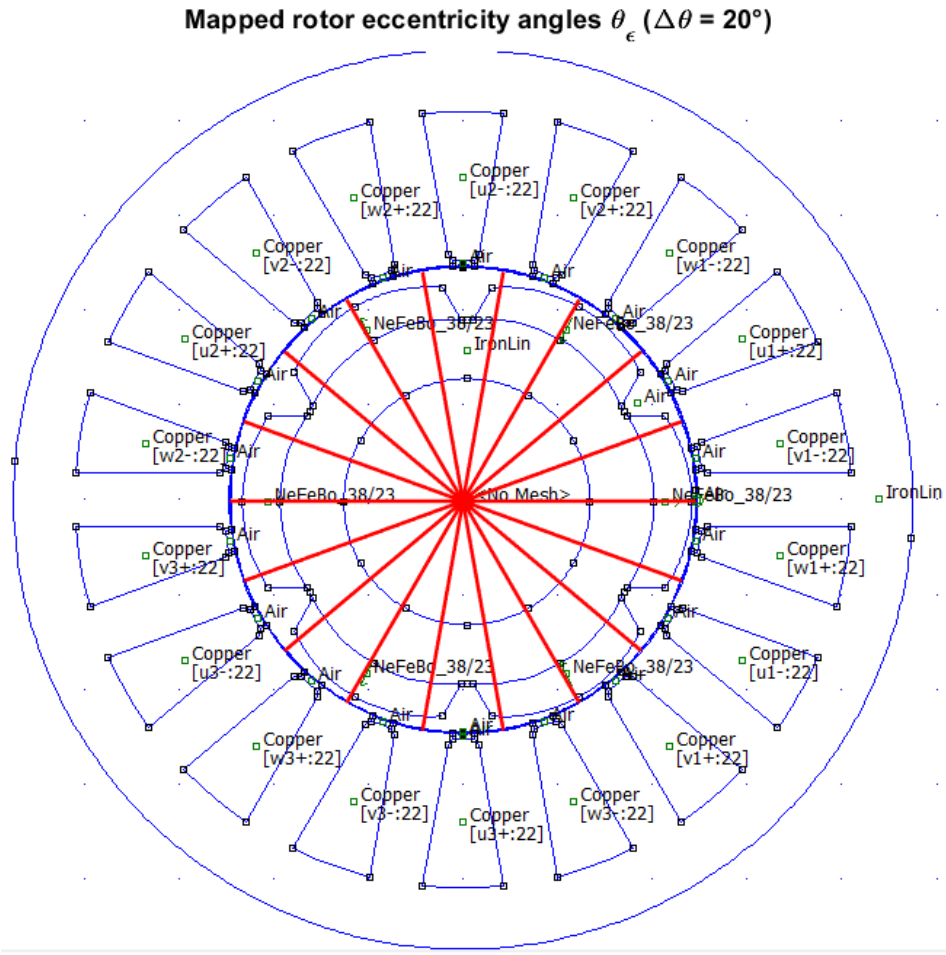

Figure 3.13: Minimum set of eccentricity angles θ_ϵ.

The completion of the inductance matrix, then, required to find a correspondence between the available data and the one to reconstruct: as a final validation step, the flux matrix obtained in 3.12 was reconstructed through a dedicated MATLAB script. The procedure also incorporated the number of shift steps applied along dimensions 1 and 4 (corresponding to θ_m and θ_ϵ and computed in 3.15) in order to generate a look-up table with which reconstruct the remaining entries.

9x9 cell

	1	2	3	4	5	6	7	8	9
1	[1,1,0,0,0,0,1]	[1,2,0,0,0,0,1]	[2,1,4,0,0,1,-1]	[4,1,48,0,0,12,1]	[5,1,52,0,0,13,-1]	[6,1,44,0,0,11,-1]	[4,1,48,0,0,12,1]	[6,1,44,0,0,11,-1]	[5,1,52,0,0,13,-1]
2	[2,1,0,0,0,0,1]	[2,2,0,0,0,0,1]	[3,2,64,0,0,16,1]	[6,1,40,0,0,10,1]	[4,1,44,0,0,11,-1]	[6,2,40,0,0,10,1]	[5,1,48,0,0,12,1]	[4,1,44,0,0,11,-1]	[9,2,16,0,0,4,1]
3	[3,1,0,0,0,0,1]	[3,2,0,0,0,0,1]	[1,1,4,0,0,1,-1]	[5,1,56,0,0,14,1]	[9,2,24,0,0,6,1]	[4,1,52,0,0,13,-1]	[6,1,48,0,0,12,1]	[6,2,48,0,0,12,1]	[4,1,52,0,0,13,-1]
4	[4,1,0,0,0,0,1]	[4,2,0,0,0,0,1]	[5,1,4,0,0,1,-1]	[1,1,24,0,0,6,1]	[2,1,28,0,0,7,-1]	[2,1,28,0,0,7,-1]	[4,1,0,0,0,0,1]	[5,1,4,0,0,1,-1]	[6,1,68,0,0,17,-1]
5	[5,1,0,0,0,0,1]	[5,2,0,0,0,0,1]	[9,2,40,0,0,10,1]	[2,1,24,0,0,6,1]	[1,1,20,0,0,5,-1]	[3,2,16,0,0,4,1]	[6,1,64,0,0,16,1]	[4,1,68,0,0,17,-1]	[6,2,64,0,0,16,1]
6	[6,1,0,0,0,0,1]	[6,2,0,0,0,0,1]	[4,1,4,0,0,1,-1]	[2,1,32,0,0,8,1]	[3,2,24,0,0,6,1]	[1,1,28,0,0,7,-1]	[5,1,8,0,0,2,1]	[9,2,48,0,0,12,1]	[4,1,4,0,0,1,-1]
7	[7,1,0,0,0,0,1]	[7,2,0,0,0,0,1]	[6,1,20,0,0,5,-1]	[4,1,24,0,0,6,1]	[6,1,20,0,0,5,-1]	[5,1,28,0,0,7,-1]	[1,1,48,0,0,12,1]	[2,1,52,0,0,13,-1]	[2,1,52,0,0,13,-1]
8	[8,1,0,0,0,0,1]	[8,2,0,0,0,0,1]	[6,2,16,0,0,4,1]	[5,1,24,0,0,6,1]	[4,1,20,0,0,5,-1]	[9,2,64,0,0,16,1]	[2,1,48,0,0,12,1]	[1,1,44,0,0,11,-1]	[3,2,40,0,0,10,1]
9	[9,1,0,0,0,0,1]	[9,2,0,0,0,0,1]	[4,1,28,0,0,7,-1]	[6,1,24,0,0,6,1]	[6,2,24,0,0,6,1]	[4,1,28,0,0,7,-1]	[2,1,56,0,0,14,1]	[3,2,48,0,0,12,1]	[1,1,52,0,0,13,-1]

Figure 3.14: Shift matrix from phases 1 and 2 maps.

In each cell of Figure 3.14, the first two numbers indicate the reference element from which the *circshift* operation is performed in MATLAB; the following four numbers

indicate the amounts of steps by which shifting over the four dimensions of the data (only θ_m and θ_ϵ have non-zero values, since shifting over currents or radius r_ϵ doesn't have any physical sense in the context of this work), and the final number is ± 1 according to the sign to apply to the original sample. The first two columns don't include any shift because those are part of the reduced mapping set.

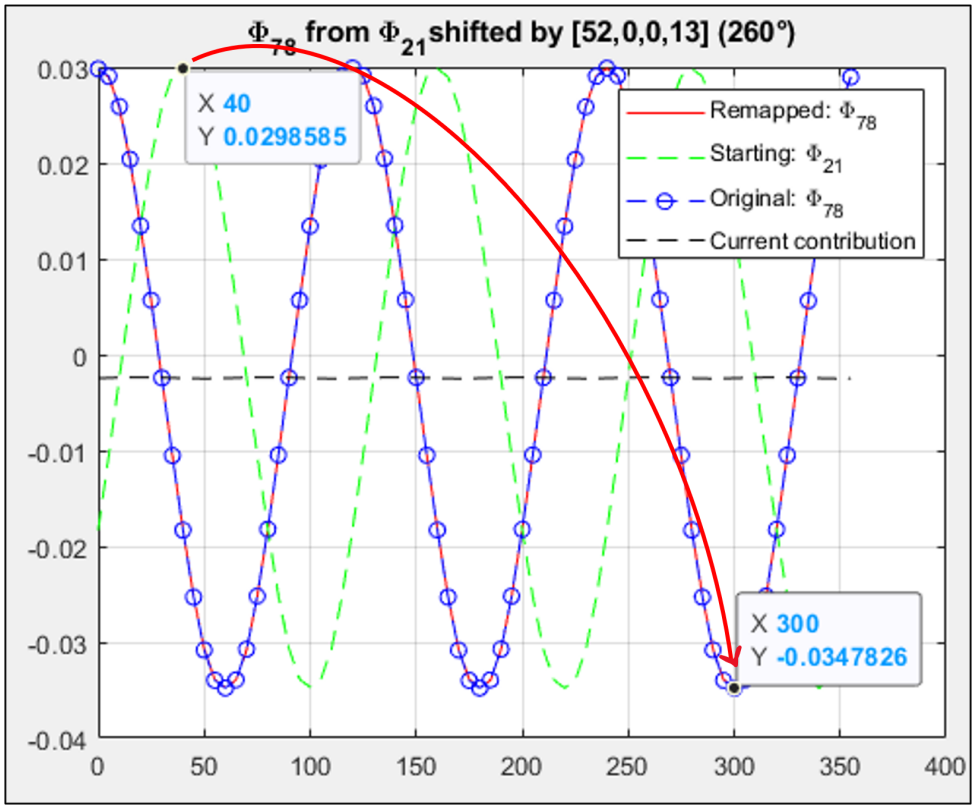

Figure 3.15: Application of circshift example. φ_{78} obtained from φ_{21}

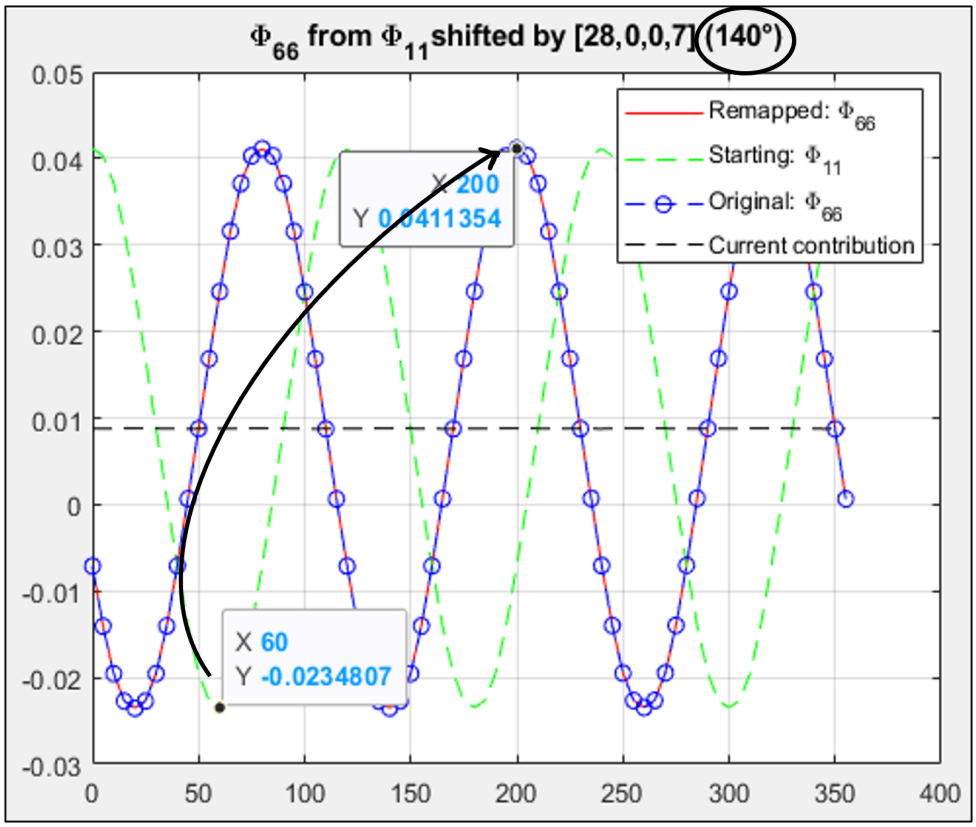

Figure 3.16: Application of circshift example. φ_{66} from φ_{11}

Figures 3.15 and 3.16 provide examples of the applications of the shifts matrix in 3.14: the red curve, which perfectly matches the original blue one, is obtained from the green one by shifting the sample by the two non-zero indexes from the figure title, corresponding to the angle indicated in brackets next to them. In both examples, the sign is inverted to match the results. According to the results of this simplification strategy, presented in 4, the simulation set can be reduced to:

- $n_{ph} = 2$ powered phases;
- 72 rotor angular positions, corresponding to a step $\Delta\theta_m = 5°$;
- 2 current values, including no-load condition (0 A) only for phase 1 and considering nominal current (+20 A) for the rest of the simulated n_{ph} phases;
- 3 eccentricity radius values: $r_\epsilon = [0, 5, 15]$ % with respect to nominal airgap $g_0 = 1$ mm;
- 18 eccentricity angles: $\theta_\epsilon = [0, \frac{\pi}{9}, \frac{2\pi}{9}, \ldots, \frac{8\pi}{9}, \frac{17\pi}{18}]$;

3.2.3 Reduced angular sampling strategy

The final variable for which an optimization is possible is the set of mapped angular positions θ_m: due to the machine structure, a trivial action could consist of simulating an

electrical period only, equal to one third of the original sample dimension, to subsequently replicate it for the whole machine. However, this thesis work aimed at further reducing the sample dimension. Indeed, the sinusoidal behaviour of the linked flux described earlier suggests that the complete map can be obtained by a quarter of an electrical period only, by applying a smart replication algorithm to extend the mapping to an electrical period, and finally replicate it to obtain the full mechanical period. Such strategy is shown in Figure 3.17 and 3.18.

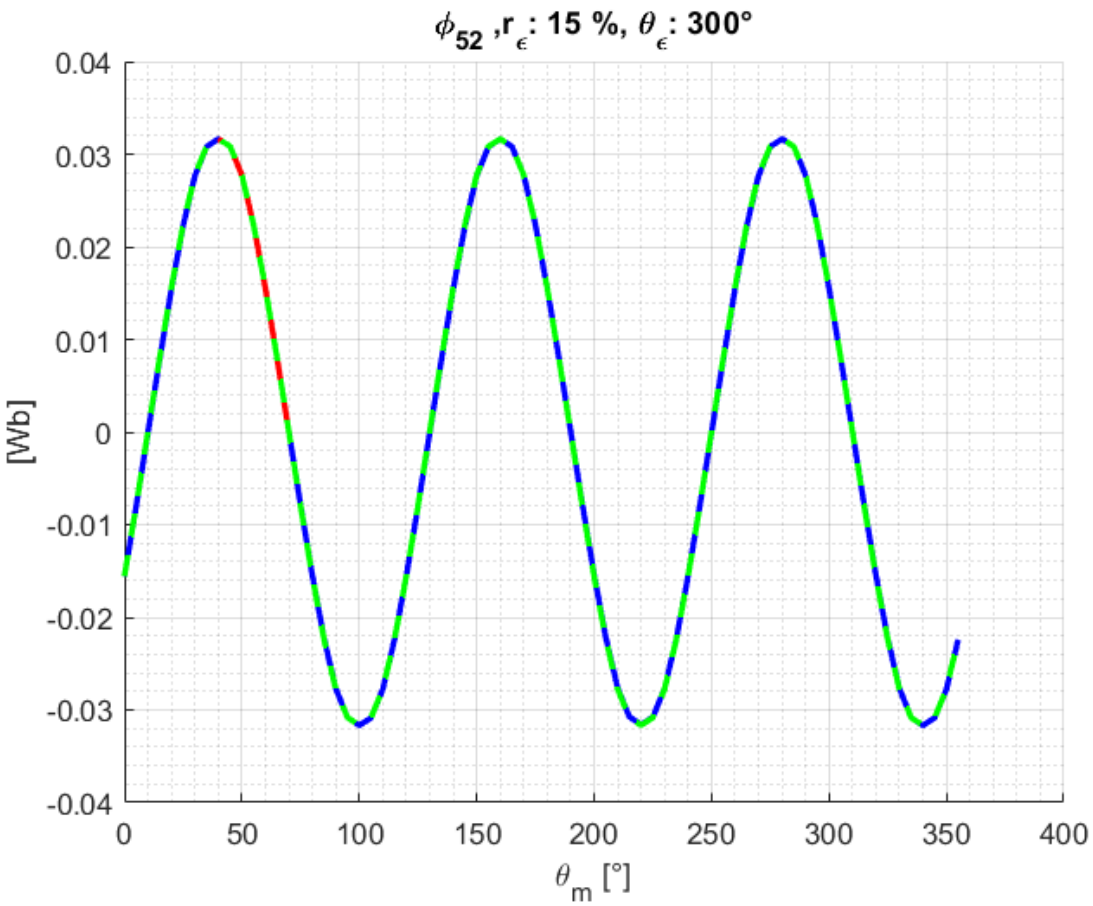

Figure 3.17: Example of no-load flux linkage from reduced angular sample.

The partial mapping was carried out by simulating a rotor rotation over a mechanical span of $\frac{\theta_{el}}{4} = 30°$, starting from a position in which a rotor magnet is aligned with each phase axis: this allows capturing the portion of the sinusoidal waveform that evolves from its extremum (either maximum or minimum, depending on the magnet pole) to the zero crossing.

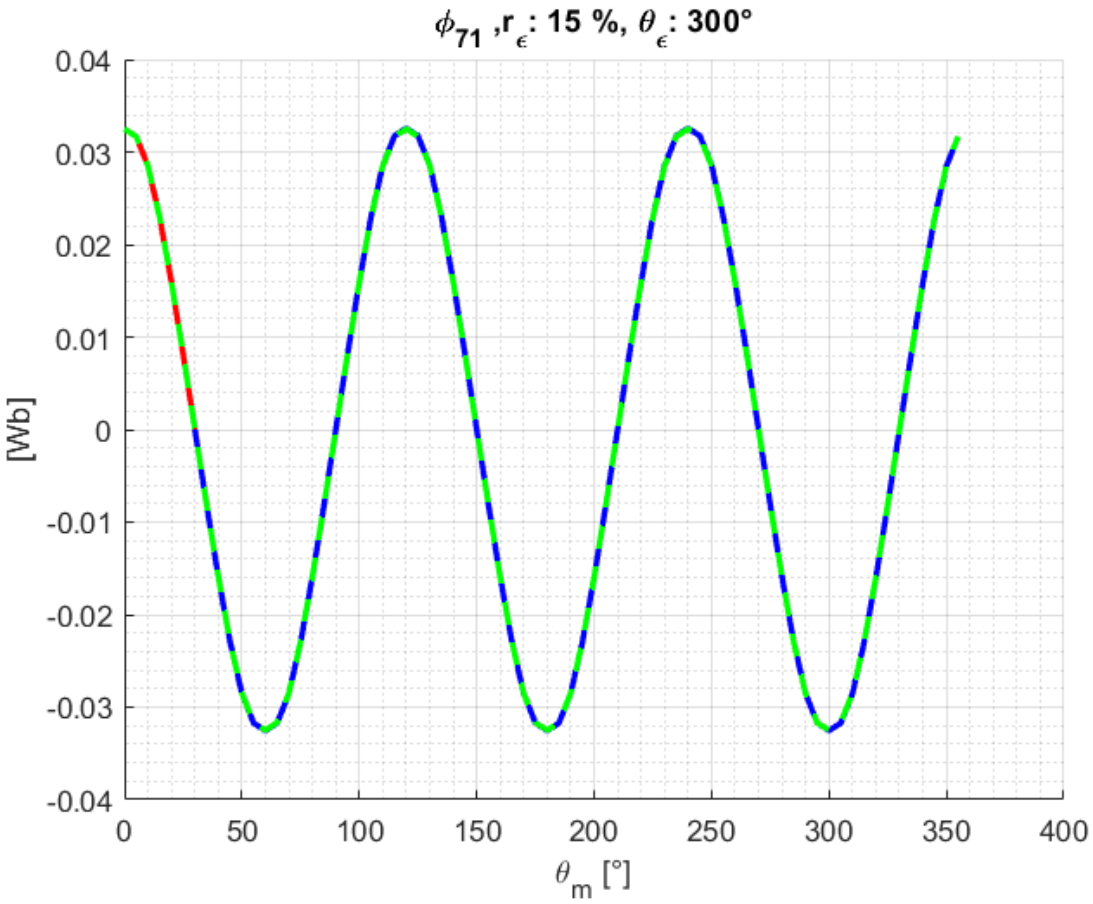

Figure 3.18: Example of no-load flux linkage from reduced angular sample.

Again, the machine structure helps reducing the initial simulation set, since the magnets' periodicity ensures that the mapping span corresponds to identical rotor positions for each u phase of the motor, and the same for each v and w. Indeed, mapping the rotor positions in the $\theta_m = [0, 5, \cdots, 25, 30]°$ interval allows to compute the no-load flux linkages for phases 1, 4 and 7, while $\theta_m = [20, 25, \cdots, 45, 50]°$ works for phases 2, 5 and 8, and $\theta_m = [-20, -15, \cdots, 5, 10]°$ works for phases 3, 6 and 9.
Considering the overall span for the nine phases of the motor, equal to 70° (-20° to 50° according to the sets presented above), this strategy would have worsened the computational efficiency of the algorithm, since choosing to map half an electrical period $\frac{\theta_{el}}{2} = 60°$ would have enabled the reconstruction of all waveforms using a smaller angular interval; nonetheless, exploiting the result obtained in Section 3.2.1 allows to consider just two phases out of nine, hence further reducing the mapped angular interval from 60° to 50° for the flux linkages from the PM.

In order to speed up the simulation of no-load inductance, the loose-meshed FEMM model introduced in Section 3.1 was further modified to obtain a new model, for which the inductance was independent from θ_m, hence simulating a perfectly isotropic rotor: the magnets are removed and the airgap region is replaced with a material with a different magnetic permeability, in order to obtain a material with intermediate magnetic

characteristics between air and magnet. The equivalent magnetic permeability can be computed in two ways:

- by maintaining constant the reluctance of the magnetic airgap considering the physical airgap and the magnet.

$$R_{eq} = R_\delta + R_m$$

$$\frac{\delta_{\text{mag}}}{\mu_{eq} S} = \frac{\delta_0 + \frac{h_{\text{mag}}}{\mu_r}}{\mu_0 S}$$

$$\frac{\delta_0 + h_{\text{mag}}}{\mu_{eq}} = \frac{\delta_0 \mu_r + h_{\text{mag}}}{\mu_0 \mu_r}$$

$$\mu_{eq} = \frac{\mu_0 \mu_r}{\delta_0 \mu_r + h_{\text{mag}}} (\delta_0 + h_{\text{mag}})$$

- as the weighted average of the magnetic airgap permeability considering actual airgap volume V_{AIR} and volume of the magnets V_{MAG}:

$$\mu_{eq} = \frac{\mu_0 V_{AIR} + \mu_r V_{MAG}}{V_{AIR} + V_{MAG}} \tag{3.16}$$

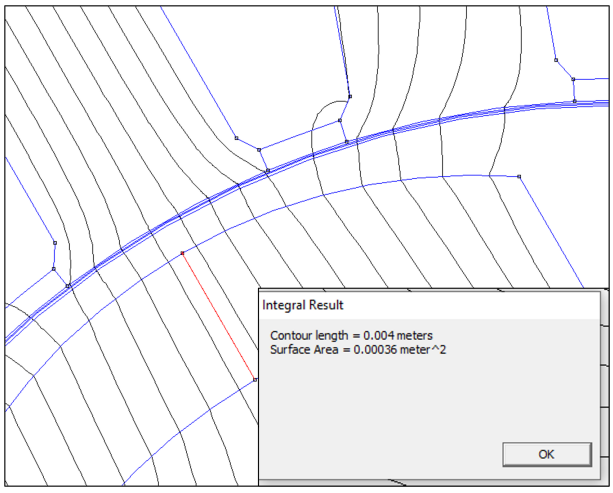

Figure 3.19: Magnet thickness measurement in FEMM.

The relative permeability to insert in the new *MagneticAir* material is obtained by dividing the resulting μ_{eq} by the permeability of vacuum μ_0. Even though both the approaches provide similar results, the second one was chosen, since it was simpler to create a MATLAB script able to modify the original FEMM model and compute the

volumes in the formula through the dedicated FEMM command *mo_blockintegral*(10) for the airgap (Fig. 3.20) and the magnets, rather than measuring the airgap and magnet thickness (Fig. 3.19).

The resulting equivalent magnetic permeability is $\mu_{eq} = 1.27985\ \frac{\mu H}{m}$, corresponding to $\mu_r = 1.01848$ relative permeability for the new material.

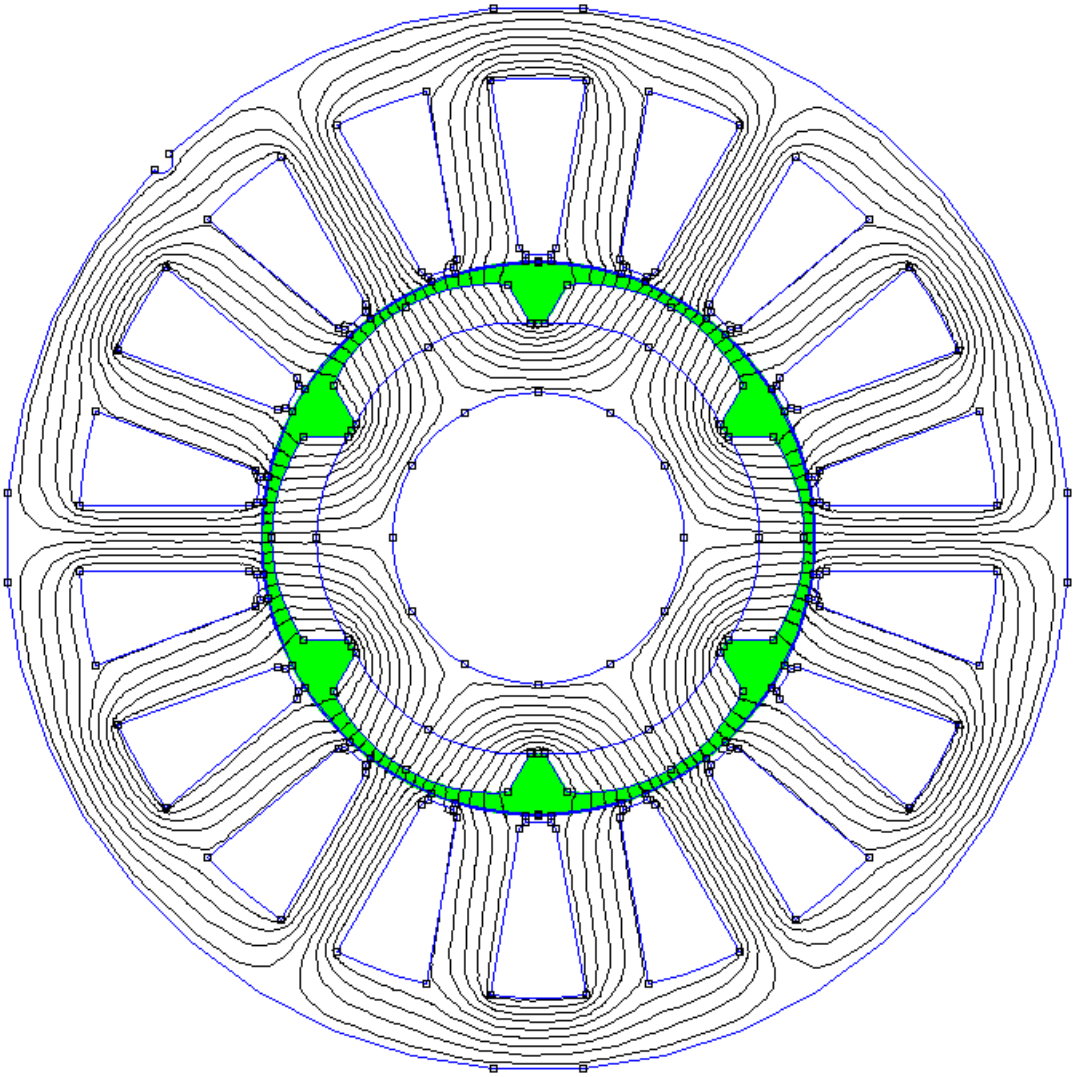

Figure 3.20: Airgap selection in FEMM.

The rotor becomes effectively isotropic when the permanent magnets are taken out and substituted with a hypothetical homogeneous material that has an equivalent magnetic permeability. The inductance and the total magnetic field distribution are strictly independent of the rotor angular position in the absence of eccentricity because the magnetic reluctance of the rotor in this configuration does not change with θ_m: since all angular positions are magnetically equivalent, rotating the rotor in the finite element model would not result in any significant change in the solution. However, the main concern about

this technique regards the fact that this invariance holds only as long as the airgap remains perfectly uniform, and once eccentricity is introduced, the assumption of isotropy is no longer sufficient to guarantee such angular independence. Even though the rotor is isotropic, the airgap ceases to be so, and the magnetic field becomes strongly influenced by the varying air-gap depth: in this condition, the flux density tends to concentrate in the region of minimum airgap and weaken in the region of maximum airgap, introducing a spatially non-uniform distribution of magnetic reluctance that depends on the rotor eccentricity angle θ_ϵ. Therefore, for control purposes, it is possible to consider eccentricity as an anisotropy which gets more pronounced for higher displacement, and considering developing a sensorless eccentricity control based on the variation of inductance due to eccentricity might be a valid option. The FEMM model definition was modified including an extra material, called "Magnetic Air", with the magnetic permeability from above, and linked to the newly created airgap. Without this approach, the different magnetic permeability of magnets would introduce a rotor anisotropy, which is reflected in a less accurate prediction of the inductance matrix.

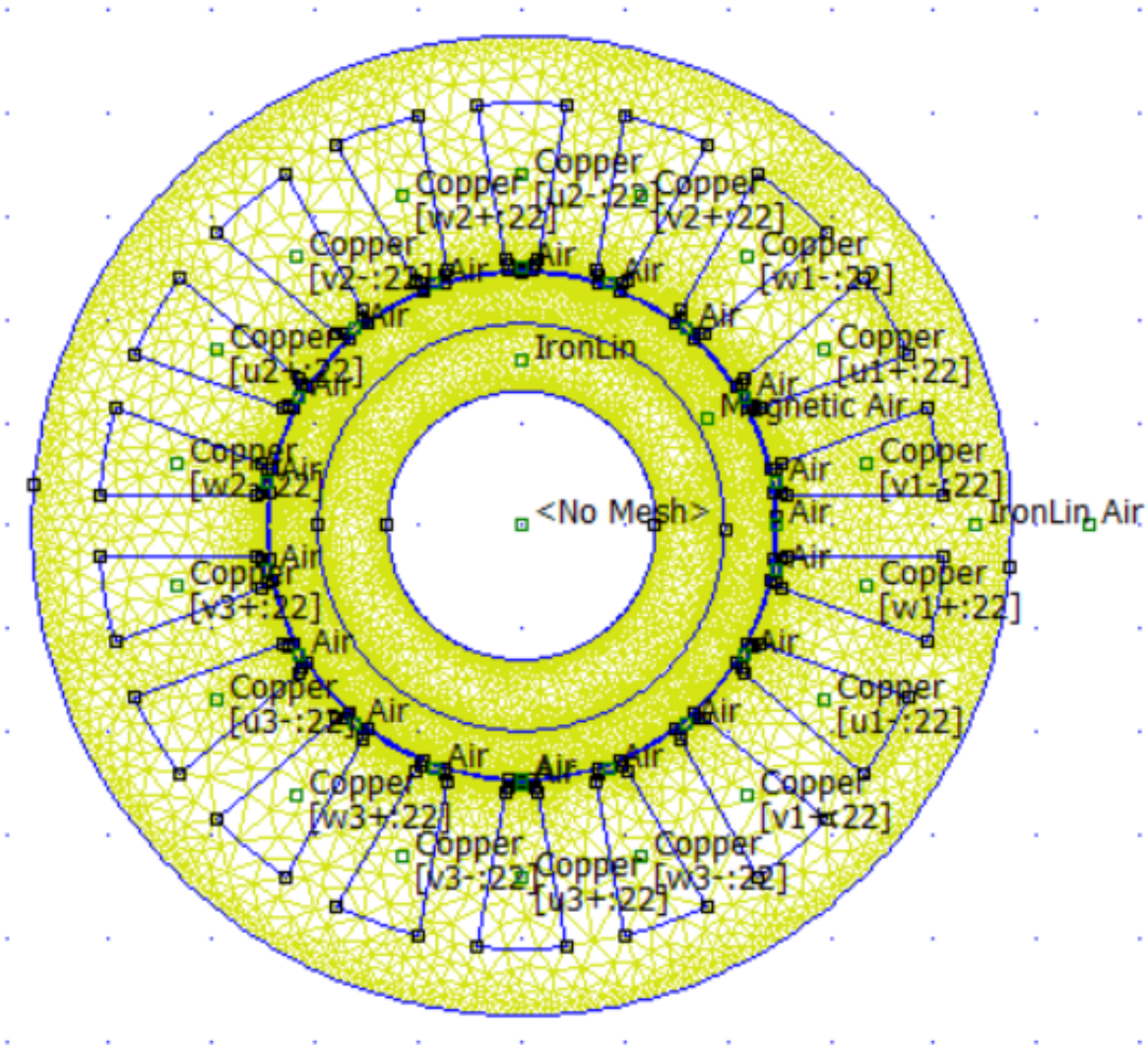

Figure 3.21: Magnetic Air model in FEMM.

This mapping strategy, combined with the previously introduced ones, allows to directly compute the armature flux linkage component and, by normalizing it with respect to the nominal current, the inductance matrix while reducing the computational effort of the simulation. Due to the different configurations of the new model with respect to the original one, an unavoidable error will be introduced by the adoption of this new "fake-rotor" model. Indeed, in the real machine simulation, the reluctance in the magnetic circuit is varying due to the motion of magnets while the rotor spins; with the newly introduced strategy, such oscillation is no longer considered, and this may cause a small error even in case the "Magnetic Air" was implemented in a thorough way.

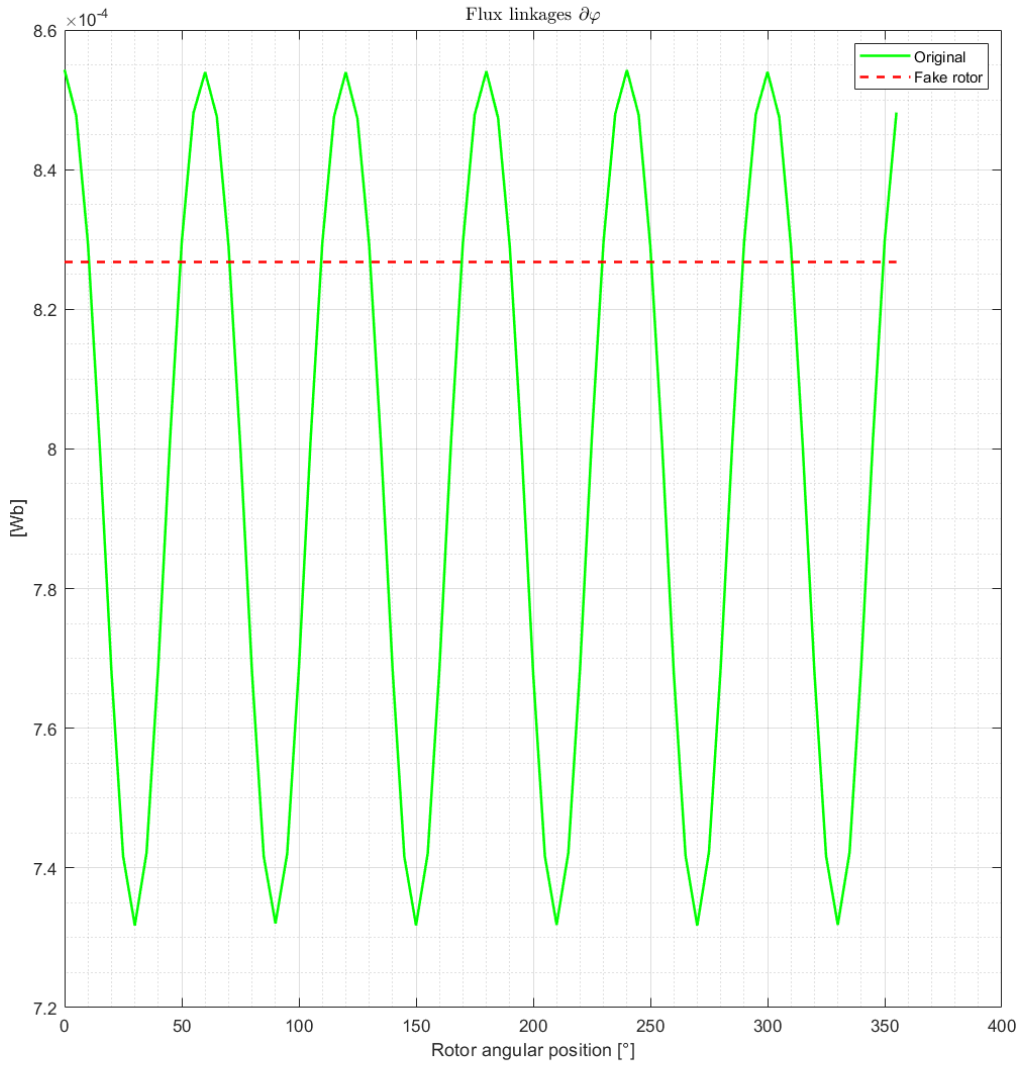

Figure 3.22: Intrinsic error for the fake-rotor model.

As an example, Figure 3.22 shows the difference between the new model results, in red, and its original counterpart computed as the difference between the $on - load$ and the

$no-load$ flux linkages, in order to neglect the PM contribution, for $\varphi_{32}(r_\epsilon : 15\%, \theta_\epsilon : 20°)$, hence for the highest eccentricity towards the considered phase 3. It is important to highlight that, in case a single rotor segment is simulated, the flux linkage magnitude is scaled down by a factor of 3, being proportional to the depth of the model: this aspect should be taken into consideration according to the selected simulation approach among the two mentioned in Section 3.1.

The average error is computed as

$$\varepsilon = 100 \cdot \frac{\varphi_{32,NEW} - \overline{\varphi_{32}}}{\overline{\varphi_{32}}} = 4\% \tag{3.17}$$

where $\overline{\varphi}_{32}$ is the average value of the green plot in Figure 3.22, resulting in an acceptable error for the considered model. The errors were computed as in Eq. 3.17 by considering separately every element of the 9x9 inductance matrix, for each combination of $[r_\epsilon, \theta_\epsilon]$, averaging the error over the 72 values of θ_m.

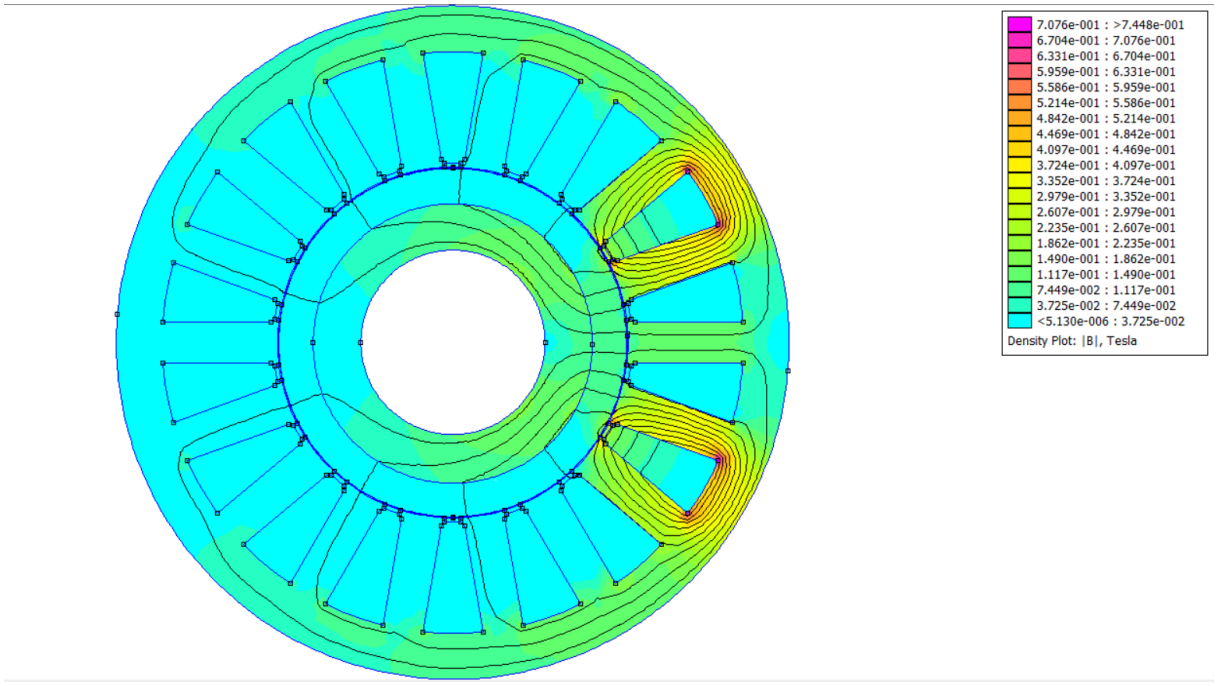

Figure 3.23: Fake-rotor model flux density while powering phase 1 only.

The errors span from values close to 0% up to approximately 8% at their peak. As shown in Figures 3.24 and 3.25, the overall trend indicates that larger deviations are generally associated with more pronounced eccentricities, oriented toward the magnetic axis of the phase for which the flux linkage is evaluated. This behaviour is expected, since displacement in the direction of the phase axis modifies more noticeably the local air-gap distribution and, consequently, the magnetic coupling.

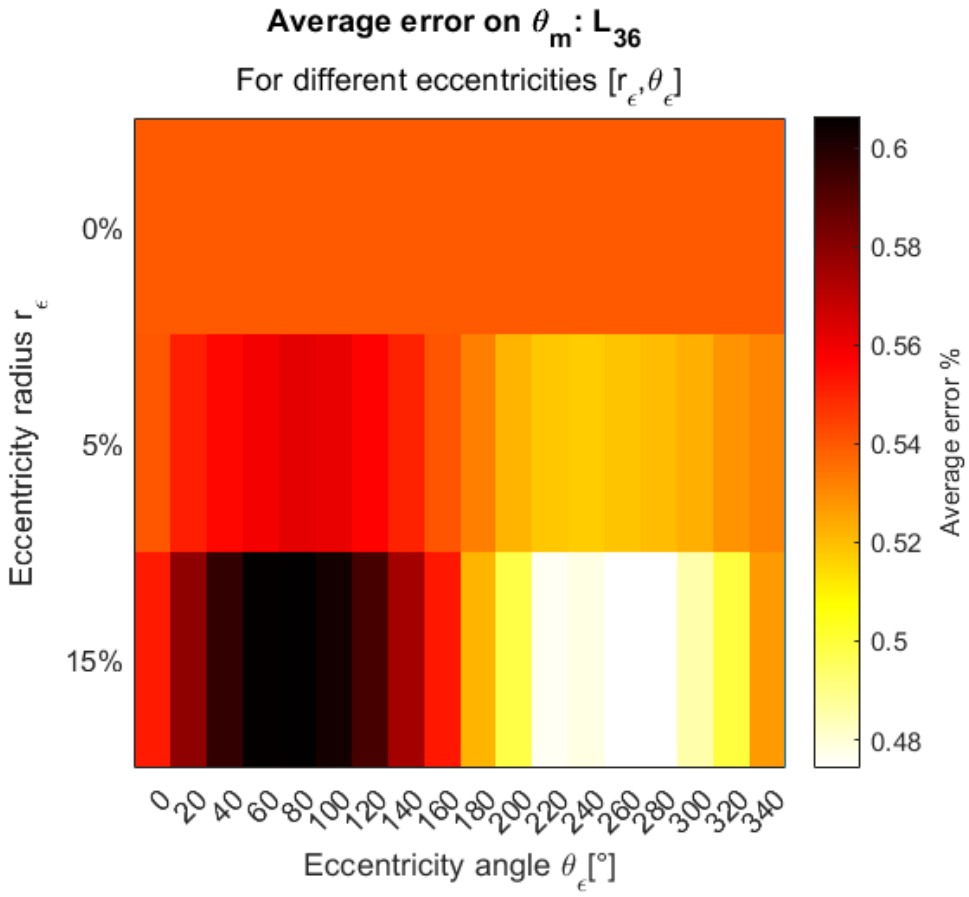

Figure 3.24: Average errors for L_{36}.

In the plots, the darkest cells indeed correspond to the direction aligned with the phase magnetic axis; however, even in such worst-case alignment, the error increases by only about 0.2%. Such a limited variation confirms that the modest eccentricity considered in this work does not significantly affect the accuracy of the model or the reliability of the inductance estimation. Finally, as expected, the error is identically constant when $r_\epsilon = 0\%$, because the rotor remains fixed in a single, perfectly concentric position on the xy plane, leaving the magnetic geometry unchanged across all angular evaluations.

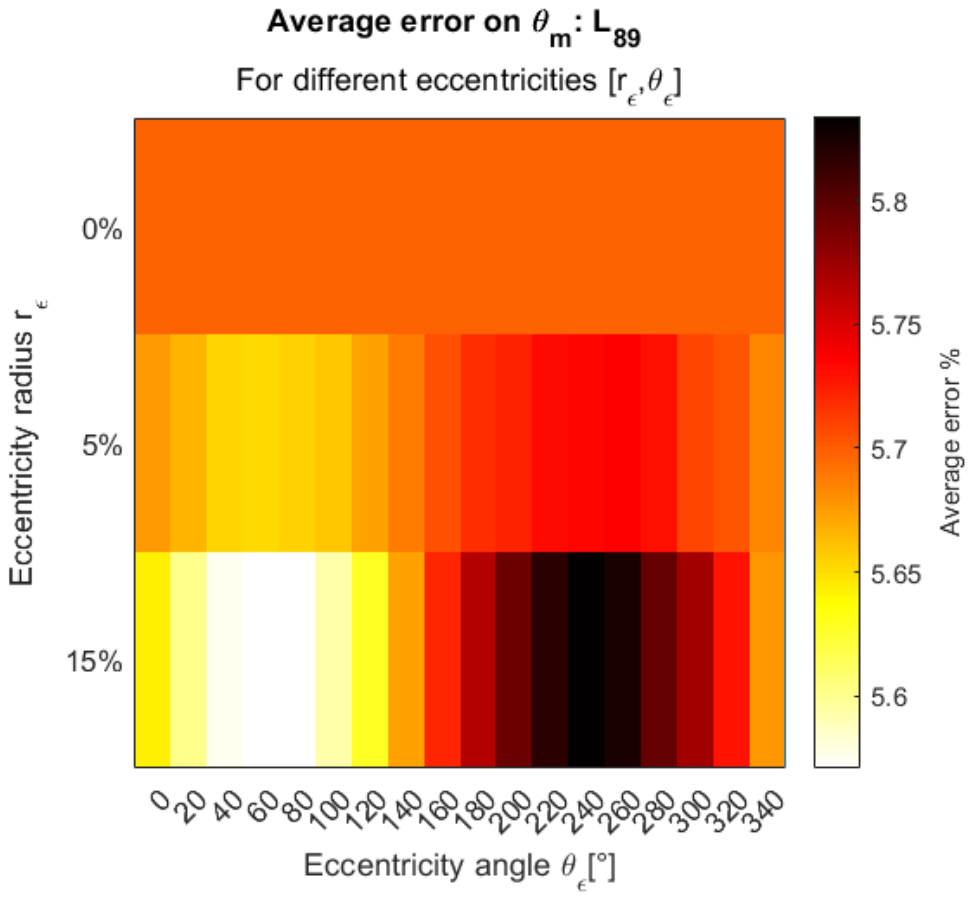

Figure 3.25: Average errors for L_{89}.

The average error over all the combinations of the model variables is presented in Figure 3.26, with an overall mean value of 3.74%.

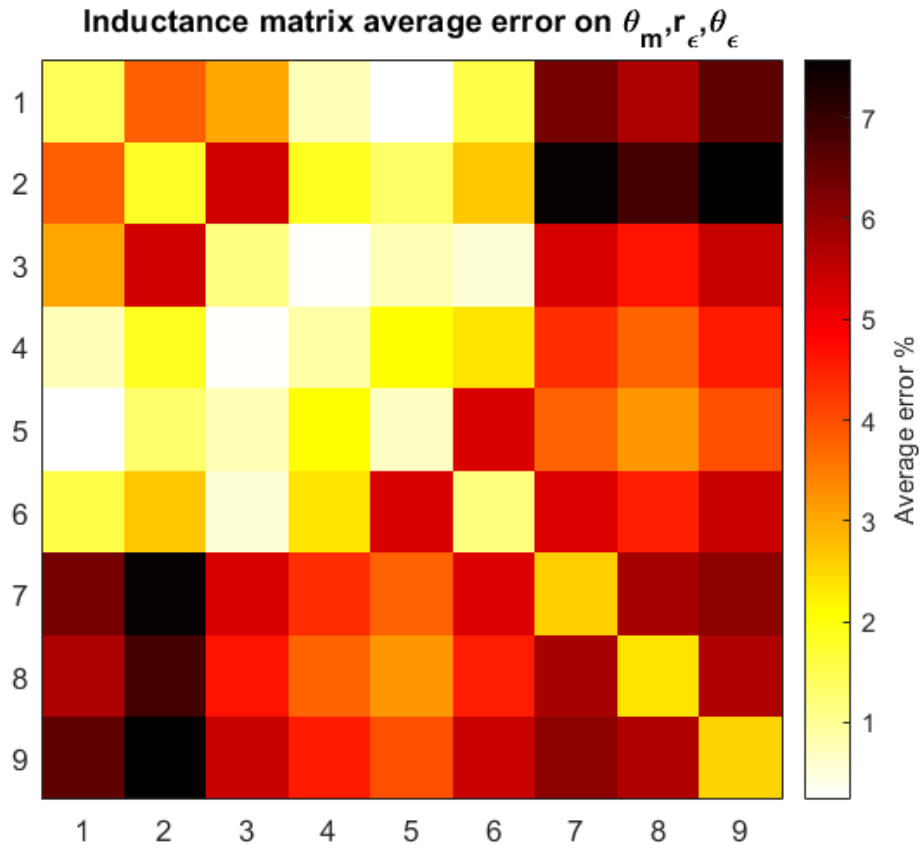

Figure 3.26: Mean error over all the inductance matrix variables.

3.3 Advanced wrench vector mapping optimization

The absence of permanent magnets in the new model introduced in the previous section makes it unsuitable for a consistent wrench analysis, as torque and radial forces arise primarily from the interaction between different orders of stator Magnetomotive Force (MMF) harmonics and those of the rotor, where the rotor's MMF is predominantly produced by the permanent magnets. In the absence of these magnets, the rotor no longer provides a fixed, spatially distributed MMF component, which fundamentally alters the electromagnetic interaction responsible for generating torque and radial forces. Without this interaction, any attempt to perform a conventional wrench analysis would yield results that are both incomplete and potentially misleading, as the main contributors to the wrench vector are no longer present. For this reason, the decoupling of the mapping procedure, considering two different models for fluxes and wrench, is necessary: the loose-meshed model still including the magnets was adopted again, during the optimization of the computational effort for the wrench vector coefficients $kW = [kFx, kFy, kT]^T$.
During the initial literature review phase of this work, [8] has gained particular attention: the article proposes a method that exploits a rotational matrix to obtain the wrench

coefficients from those of sector 1 only, after converting them into the dq reference frame. The method is applied to a bearingless Halbach array machine, which can be seen as a larger version of the machine under analysis. This machine features the same winding structure, but its rotor is equipped with an array of consecutive permanent magnets with different magnetization directions. The Halbach arrangement improves the sinusoidal waveform of the air-gap magnetomotive force. The approach presented in this work avoids the conversion in the dq reference frame, as that transformation does not modify the nature of the wrench vector, and there is no direct need of dq insights for control purposes. The control scheme is presented in Figure 3.27; a similar control scheme, that exploits the lookup tables resulting from this work, is described in detail in Chapter 5.

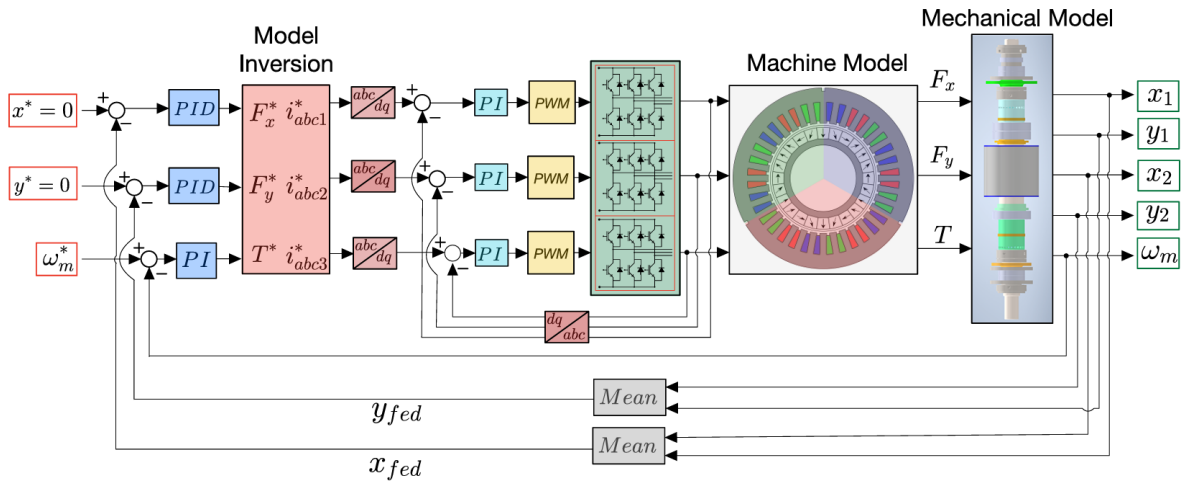

Figure 3.27: Control scheme of bearingless Halbach machine [7].

Under the hypothesis of linear behaviour, the wrench produced by the generic sector s can be expressed in terms of a linear matrix equation:

$$W^i(i_d^i, i_q^i, \theta_{el}^i) = R^i K_{dq}^1(\theta_{el})[i_d^i i_q^i]^T \tag{3.18}$$

Where K_{dq}^1 is the matrix of wrench coefficients of sector 1 and R^i is a rotational transformation defined as

$$R^i = \begin{bmatrix} cos\Delta\theta_m^i & -sin\Delta\theta_m^i & 0 \\ sin\Delta\theta_m^i & cos\Delta\theta_m^i & 0 \\ 0 & 0 & 1 \end{bmatrix} \tag{3.19}$$

where $\Delta\theta_m^i$ represents the axis of the $i-th$ sector, hence either 0, $\frac{2\pi}{3}$ or $\frac{4\pi}{3}$. As explained earlier in this work, under the assumption of linear behaviour and negligible cross-coupling between the sectors, the matrix K_{dq}^i defining the relationship between the sector wrench W^i and the respective current components, is independent from the current components of the other sectors.

Under this hypothesis, the overall wrench produced by the machine can be expressed as:

$$W = \sum_{i=1}^{n} R^i K^1_{dq}(\theta_{el})[i^i_d i^i_q]^T = K_{dq}(\theta_{el}) i_{dq} \tag{3.20}$$

Where K_{dq} and i_{dq} are defined as:

$$K_{dq} = [K^1_{dq}, R^2 K^1_{dq}, R^3 K^1_{dq}] \tag{3.21}$$

$$i_{dq} = [i^1_d, i^1_q, i^2_d, i^2_q, i^3_d, i^3_q] \tag{3.22}$$

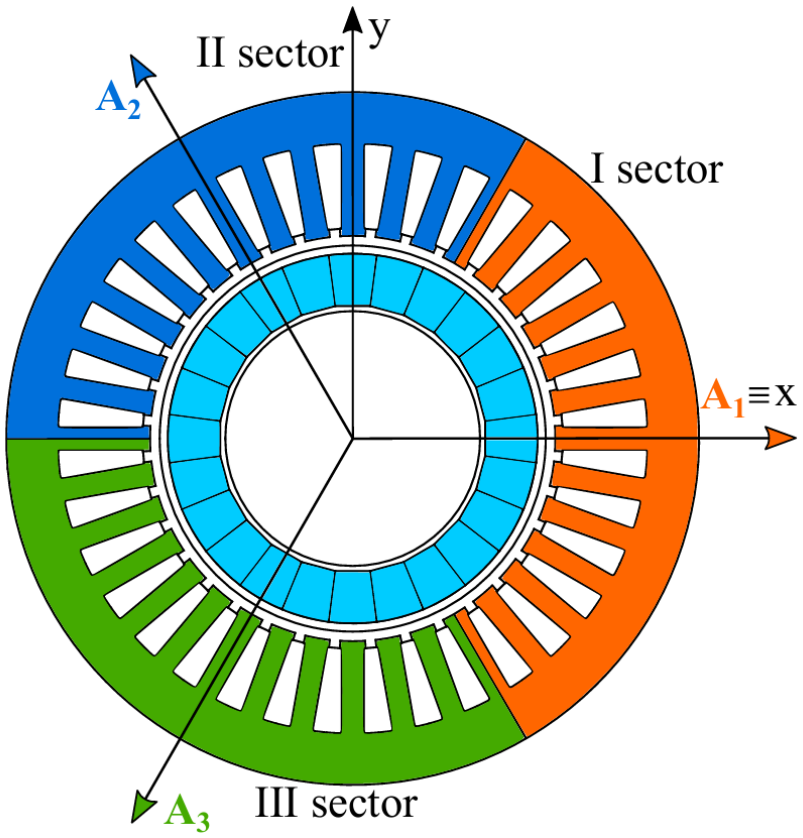

Figure 3.28: Halbach array bearingless machine [8].

In order to investigate on the feasibility of this approach, the wrench coefficients from sector 1 K^1_{abc} were obtained from the full mapping based on the loose-meshed $.FEM$ model, by normalizing F_x, F_y, T with respect to the machine nominal current, as:

$$K^1_{abc} = [\frac{F^1_x}{I_{nom}}; \frac{F^1_y}{I_{nom}}; \frac{T^1}{I_{nom}}] \tag{3.23}$$

Then, the wrench coefficients matrix for the whole machine K_{abc} was computed without moving to the dq referenced frame as specified earlier, but only applying the rotational

matrix from Eq. 3.19, as:

$$K_{abc} = [K^1_{abc}, R^2 K^1_{abc}, R^3 K^1_{abc}] \tag{3.24}$$

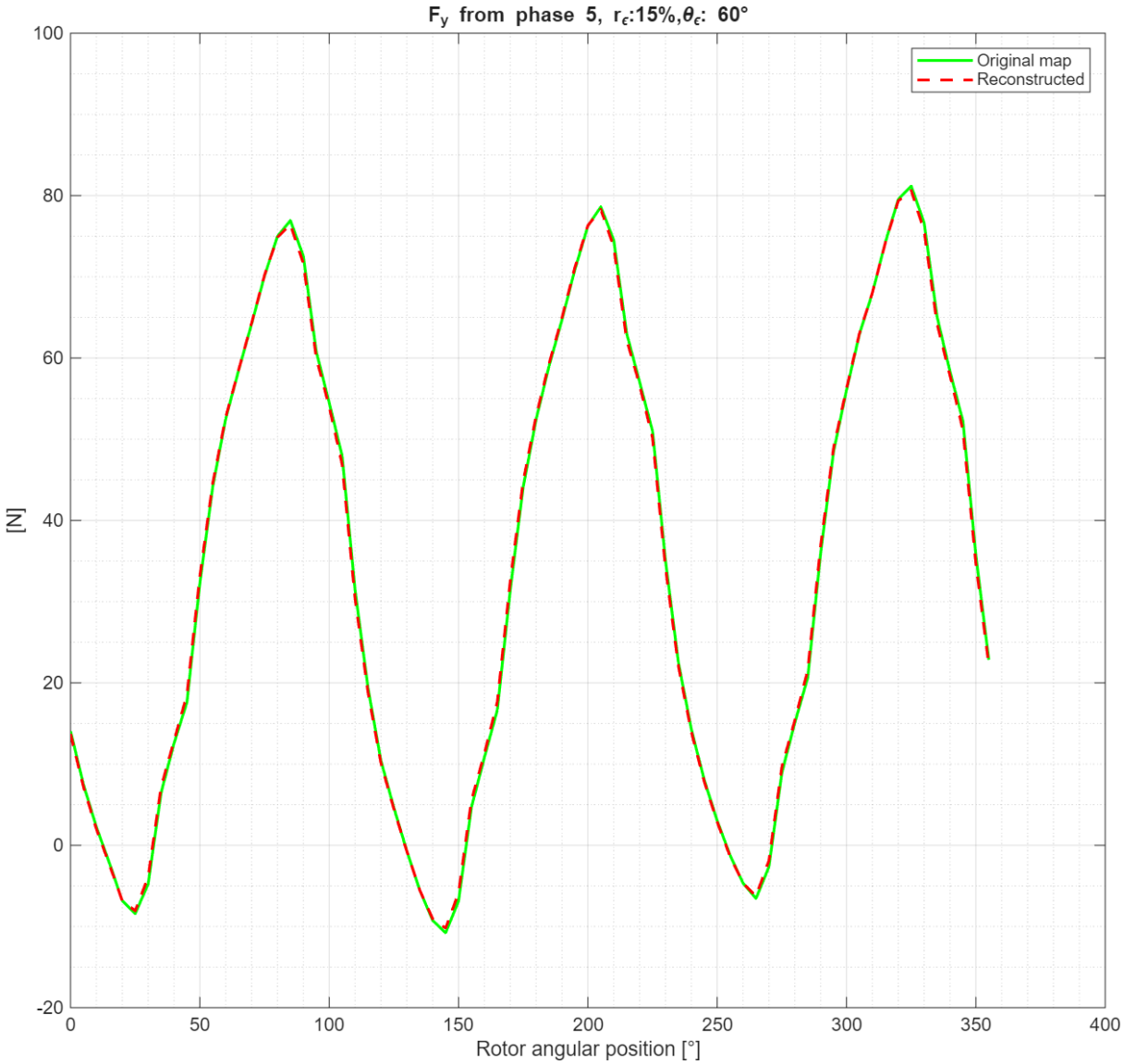

Figure 3.29: F_y from phase 5. Original vs reconstruction.

The results of the wrench comparison - original and newly obtained from rotated coefficients - is qualitatively shown in Figures 3.29 and 3.30, in which it was demonstrated the applicability of the rotational transformation described in 3.18 to the wrench coefficients of sector 1 in *abc* frame to obtain the wrench coefficients of sectors 2 and 3, with an acceptable level of accuracy, hence by reducing the computational effort by 66%.

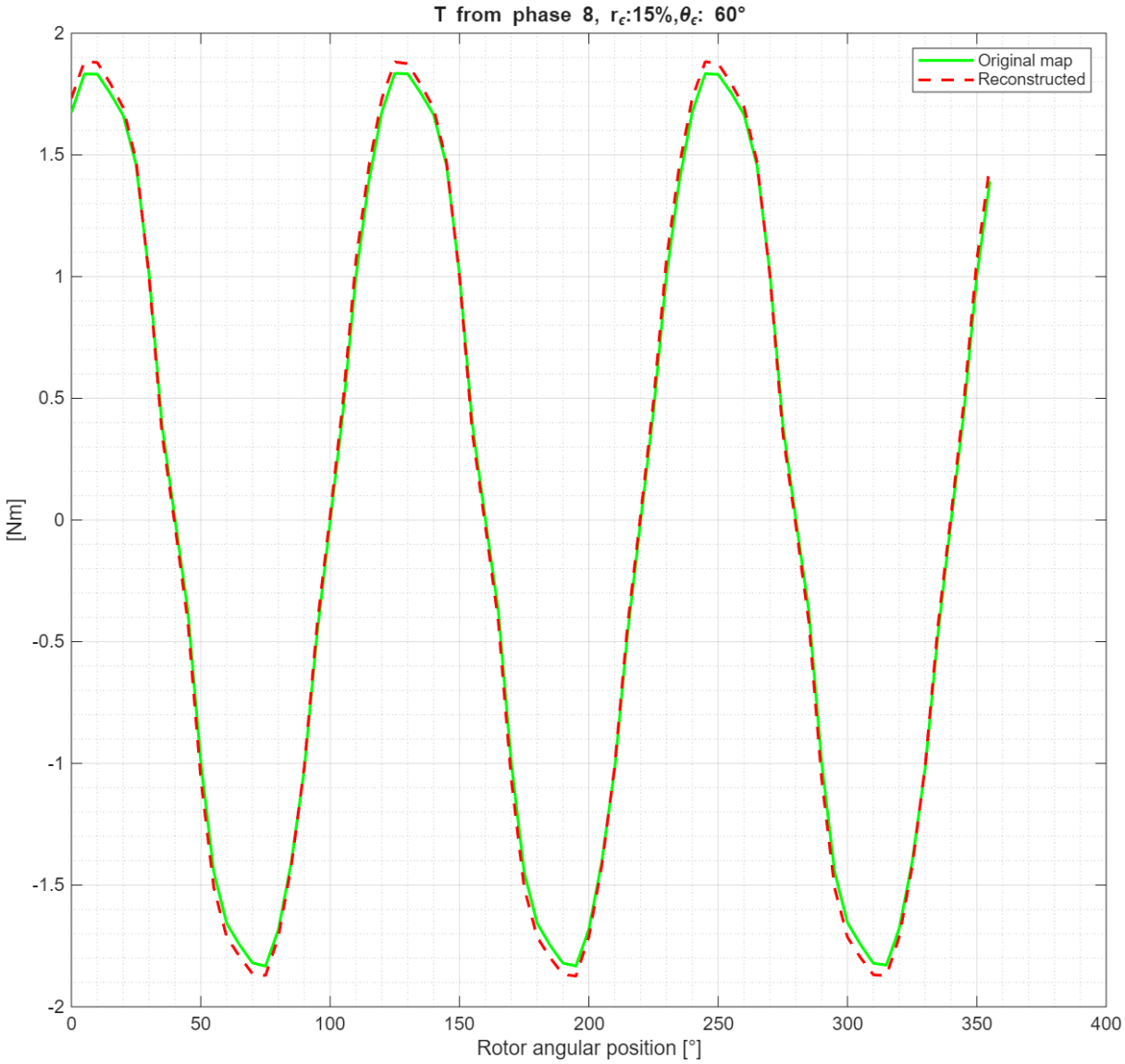

Figure 3.30: T from phase 8. Original vs reconstruction.

For the sake of completeness, a table with the errors regarding the reconstructed wrench W_R with respect to the original W is shown in 3.34. Since the periodic presence of zero-values in all the original waveforms, the error was computed with respect to the amplitude $|W_f|$ of the main harmonic of each wrench element, obtained from a FFT decomposition of the original samples, as:

$$\varepsilon_W = 100 \cdot \frac{W_R - W}{|W_f|} \tag{3.25}$$

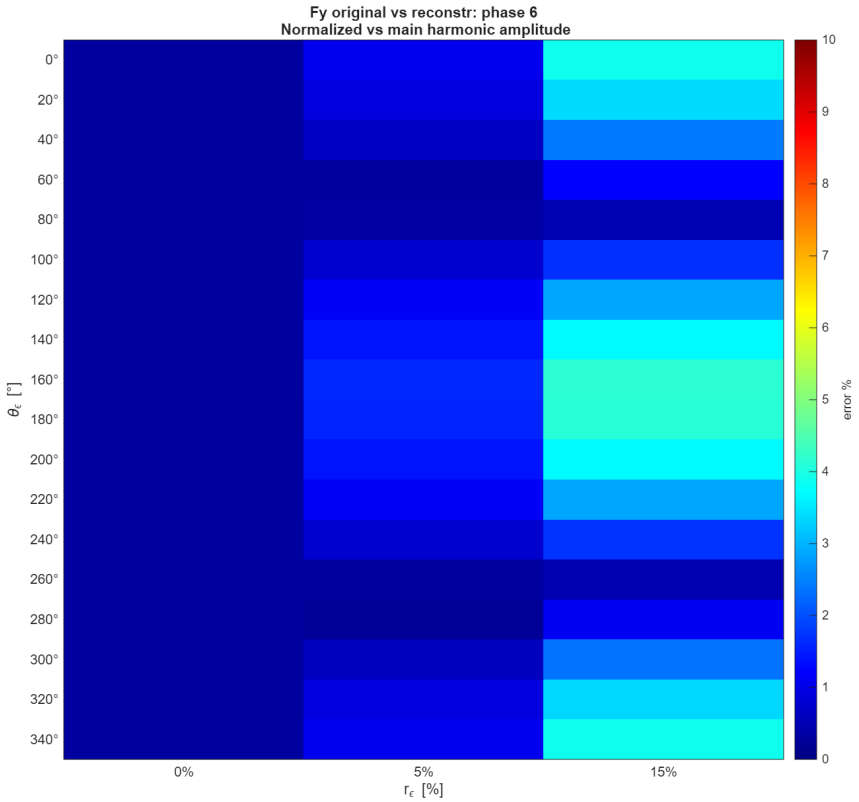

Figure 3.31: Error on reconstructed Fy_6 normalized with respect to the amplitude.

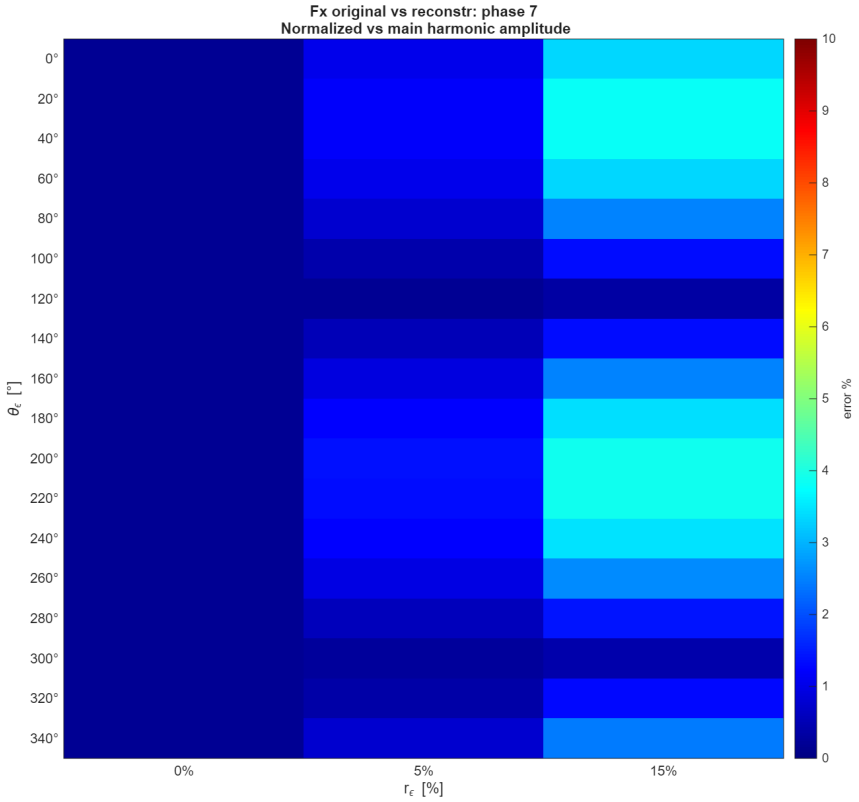

Figure 3.32: Error on reconstructed Fx_7 normalized with respect to the amplitude.

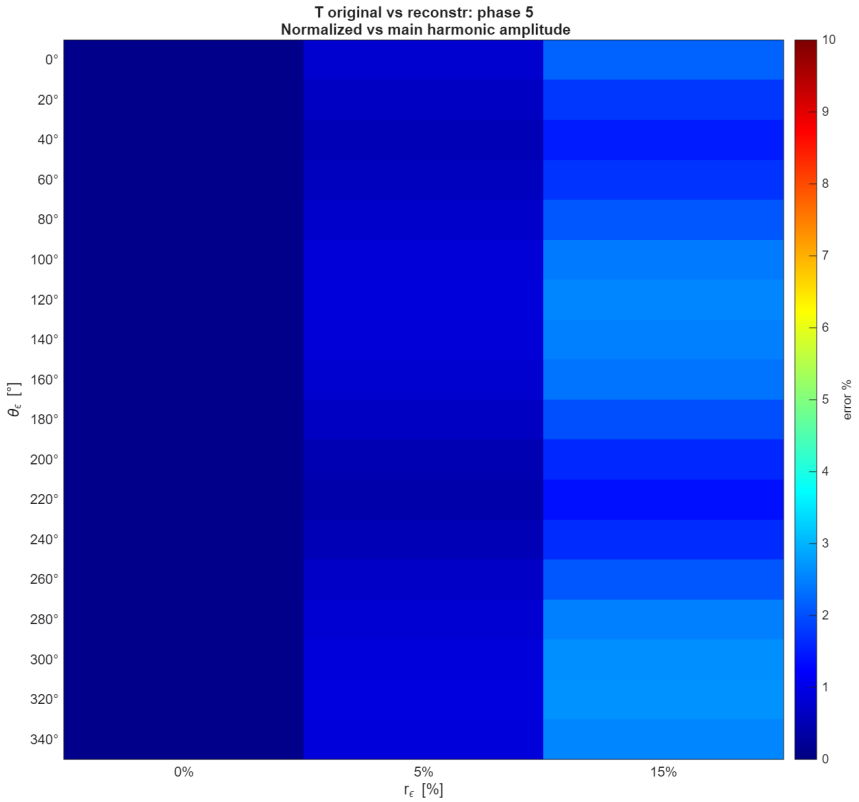

Figure 3.33: Error on reconstructed T_5 normalized with respect to the amplitude.

The normalized error is very well limited, with the only case of 15% eccentricity radius introducing errors consisting of a few percentage units. Figure 3.34 represents the errors obtained comparing original wrench of the machine with the one obtained with the roational matrix approach, highlighting a good average correspondence, even though few percentage units error appear due the difference in the obtained no-load wrench, which is unavoidably null, as can be seen in Fig. 3.30. Figure 3.34 shows the average errors, normalized with respect to the amplitude of the main harmonic, resulting from the adoption of the rotation technique described in [8]: trivially, the error for phases 1 to 3 is null, since those samples correspond to the originally mapped ones, and torque reconstruction results to be more precise, since it is less affected by eccentricity.

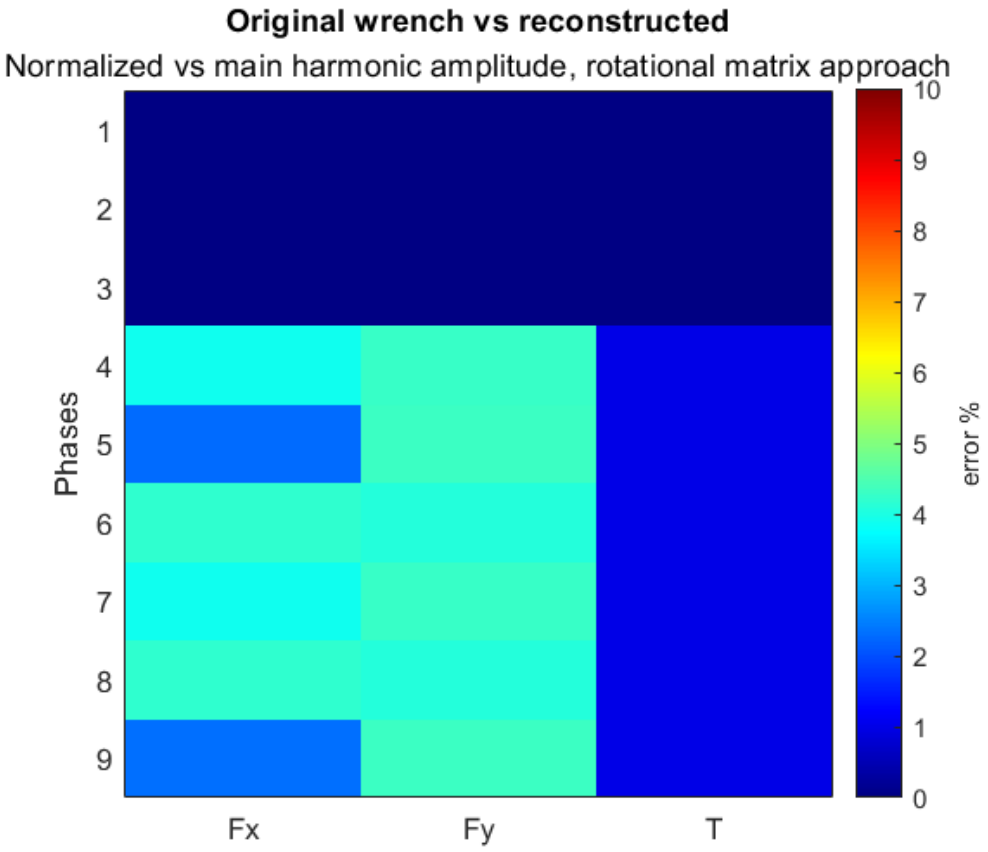

Figure 3.34: Average normalized errors for rotational matrix approach.

However, this was not the final optimization that this work achieved: the original phase set was reduced even further with respect to a single sector. Indeed, the machine simmetry, featuring symmetric axes for phases 2 and 3, allowed to avoid mapping phase 3, for which the wrench was obtained from the one resulting from phase 2. In the final part of this chapter, the strategy employed to complete the whole sector 1 wrench from two phases only, reducing the angular sample as well as did for the inductance matrix in Section 3.2.3, is described.

The most straightforward wrench element to indirectly map from one phase to another is the torque, as all phases produce the same identical torque when powered, with a phase shifting equal to the reciprocal angle between different phase axes. Negligible variations are caused by eccentricity, yet complying with the constraints for θ_ϵ described in 3.2.2 allows to ensure simulating the exact same relative rotor-stator positions again. Figure 3.35 highlights the described phenomenon with higher accuracy, proving that the correspondence is not that straightforward. In fact, it's sufficient to imagine the relative motion of the rotor magnets with respect to the phase 2 and 3 axes to understand that shifting by $\Delta\theta_{23} = 40°$ is not sufficient to cause the torque waveforms to match. To simulate the exact relative motion of magnets it's necessary to mirror the torque of phase 2, as if the rotor was rotating backwards, and then change also the sign, due to the inversion

of the reference frame: through this procedure, the torque for phase 3 is obtained from the one for phase 2 (Fig. 3.36).

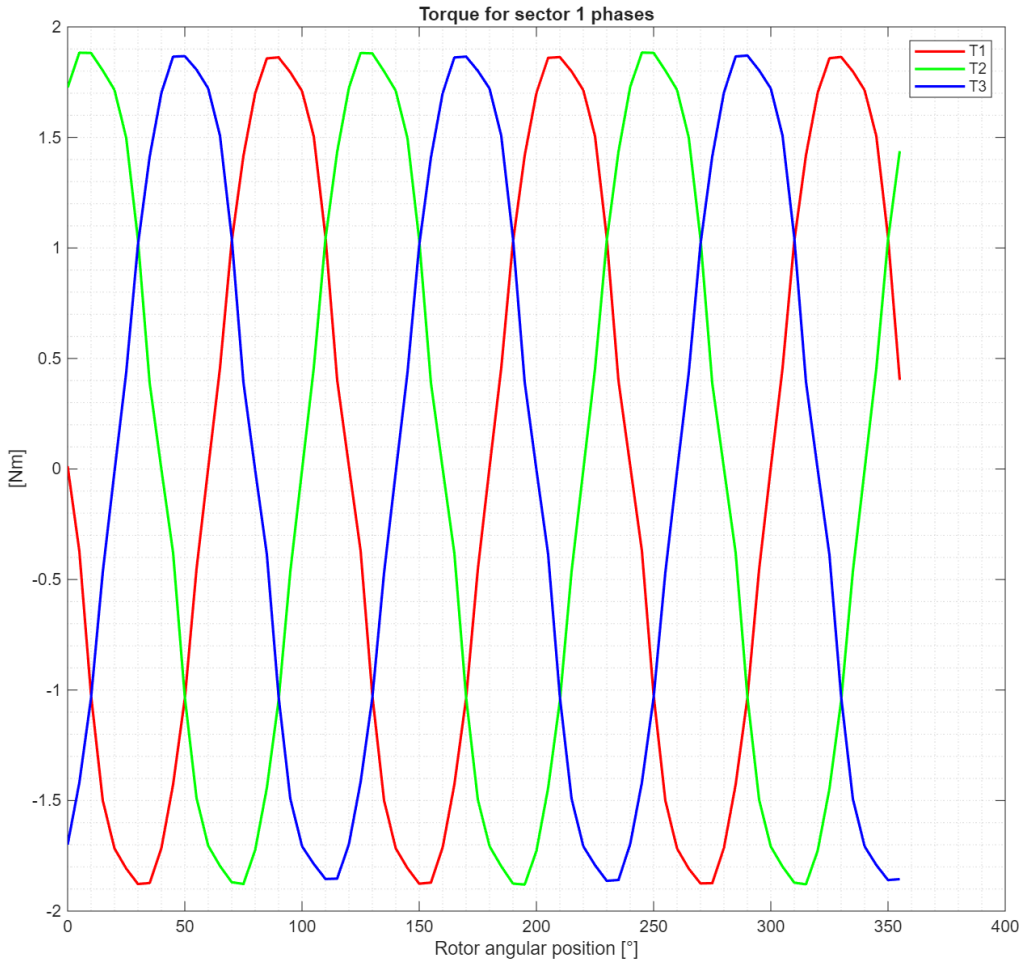

Figure 3.35: Torques while feeding sector 1 phases.

As will be shown in the next charts, the torque is easily obtained for the whole machine through shifts that simplify the explained procedure, exploiting the periodicity of data. A better match is obtained by considering only the phase currents contribution, without including in the procedure the cogging torque (Fig. 3.36), which is independent from the phase placement, and the same can be stated for radial forces.

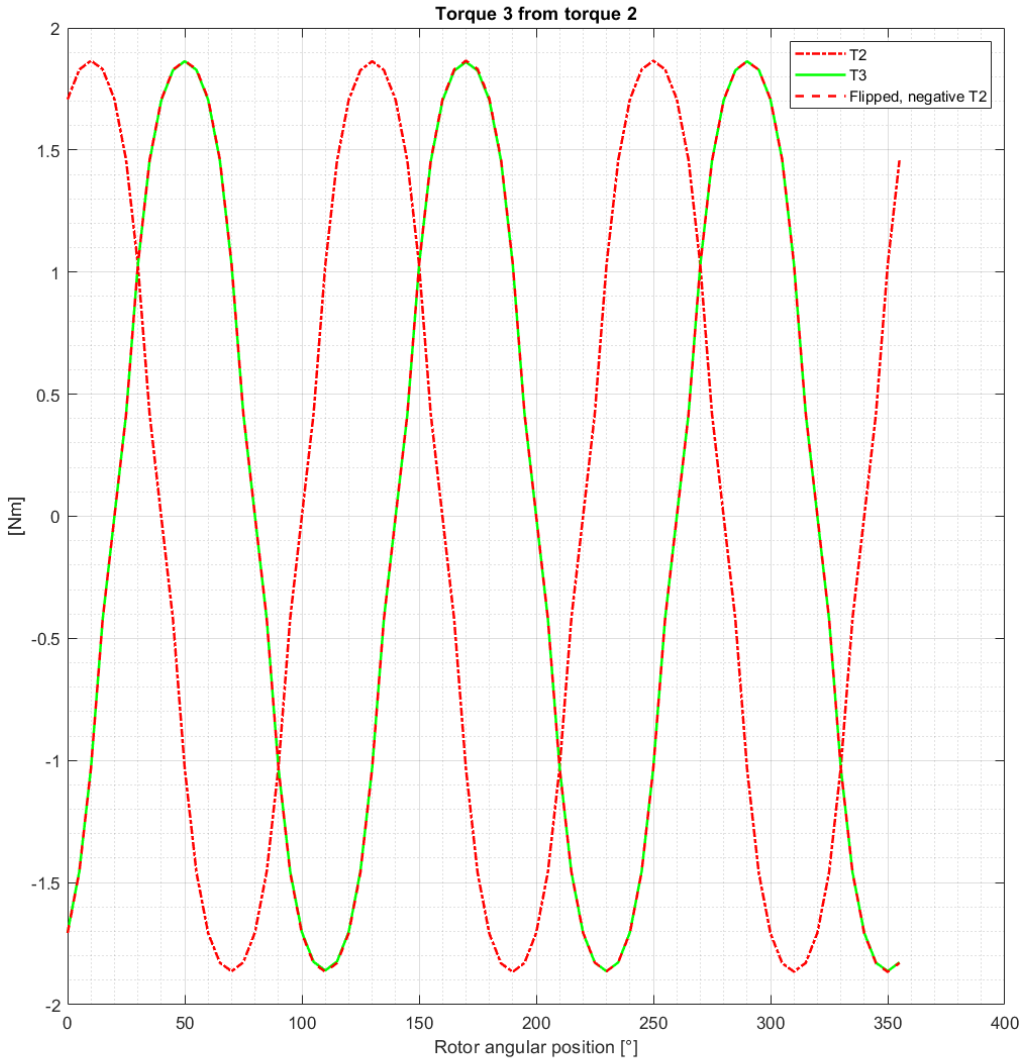

Figure 3.36: T3 obtained from T2.

The simmetry of phase 2 and 3 is easily exploitable to repeat the radial force developed on x direction: the same concept of counter-rotation used for torque turns to be effective for F_x, as shown in Figure 3.37.

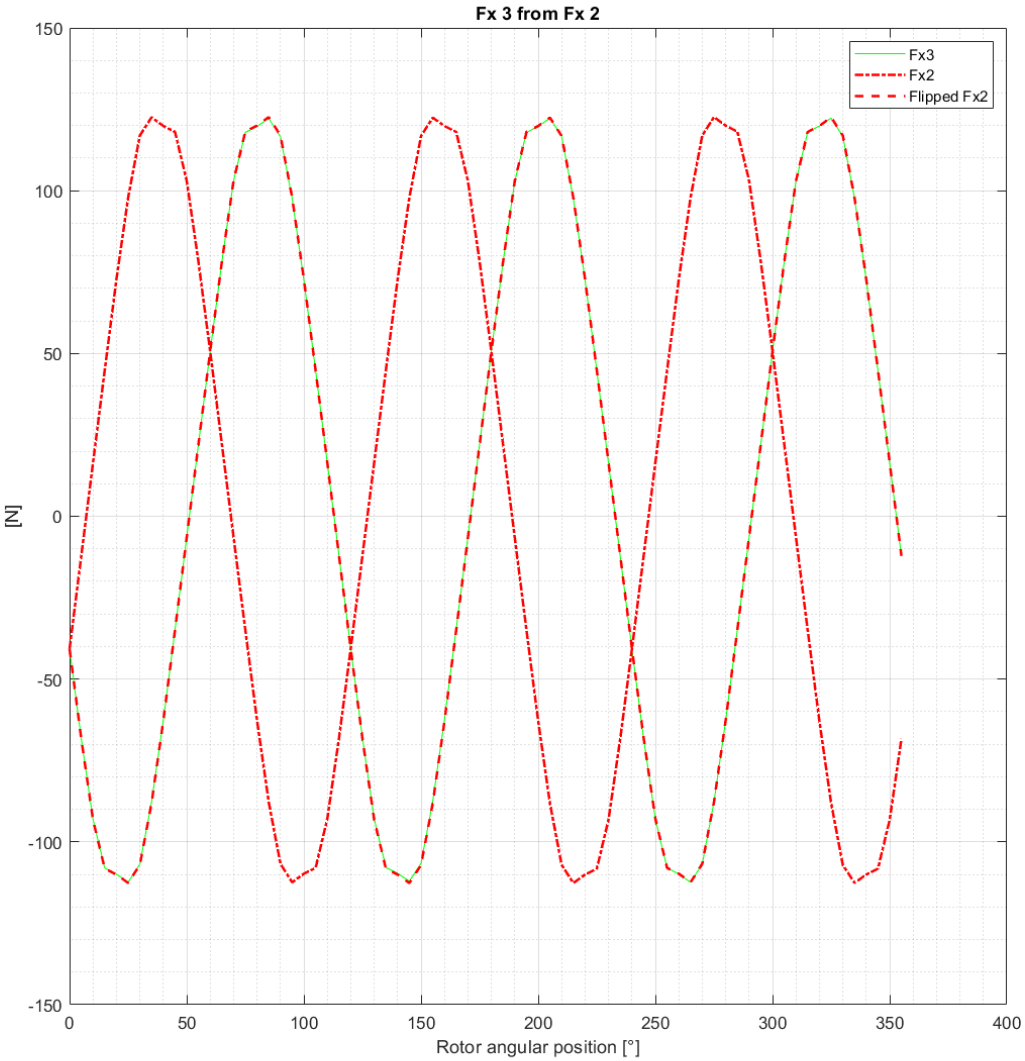

Figure 3.37: Fx3 from Fx2

Regarding Fy, the simmetry makes the sign inversion necessary to obtain a proper match, and Figure 3.38 shows that also rotor counter-rotation is needed.

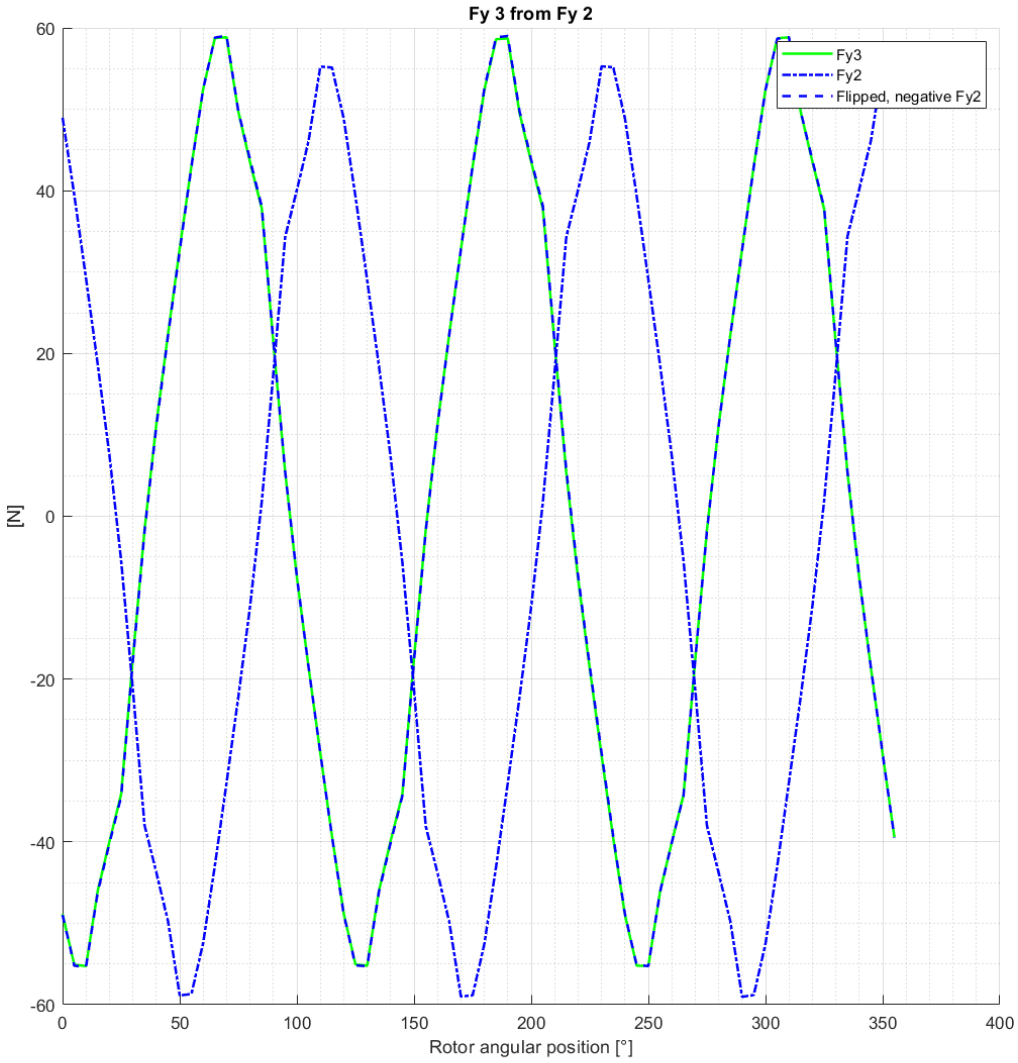

Figure 3.38: Fy3 from Fy2

Besides matching the wrench elements according to θ_m, also the eccentricity angles θ_ϵ are associated to the different reference axis, according to the shifts indicated in 3.14. Moreover, reducing the angular sample for θ_m is still possible: some iteration of a trial-and-error approach defined that the smallest sample possible consists of half an electrical period. In fact, due to the non-sinusoidal shape of the wrench waveforms, and the generation of important offsets in radial force in eccentricity conditions, at least 180 electrical degrees are needed, to fulfill the electrical period and repeat it twice to complete a 360° mechanical revolution. Indeed, from the initial sample W_{samp} of $\frac{\theta_{el}}{2} = 60°$, the second half of the electrical period is completed by repeating the original sequence after removing its offset OS to obtain a sinusoidal W_{sin}: this was useful for radial forces featuring non-negligible offset in some eccentricity configurations, while torque did not show important disturbances,

as shown in 2.12:

$$W_{sin} = W_{samp} - OS = W_{samp} - \frac{W_{samp}[1] + W_{samp}[end]}{2} \tag{3.26}$$

and finally exploit its symmetries, generalized as:

$$W_{T_{el}}[1 : T/2] = W_{samp} \qquad W_{T_{el}}[T/2 + 1 : end] = -W_{samp} \tag{3.27}$$

The final structure of the remapped general wrench element is obtained by concatenating the results obtained for an electrical period and adding the offset from 3.26 back:

$$W_{remap} = [W_{T_{el}}, W_{T_{el}}, W_{T_{el}}] + \frac{W_{samp}[1] + W_{samp}[end]}{2} \tag{3.28}$$

The results, being based on $\frac{T_{el}}{2}$ rather than $\frac{T_{el}}{4}$, appear to match independently from the initial sampling angle, allowing to identify a compact simulation set valid for both phases, without taking into consideration partial sets overlap, as did for phases 1 and 2 fluxes in Section 3.2.3. The comparison between the original and the remapped wrench elements is displayed in Figures 3.39, 3.40 and 3.41.

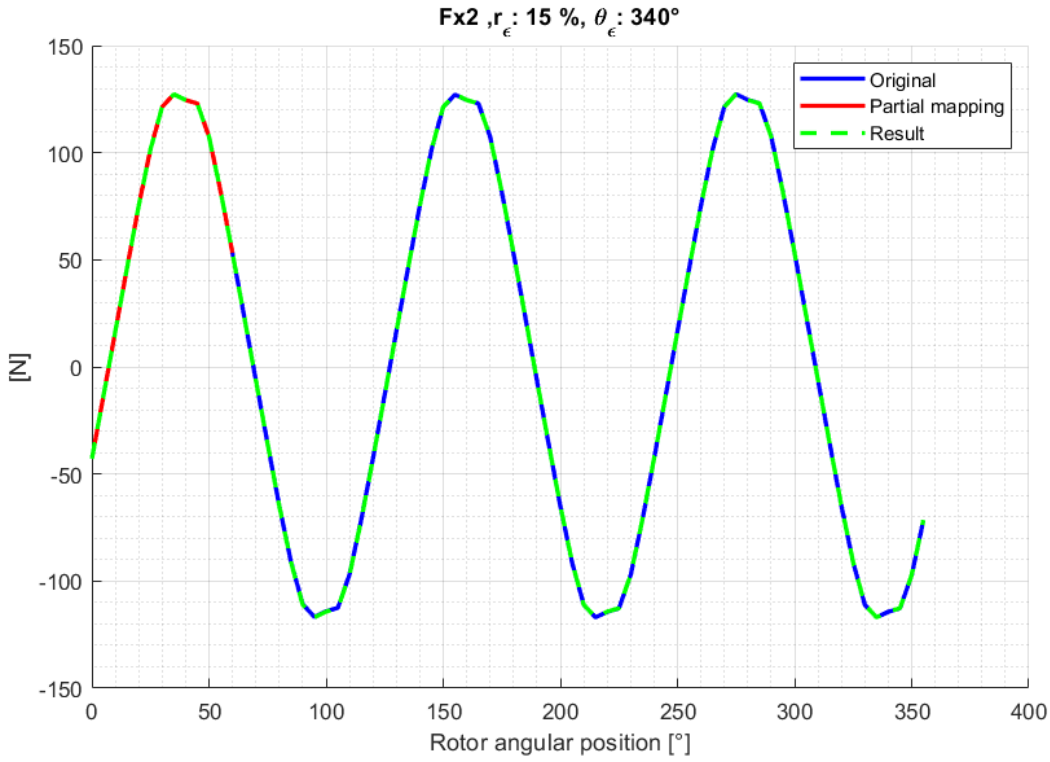

Figure 3.39: Remapped Fx from phase 2.

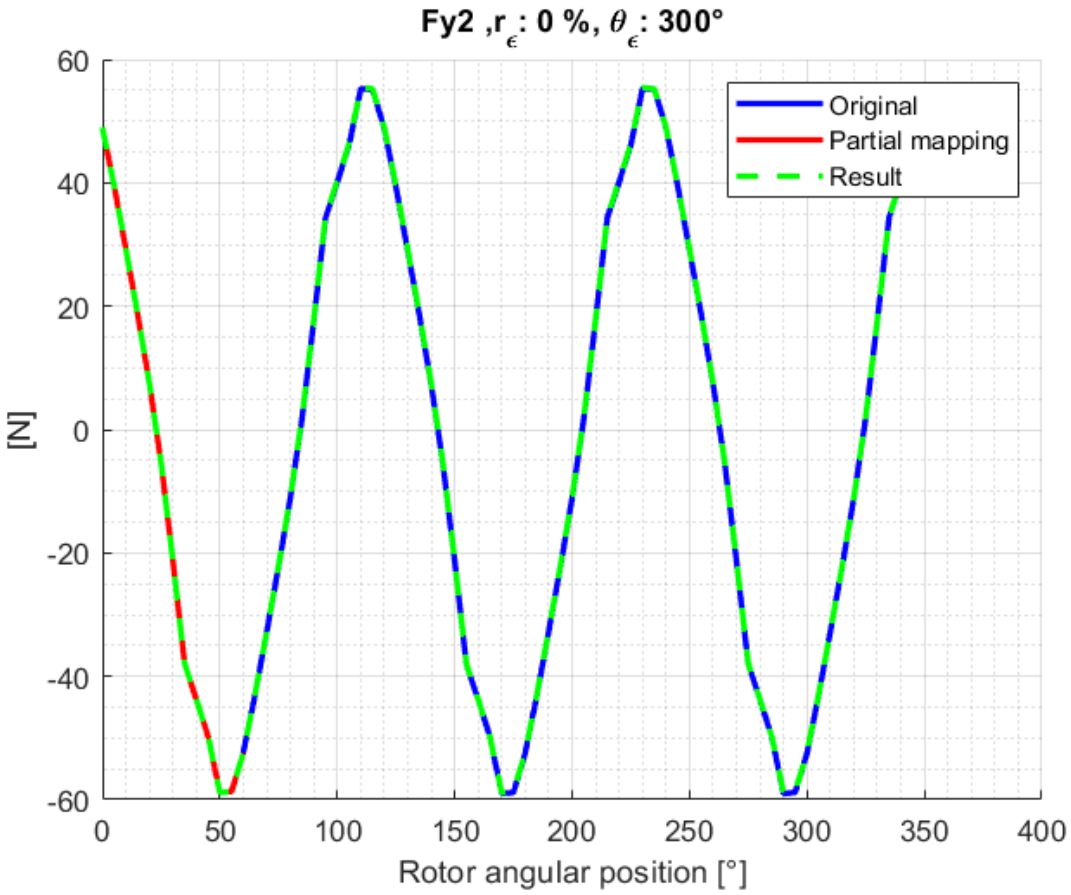

Figure 3.40: Remapped Fy from phase 2.

Figure 3.40 shows the effectiveness of the offset computation and application for a correct completion of the y-axis force component: the waveform features a clear mismatch between the absolute values of positive and negative peaks, which required compensation before proceeding. This was an essential step for a correct implementation of the fast mapping strategy, since the negative half-wave could not be obtained simply by mirroring the positive one without removing the mentioned offset.

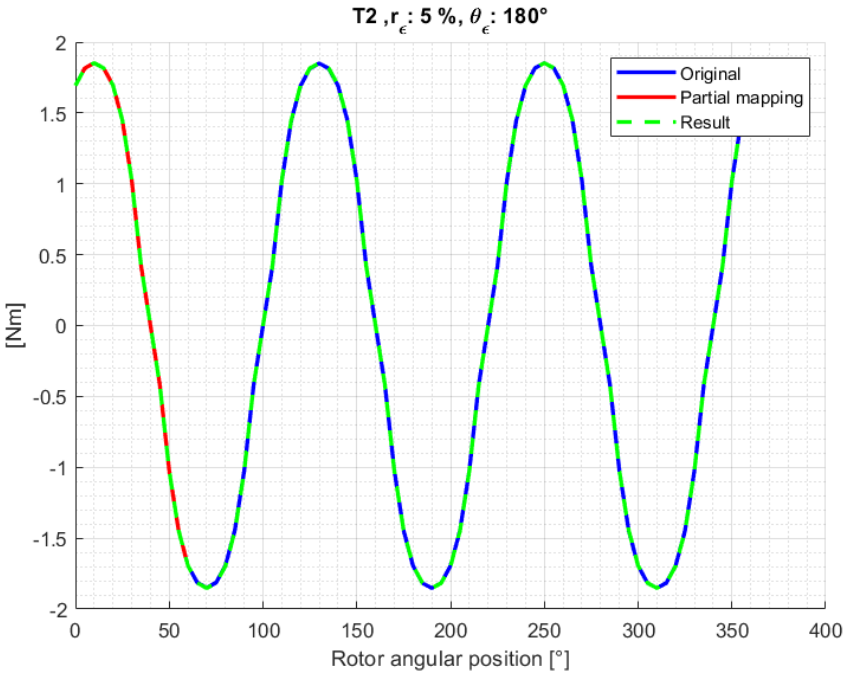

Figure 3.41: Remapped torque from phase 2.

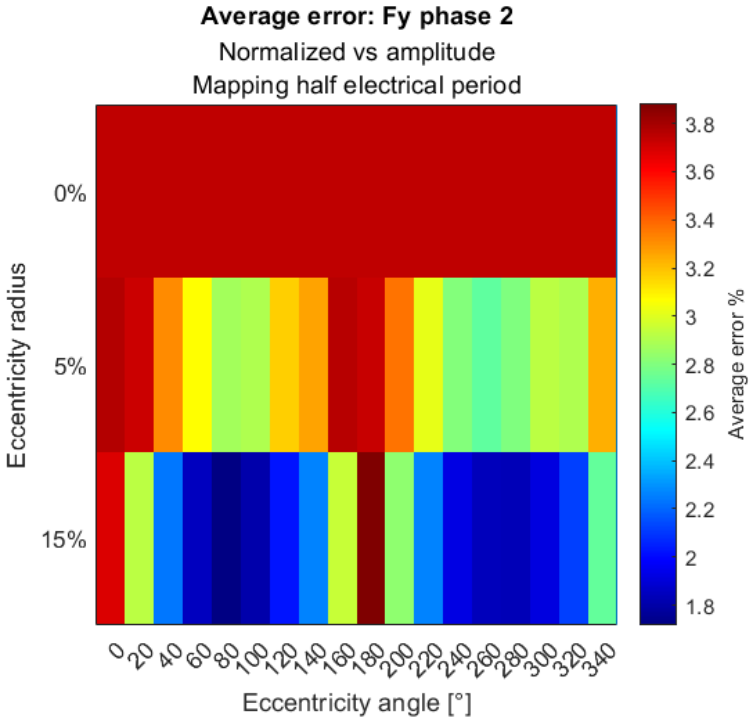

Figure 3.42: Errors from half-period mapping.

Due to the limited available sample $n\theta_m$, the no-load wrench is obtained by repeating the obtained sequence until completing the mechanical period, which leads to unavoidable error, described numerically in Figure 3.42 and graphically in Figure 3.43.

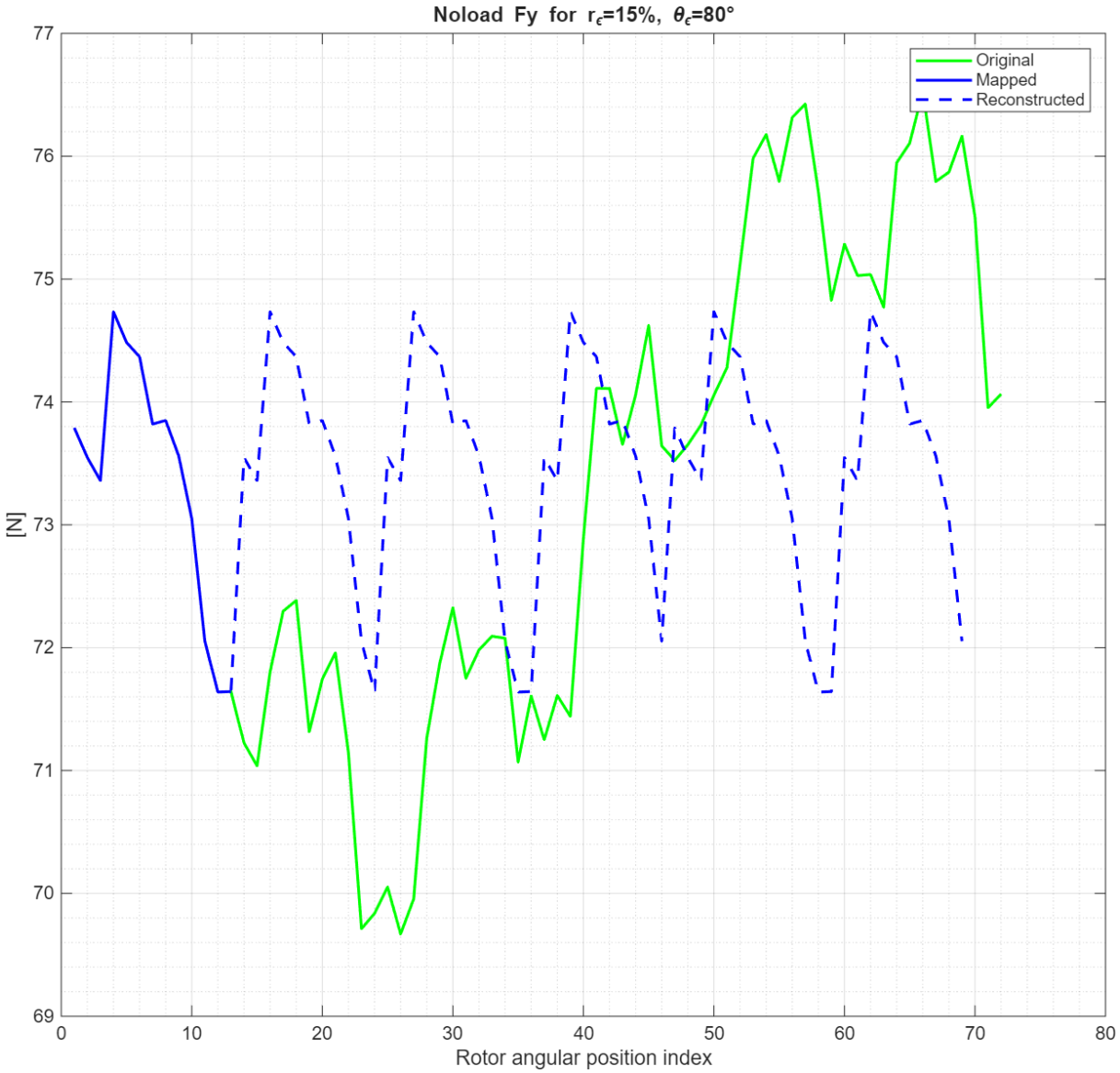

Figure 3.43: Original and reconstructed no-load Fy for reduced $n\theta_m$.

To mitigate this effect, hence improving accuracy with a very small increase in computational duty, a reasonable approach consists of mapping the no-load wrench over the whole 360° in centered conditions, in order to compute the numeric error that leads to non-zero radial forces and using the results to correct the wrench in eccentricity condition, obtaining a better match. The no-load sample is also used to correct the eccentric results, as the trend of the two waveforms is exactly the same as in Figure 3.2, also numerically.

Starting from the first $n\theta_m$ =13 samples of the radial forces obtained from the no-load centered mapping, it is possible to remove the numerical error arising from the fact that, in the centered no-load condition, the radial forces should be zero but are not (Fig. 3.2). By subtracting the first $n\theta_m$ =13 centered-rotor values from the corresponding eccentric ones, is possible to compensate for such offset, which is most likely caused by meshing inaccuracies in the finite-element model.

If these 13 corrected samples are then concatenated over the entire mechanical period, the resulting waveform represents with a good approximation the eccentric radial forces without the error present in the centered case, thus giving a result with greater physical meaning.

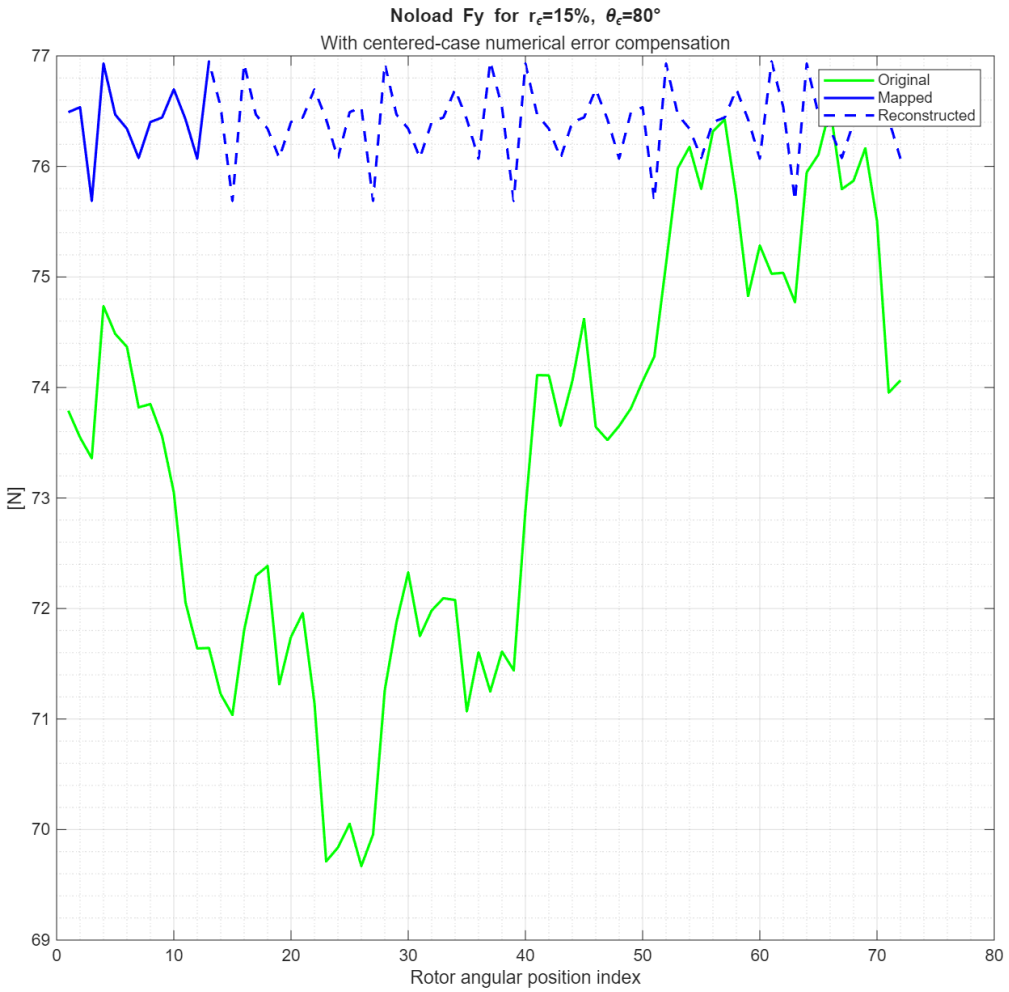

Figure 3.44: Resulting eccentric no-load Fx from optimized mapping, with centered-error compensation.

To match the original simulations results, instead, it's possible to add again the centered contribution to the obtained result, improving the accuracy of the model, while performing only few extra iterations. This strategy was not applied to the torque samples, since those don't exhibit high correlation with eccentricity and the relative errors were already close to zero.

Figure 3.45: Resulting eccentric no-load Fx from optimized mapping.

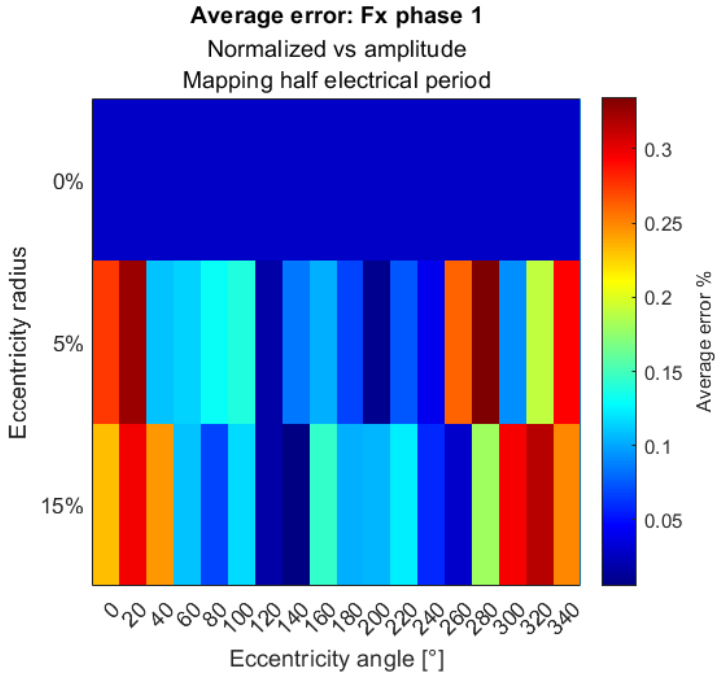

Figure 3.46: Eccentricity no-load compensation results on Fx errors.

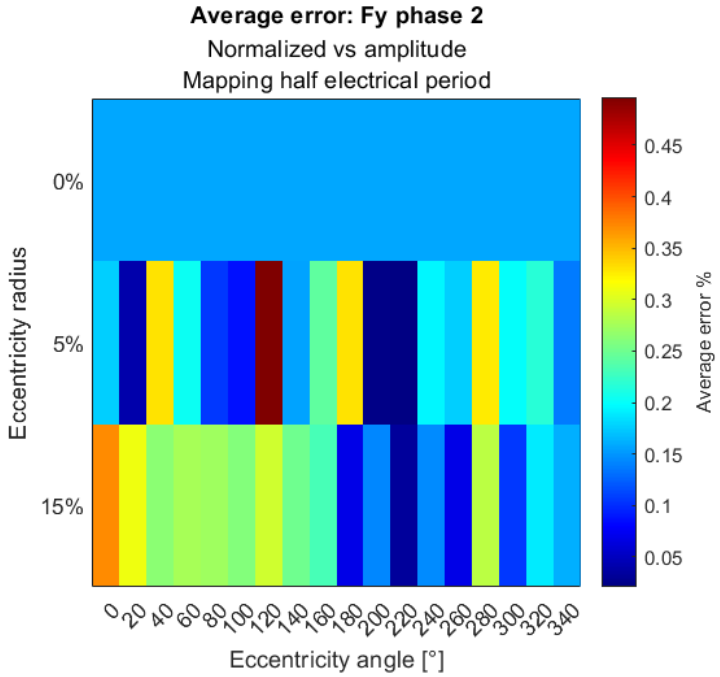

Figure 3.47: Eccentricity no-load compensation improvement on Fy errors.

The resulting error tables prove the effectiveness of this final strategy in error reduction: Figures 3.46 and 3.47 show sensible improvement in the resulting error, particularly the latter if compared with 3.42.
After clarifying the optimization strategies and highlighting their accuracy, the final part of this analysis deals with the savings in term of iterations and hence computational effort.

Chapter 4

Results

Applying all the strategies for computational effort reduction discussed in Chapter 3, it was possible to compute both the inductance matrix and the wrench vector by mapping two phases only, simulating a fraction of an electrical period, maximizing the computational efficiency of the mapping procedure. This chapter summarizes the implemented strategies and provides results in terms of accuracy, reduction of computational effort and computational time, while the accuracy analysis was already addressed in Chapter 3.
As a first step, some low-complexity simplifications were introduced in the mapping procedure, such as model mesh reduction from 140k nodes to 33k, performing no-load simulations for one phase only, avoiding repetitive simulations for $r_\epsilon = 0\%$: this allowed to reduce the number of iterations (Eq. 2.21, 3.6) from

$$N_{sim} = n\theta_m \cdot n\gamma_I \cdot nr_\epsilon \cdot n\theta_\epsilon \cdot n_{ph} = 36 \cdot 3 \cdot 3 \cdot 6 \cdot 9 = 17496$$

to

$$N_{sim,opt1} = n\theta_m \cdot [(1 + (nr_\epsilon - 1) \cdot n\theta_\epsilon) \cdot (1 + n_{ph})] = 9360$$

resulting in a reduction of $1 - \frac{9360}{17496} = 46.5\%$, even though the sample width for θ_m had been doubled ($n\theta_m = 72$, while originally was 36). Applying more extreme optimization strategies evidenced that reducing the number of powered phases n_{ph} from 9 to 2, according to the results of Sections 3.2.1 and 3.2.2, was possible provided that specific constraints on the simulated angles were introduced, setting the minimum values of $n\theta_m$ and $n\theta_\epsilon$ as 72 and 18 respectively. Considering all the combinations of the sensitive variables [n_{ph}, γ_I, r_ϵ, θ_ϵ], the number of iterations can be computed recalling 3.1 as

$$N_{sim,opt2} = n\theta_m \cdot [(1 + (nr_\epsilon - 1) \cdot n\theta_\epsilon) \cdot (1 + n_{ph})] = 72 \cdot [(1 + 2 \cdot 18) \cdot (1 + 2)] = 7792 \quad (4.1)$$

Even though a low reduction in the computational effort was expected, since the number of phases was reduced to $\frac{2}{9} = 22\%$, but the size of the sample of θ_ϵ was triplicated to $n\theta_\epsilon = 18$, the reduction of the powered phases during the simulations was justified by a

reduction of $1 - \frac{7792}{17496} = 55.46\%$, hence an extra 9% with respect to the previous step.
The reduction of $n\theta_m$ to fractions of an electrical period was investigated in 3.2.3, opening to the possibility of mapping the wrench vector by $\theta_m = \frac{T_{el}}{2} = 60°$, corresponding to $n\theta_m = 13$, as 13 samples are used to cover an angular span of 60° with a step size of 5°, including both the initial and the final samples to ensure higher accuracy. For this reason, the generalized formula from Eq. 3.1 can be applied to obtain the number of simulations for wrench:

$$N_{sim,opt3} = n\theta_m \cdot [(1 + (nr_\epsilon - 1) \cdot n\theta_\epsilon) \cdot (1 + n_{ph})] = 13 \cdot [(1 + 2 \cdot 18) \cdot (1 + 2)] = 1443 \quad (4.2)$$

resulting in a reduction of $1 - \frac{1443}{17496} = 91.75\%$, hence a flabbergasting extra 45% with respect to the previous step. Even though in the referenced section 3.2.3 has been claimed that for inductance computation the sample size for θ_m was halved, hence $n\theta_m$=7, corresponding to 30° only, the *PostProcessing.m* function had to be executed for the wrench samples as well, and for this reason the value of $n\theta_m$ was assumed equal to 13.

The final reduction of computational demand was implemented by deploying two different FEMM models for the simulations of inductance and wrench, to mitigate the effects of the main limit of the previous approach.
For the inductance matrix, a new FEMM model was created to approximate perfect rotor isotropy by removing the rotor magnets and modifying the airgap material property (Section 3.2.3): this key model variation allowed for the first time in this work to modify the sample size of θ_m, drastically reduced from $n\theta_m = 72$ to $n\theta_m = 1$; also, the no-load simulation was not necessary anymore to remove the magnets' flux contribution, those not being present in the model anymore.

Due to the absence of the no-load simulation, Eq. 3.1 is not valid for this case. The number of iterations for the computation of the inductance matrix is reduced to:

$$\begin{aligned} N_{sim,L} &= N_{sim}(r_\epsilon \neq 0\%) + N_{sim}(r_\epsilon = 0\%) \\ &= n_{ph} \cdot (nr_\epsilon - 1) \cdot n_{\theta_\epsilon} + n_{ph} \\ &= 2 \cdot 2 \cdot 18 + 2 = 74 \end{aligned} \quad (4.3)$$

Regarding the wrench, instead, the generalized formula from Eq. 3.1 can be applied to obtain the number of simulations for the wrench:

$$N_{sim,W} = n\theta_m \cdot [(1 + (nr_\epsilon - 1) \cdot n\theta_\epsilon) \cdot (1 + n_{ph})] = 13 \cdot [(1 + 2 \cdot 18) \cdot (1 + 2)] = 1443 \quad (4.4)$$

For a total number of simulations equal to:

$$N_{sim,opt4} = N_{sim,W} + N_{sim,L} = 1443 + 74 = 1517 \quad (4.5)$$

Even though such a number is higher than the one obtained for 4.2, the main difference relies in the nature of those simulations: while in the previous version both the operations were executed serially for all the 1443 iteration, in this scenario the actions are decoupled into the functions $PostProcessing\_Wrench$ and $PostProcessing\_Flux$, hence with approximately half the numerical operations to be performed with respect to the previous case. Flux linkage computation, that consists of selecting singularly each one of the 18 slots to integrate the magnetic vector potential across their surface, is performed only 74 times (Eq. 4.3); for the other 1443 simulations (Eq. 4.4), the software only has to select the rotor and compute the wrench through the MST as in Section 2.1.

The final proposed strategy consists of a tradeoff between computational duty reduction and accuracy improvement: by mapping the no-load wrench over the whole 360° in centered conditions only, it is possible to compensate for the numeric error leading to non-zero radial forces in centered no-load conditions, as well as giving the possibility to increase the physical significance of the results if desired.

This only comes at the cost of simulating the complete rotor revolution in centered case ($n\theta_m = 72, n_{ph} = 1, nr_\epsilon = 1, n\theta_\epsilon = 1$), considering that 13 of those iterations were already included in Eq. 4.4, resulting in

$$N_{sim,Wextra} = 72 - 13 = 59 \tag{4.6}$$

extra iterations with respect to Eq. 4.5. The total number of iterations for the final optimized model are, then:

$$N_{sim,opt4} = N_{sim,W} + N_{sim,L} + N_{sim,Wextra} = 1443 + 74 + 59 = 1576 \tag{4.7}$$

The number of iterations required for a perfectly accurate mapping can then be generalized as:

$$N_{sim,opt5} = N_{sim,L} + N_{sim,W} + N_{sim,Wextra} \tag{4.8}$$

$$= [n_{ph} \cdot (nr_\epsilon - 1) \cdot n_{\theta_\epsilon} + n_{ph}] \tag{4.9}$$

$$+ n\theta_m \cdot [(1 + (nr_\epsilon - 1) \cdot n\theta_\epsilon) \cdot (1 + n_{ph})] \tag{4.10}$$

$$+ [n\theta_m - (\frac{n\theta_m}{frac_m} + 1)] \tag{4.11}$$

where $frac_m$ represents the fraction of mechanical period being mapped, in this case 6, being half of an electrical period, and $n\theta_m$ represents the number of steps to map a full mechanical period, in this case 72. With respect to the original amount of simulations,

this result corresponds to a computational effort of

$$\frac{1576}{17496} = 9\% \tag{4.12}$$

In order to provide a broader perspective of the real computational effort reduction, the simulation elapsed time is included in the analysis. Indeed, as discussed in Section 3.1, it was assumed that the adoption of a new FEMM model featuring a looser mesh with respect to the original, allowed saving 86.2% of the execution time of the simulation (Eq. 3.1), and that the adoption of two different MATLAB functions for the computation resulted in an extra reduction by 22% of the required elaboration time.
In case improving the simulation resolution is the aim of the optimization instead, this approach can also be exploited for such a purpose: the obtained computational reduction allows thickening the simulation set without introducing concerns about the simulation time of the mapping process.
Besides the reduction of the computational duty of the simulation, it is important to remember that the function of the mapping procedure is to provide a solid basis for control algorithms. As a final step, a new structure is created to store all possible results from combinations of nine phase currents, rotor position and eccentricity. This structure is used to provide Simulink control models of a look-up table (LUT), which parameterizes the motor's behaviour in real time with satisfactory precision. The LUT can finally be added to the Simulink model: only requiring the nine phase currents, the rotor angular and planar position $(x - y)$, the output of the block includes the 9x9 inductance matrix and the "instantaneous" values of the wrench vector $W = [F_x; F_y; T]^T$. An insight on the applications of the results is provided in Chapter 5.

Chapter 5

Results use in control system

In this section, the role of the LUT generated by the machine mapping is investigated: indeed, the results of this work have been used in research work regarding the sensorless control of the motor position, by means of an Extended Kalman filter. A complete description of the control architecture and its implementation is provided, focusing mostly on the details derived from the previously introduced work. It's important to highlight that the model features a small-sized map, featuring only 36 points for θ_m, which do not allow to correctly simulate the skewing of the rotor; since it was not the main interest of the research project, this did not affect the validity of the results. The look-up table (LUT) is mostly used in the machine block, which is recognizable from its mask representing the cross section of the multi-sector bearingless machine, more clearly visible in 5.4.

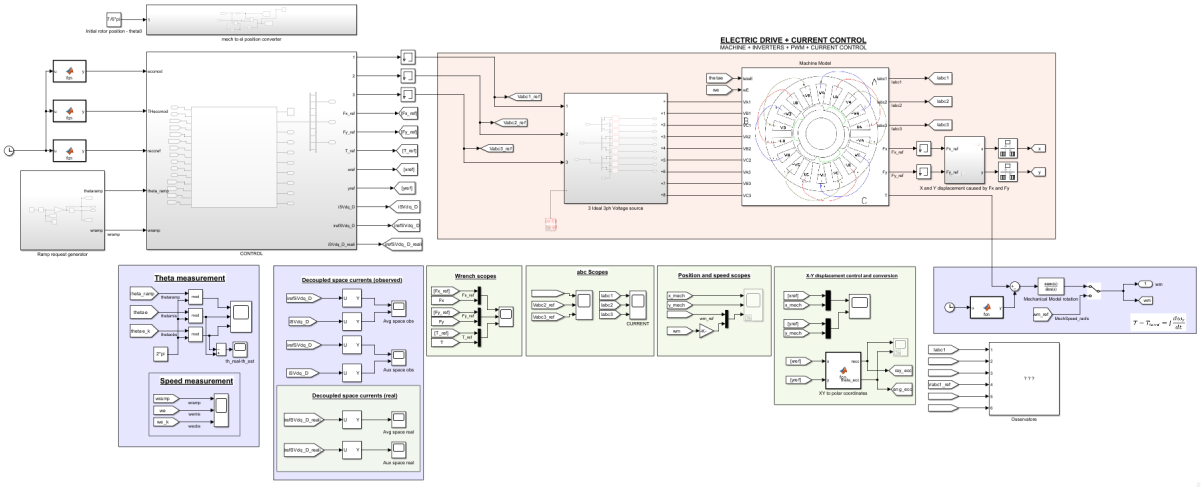

Figure 5.1: Sensorless control Simulink model.

The control scheme adopts a PI controller for the speed loop, whose dynamics are naturally stable due to the presence of a viscous friction term proportional to the rotor velocity, which introduces negative real poles in the system, and a PID controller for the force–generation dynamics, that for a bearingless actuator are inherently unstable. Indeed, for an electromagnetic actuator, the closer the ferromagnetic target moves to the stator

core, the stronger the attractive force becomes. When the rotor is centered with the stator axis, the airgap flux density is constant. Instead, if some eccentricity is introduced, the air gap permeance becomes a function of θ, recalling Figure 1.3:

$$\lambda(\theta) = \frac{\mu_0}{g_0[1 - r_\epsilon \, cos(\theta - \theta_\epsilon)]} \tag{5.1}$$

where r_ϵ is the eccentricity radius ρ normalized relatively to the air gap thickness g_0, and θ_ϵ is the eccentricity angle. This unbalance in permeance causes the arising of radial forces acting on the rotor. It's possible to compute them by solving equations 2.11 and 2.12 assuming that the eccentricity is small enough not to affect the current, so that the PM radial flux $B_{r,PM}$ is still dominant with respect to its tangential component $B_{n,PM}$.

$$F_x \approx \int_0^{2\pi} Lr \, \frac{B_{r,PM}^2}{2\mu_0} \, cos\theta \, d\theta = k_m \, \varepsilon \, cos\theta_e \tag{5.2}$$

$$F_y \approx \int_0^{2\pi} Lr \, \frac{B_{r,PM}^2}{2\mu_0} \, cos\theta \, d\theta = k_m \, \varepsilon \, sin\theta_e \tag{5.3}$$

Where k_m is a coefficient representing the suspension force stiffness of rotor eccentricity: the most interesting feature of this parameter is that (at least for low eccentricities) the generated force aims towards the eccentricity direction θ_e, and is proportional to the eccentricity radius r_ϵ: this means that the radial force given by the magnets tends to increase the eccentricity by pushing the rotor even further away from the geometrical center. This phenomenon is called negative stiffness, to highlight the fact that the system does not aim to restore the initial configuration, as expected from a stiffness component, but it instead tends to strengthen the perturbation. Because of this, the unbalanced magnetic pull (UMP) is considered to be a self-sustaining event phenomenon. Linearizing the governing equations around the operating point and computing the closed-loop poles yields one negative pole and one positive pole, confirming the intrinsic open-loop instability of the system. Consequently, achieving closed-loop stability requires not only proportional–integral action but also a derivative term, due to the mechanical nature of the magnetic suspension force and the absence of natural damping. The PID controller is tuned using the inductances from the LUTs, and allows to obtain the reference radial force values.

The control block, the grey one to the left in Figure 5.1, is presented in detail in Figure 5.2: it receives as inputs the requested speed and rotor angle, the estimations by the observer, the requested eccentricity ($x - y$ coordinates) and the nine currents, and delivers the reference wrench elements and xy positions.

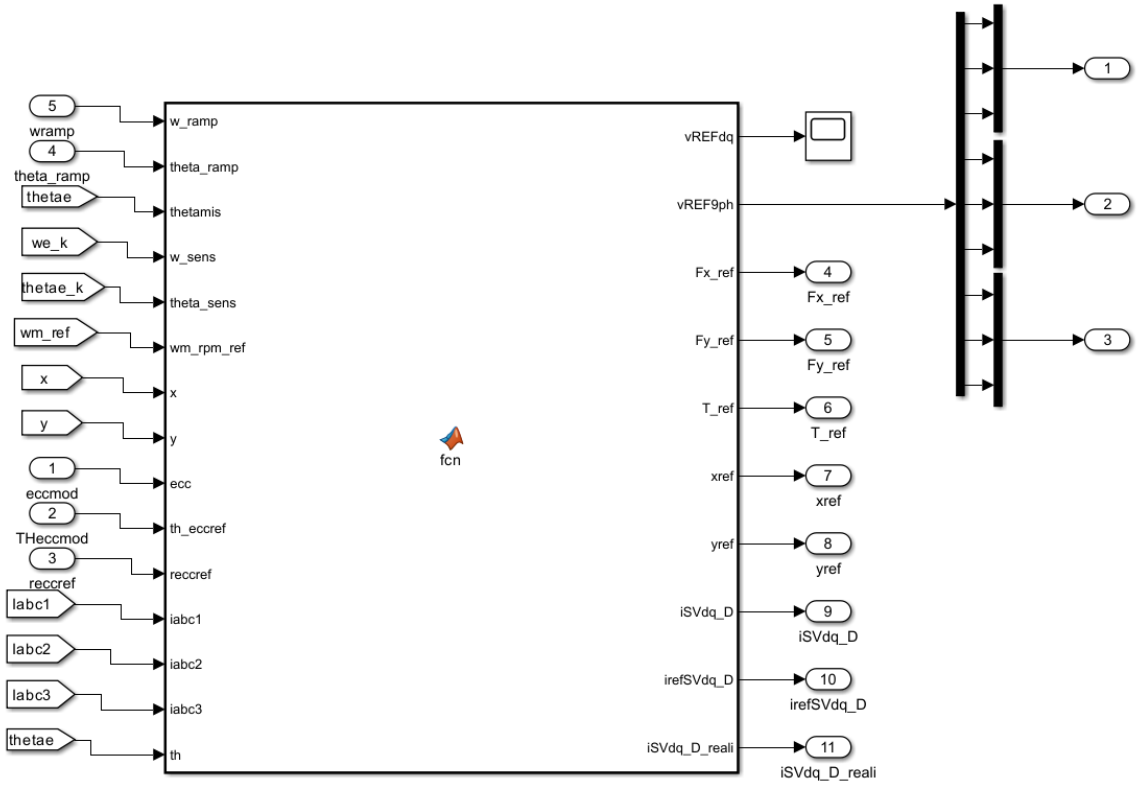

Figure 5.2: Control block

To obtain the phase currents needed to meet the radial force reference, the Pseudoinverse matrix (PIM) is used, as it allows to create a direct link between the wrench vector and the $i_{\alpha\beta}$ current of each sector in the Clarke reference frame. For a single vector, it is representable as a matrix ${}^{s}\overline{\mathbf{K}}_E$, function of the electrical angle θ_e and the phase currents ${}^{s}\gamma$:

$$ {}^{s}\overline{W}_E(\vartheta_e, {}^{s}\gamma, {}^{s}\bar{i}_{\alpha\beta}) = {}^{s}\overline{\mathbf{K}}_E(\vartheta_e, {}^{s}\gamma)\,{}^{s}\bar{i}_{\alpha\beta} \tag{5.4} $$

Where

$$ {}^{s}\overline{\mathbf{K}}_E(\vartheta_s, {}^{s}\gamma) = \begin{bmatrix} {}^{s}k_{x,\alpha}(\vartheta_e, {}^{s}\gamma) & {}^{s}k_{x,\beta}(\vartheta_e, {}^{s}\gamma) \\ {}^{s}k_{y,\alpha}(\vartheta_e, {}^{s}\gamma) & {}^{s}k_{y,\beta}(\vartheta_e, {}^{s}\gamma) \\ {}^{s}k_{T,\alpha}(\vartheta_e) & {}^{s}k_{T,\beta}(\vartheta_e) \end{bmatrix}. \tag{5.5} $$

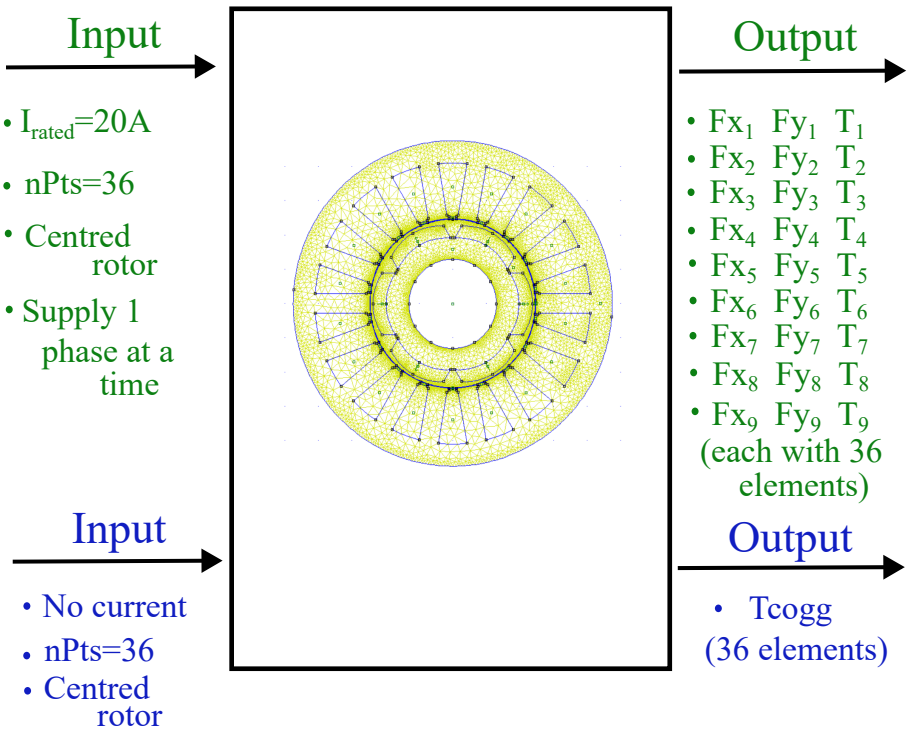

Figure 5.3: LUT in Simulink control scheme.

The harmonic components of the Pseudoinverse matrix for the whole machine are computed through the mapped wrench, resulting into:

$$\text{Kpinv} = \begin{bmatrix} K_{pF_{x1}} & K_{pF_{y1}} & K_{pT1} \\ K_{pF_{x2}} & K_{pF_{y2}} & K_{pT2} \\ K_{pF_{x3}} & K_{pF_{y3}} & K_{pT3} \\ K_{pF_{x4}} & K_{pF_{y4}} & K_{pT4} \\ K_{pF_{x5}} & K_{pF_{y5}} & K_{pT5} \\ K_{pF_{x6}} & K_{pF_{y6}} & K_{pT6} \\ K_{pF_{x7}} & K_{pF_{y7}} & K_{pT7} \\ K_{pF_{x8}} & K_{pF_{y8}} & K_{pT8} \\ K_{pF_{x9}} & K_{pF_{y9}} & K_{pT9} \end{bmatrix} \tag{5.6}$$

This means that to calculate the required nine *abc* phase currents the matrix operation is:

$$i_{abc,ref} = \text{Kpinv} \cdot W_{ref} \tag{5.7}$$

Where W_{ref} is the reference wrench vector, defined as:

$$W_{ref} = \begin{bmatrix} F_{x,ref} \\ F_{y,ref} \\ T_{ref} \end{bmatrix} \tag{5.8}$$

Once defined the required nine currents, a PI regulator sets the reference voltage requests, to be generated by three ideal three-phase inverters block, feeding the machine model shown in Figure 5.4. This block includes an RL load and a back-EMF calculation stage, that makes use of the no-load fluxes ϕ_{PM} provided by the LUTs obtained by the mapping procedure.

$$e = \frac{d\phi_{PM}}{dt} = \frac{d\phi_{PM}}{d\vartheta_{el}} \frac{d\vartheta_{el}}{dt} = \frac{d\phi_{PM}}{d\vartheta_{el}} \omega_{el} = K_e \omega_{el} \tag{5.9}$$

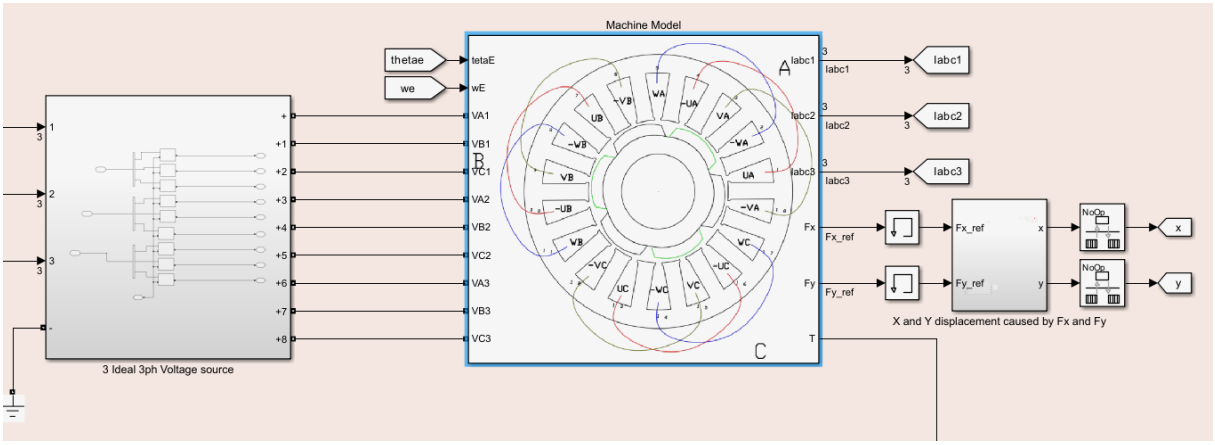

Figure 5.4: Ideal inverter (left)), machine block (centre) and mechanical simulation block (righ).

Those matrices take eccentricity into account, having been mapped for a certain set of eccentricity radii and angles. A linear interpolation is performed through a function block on r_ϵ and θ_ϵ to be able to compute fluxes amplitude and phase for any rotor position with higher resolution, and finally reconstruct no-load fluxes through Fourier. The aforementioned code also inverts the machine equations to obtain the actual current derivatives $\frac{di}{dt}$, and a subsequent integration block allows to compute the real phase currents 5.5.

$$\frac{d\bar{i}}{dt} = [L]^{-1}(\overline{V} - R_s\bar{i} - \bar{e}) \tag{5.10}$$

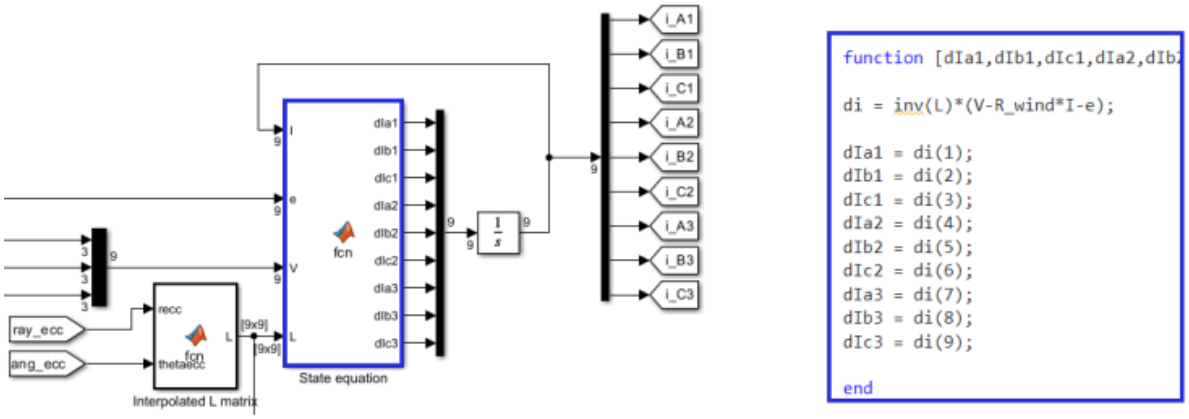

Figure 5.5: Machine equations implementation in Simulink.

Finally, the system in Figure 5.6 computes the dynamics of the rotor to calculate the radial displacement due to the eccentricity. The inputs are the radial forces references and the negative stiffness contribution, while the acceleration is computed considering the rotor as a mass in which radial force and elastic force (due to stiffness) act on the same direction.

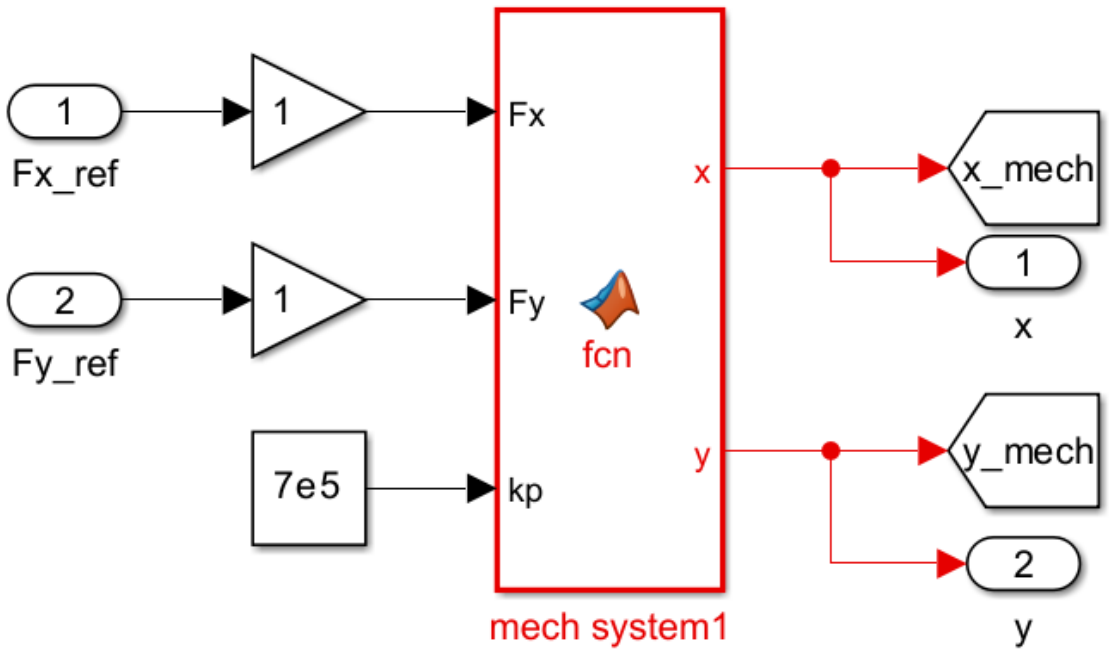

Figure 5.6: Mechanical model.

The *abc* currents and the $x - y$ rotor position compose the feedback loop of the control system: as it was explained above, both those quantities are obtained directly from the data provided by the LUTs, to furthermore highlight the importance of the results of this

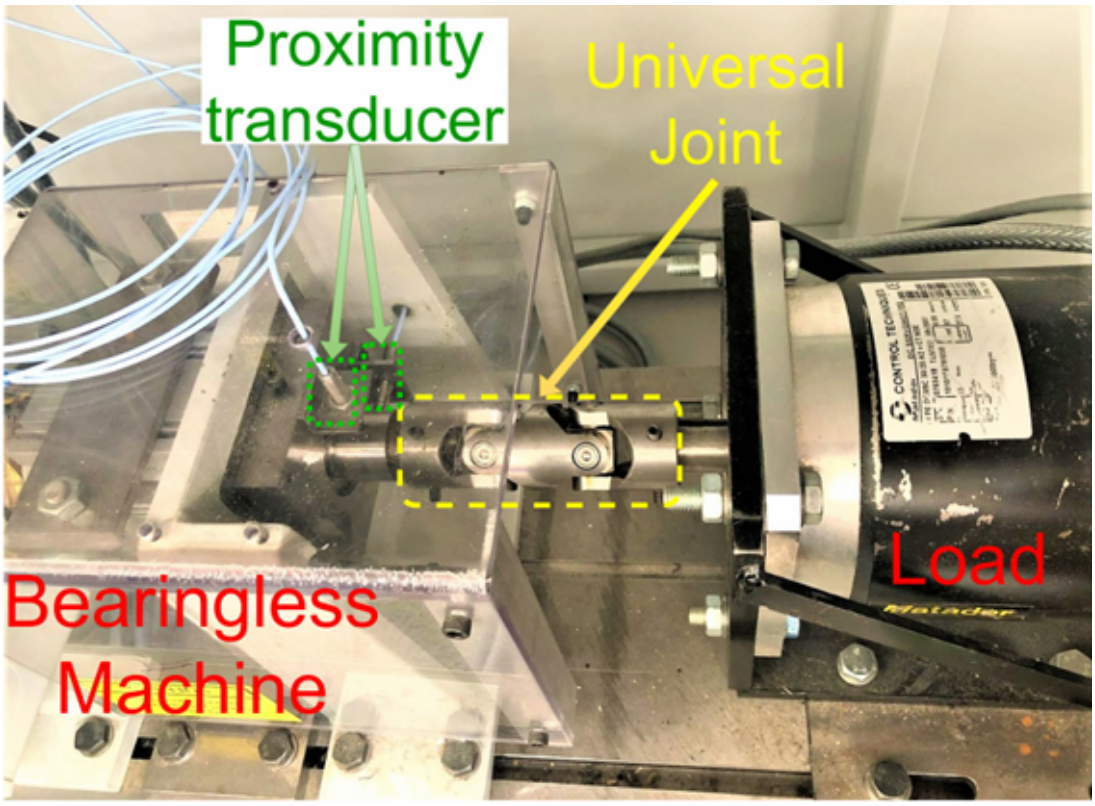

Figure 5.7: Real test bench setup [5].

work. In a real setup, since the accurate position detection is of fundamental importance for the development of a bearingless machine, the radial position control loop relies on expensive proximity sensors for the feedback signal: in Figure 5.8, eddy currents-based proximity sensors from Bently Nevada are employed, and can be distinguished in the test bench in Figure 5.9, showing the test setup created at the PEMC group facilities in Nottingham, on the right side of the table for their blue color.

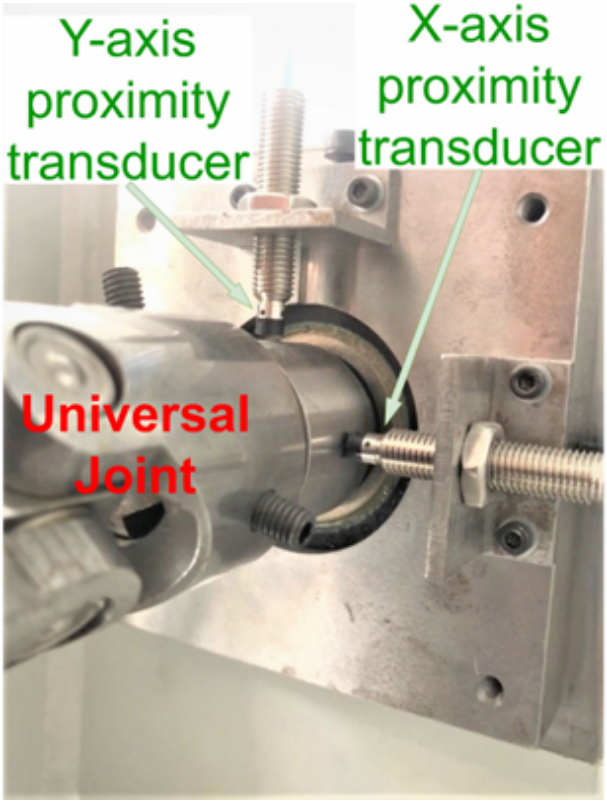

Figure 5.8: x-y proximity transducers in the real test bench [5].

The limited range of motion available for the motor shaft is shown in Figure 5.8, while the complete test bench is reported in Figure 5.9, where the main components are highlighted: the three 3-phase inverters and the DC servo drive are controlled by the control board located on the table, beneath which the multiphase bearingless machine and the DC motor used for imposed-speed testing can be seen.

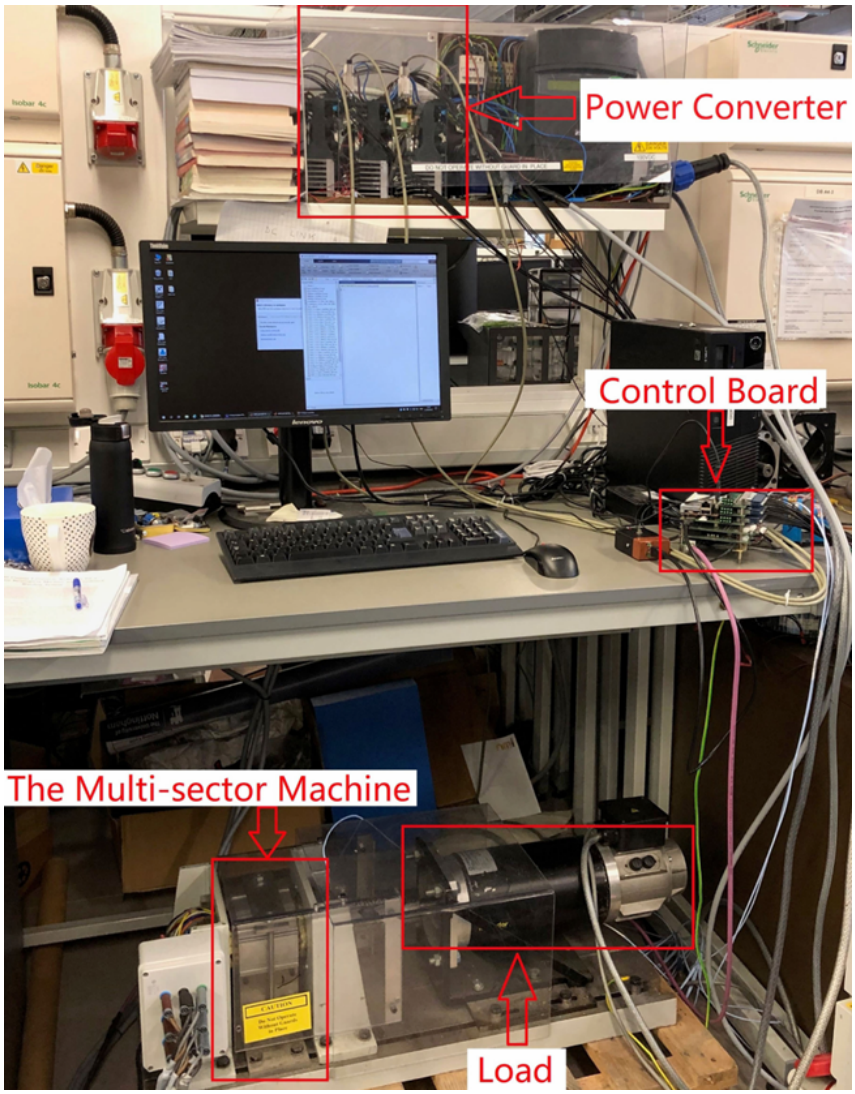

Figure 5.9: Testing setup in the PEMC facilities in Nottingham [9].

Chapter 6

Conclusions and future developments

This thesis investigated the electromagnetic behavior of a multi-sector bearingless surface-mounted permanent magnet (SPM) machine, with particular attention to the impact of rotor eccentricity on its performance. Bearingless machines are increasingly being considered in advanced applications—such as automotive, aerospace, and high-speed industrial systems—where improved dynamic behavior, compactness, and reduced mechanical wear are essential. Nevertheless, most of the conventional modeling and control strategies typically assume a perfectly centered rotor, neglecting the eccentricity-induced variations in inductance values, torque production, and radial force generation.

To address this gap, the work first described a comprehensive finite-element electromagnetic model of the machine, capable of describing both centered and eccentric operating conditions, in chapter 2. The differences between these conditions in terms of flux, torque, and radial forces, which often cannot be neglected when designing robust control strategies, are reported and commented.

The author's major contribution of this thesis lies in Chapter 3, where several mapping techniques were proposed and compared with the aim of reducing the computational effort, traditionally associated with FE–based electromagnetic characterization. Indeed, standard FEA mapping often requires a significant amount of computational time for high-resolution multidimensional maps, especially when the model variables increase once including eccentricity as an additional degree of freedom. The strategies developed in this work focus on preserving the accuracy of the electromagnetic representation while drastically reducing the number of FEA simulations required. In fact, a significant effort was devoted on proposing the accuracy comparison between the newly proposed characterization strategies with respect to the original method.

The results presented in Chapter 4 highlighted the substantial savings in computational duty and, ultimately, simulation time. These findings confirm the feasibility of producing reliable inductance and wrench maps through optimized sampling approaches.
The adopted strategies were formulated in the most generalized manner possible, with the aim of enabling their application to multiple machine geometries and winding distributions,

with the goal of broadening their relevance to future research and industrial contexts. This work also aims at enabling faster design iterations and facilitating the exploration of alternative machine configurations, without the prohibitive cost of repeated full-resolution mappings.

Finally, Chapter 5 presented the implementation of the resulting lookup tables (LUTs) within a Simulink control environment. This integration aims at showing the practical value of the mapping approaches: the machine model can be simulated in closed-loop control with high fidelity and drastically reduced computational load. Such an environment is essential for rapid prototyping of advanced control algorithms. This work also aims at laying the groundwork for future development of sensorless control techniques, not only for rotor angular position estimation but also for the estimation of eccentric rotor displacement in the x-y plane: the availability of accurate LUTs that account for eccentric conditions is a key enabling factor for such strategies.

In summary, the thesis achieved its overarching objective: providing a computationally efficient workflow to simulate and analyze a bearingless SPM machine while accounting for the effects of rotor eccentricity. The proposed methodology enables rapid generation of machine maps suitable for advanced control schemes, significantly shortening the design cycle and supporting future research on sensorless and fault-tolerant operations. Considering the state of the research work, instead, possible improvements can be obtained by optimizing the model mesh, as well as investigating on the nature of the numerical error leading to non-zero radial forces when the rotor is in a centered position and none of the machine phases is being powered.

Bibliography

[1] S.-I. Hwang and J.-M. Kim, "Opposite triangle carrier with svpwm for common-mode voltage reduction in dual three phase motor drives," *Energies*, vol. 14, no. 2, p. 282, 2021.

[2] R. Pérez, J. Cros, and M. Picard, "Real-time modeling of static, dynamic and mixed eccentricity in permanent magnet synchronous machines," *Machines*, vol. 13, no. 2, p. 120, 2025.

[3] H. Cui and X. Ding, "Suspension force model of bearingless multi-sector surface-mounted permanent magnet synchronous motor based on maxwell stress tensor method," in *2023 26th International Conference on Electrical Machines and Systems (ICEMS)*. IEEE, 2023, pp. 3163–3168.

[4] N. P. Petersen and E. L. Severson, "Rotor eccentricity impact on electromagnetic behavior in combined winding bearingless motors towards displacement self-sensing," *IEEE Transactions on Energy Conversion*, vol. 40, no. 1, pp. 323–336, 2024.

[5] Z. Wen, M. Di Nardo, G. Sala, G. Valente, A. Marfoli, M. Degano, P. Zanchetta, and C. Gerada, "Modular power sharing control for bearingless multithree phase permanent magnet synchronous machine," *IEEE Transactions on Industrial Electronics*, vol. 69, no. 7, pp. 6600–6610, 2021.

[6] G. Sala, G. Valente, M. Di Nardo, M. Degano, P. Zanchetta, and C. Gerada, "Power-sharing control in bearingless multi-sector and multi-three-phase permanent magnet machines," *IEEE Transactions on Industrial Electronics*, vol. 68, no. 10, pp. 9070–9080, 2020.

[7] M. Di Nardo, M. R. Ilkhani, M. Wang, M. Degano, C. Gerada, G. Sala, T. Spadi, M. Gaertner, C. Brecher, and M. Hoppert, "Rotor vibration control using multi-three-phase permanent magnet synchronous machines," in *2023 IEEE International Electric Machines & Drives Conference (IEMDC)*, 2023, pp. 1–7. [Online]. Available: https://amslaurea.unibo.it/id/eprint/28263/

[8] M. Di Nardo, M. Ilkhani, M. Wang, M. Degano, C. Gerada, G. Gallicchio, F. Cupertino, M. Gartner, C. Brecher, and M. Hoppert, "Optimal design of bearingless multi-three

phases permanent magnet synchronous machines," in *2023 IEEE International Electric Machines & Drives Conference (IEMDC)*. IEEE, 2023, pp. 1–7.

[9] Z. Wen, G. Valente, A. Formentini, L. Papini, C. Gerada, and P. Zanchetta, "A novel current limitation technique exploiting the maximum capability of power electronic inverter and bearingless machine," *IEEE Transactions on Industry Applications*, vol. 57, no. 6, pp. 7012–7023, 2021.

[10] G. Valente, "Radial force control of bearingless multi-sector permanent magnet machines," Ph.D. dissertation, University of Nottingham, 2018.

[11] G. Sala, "Multiphase electric drives for" more electric aircraft" applications," 2018.

[12] A. Marfoli, M. Di Nardo, S. Garvey, M. Degano, R. Vashisht, R. Turnbull, and C. Gerada, "Modelling, analysis and design considerations of multi-phase bearingless permanent magnet synchronous machine," in *2021 IEEE Energy Conversion Congress and Exposition (ECCE)*. IEEE, 2021, pp. 4646–4653.

[13] K. Miyashita, M. Ooshima, and M. N. Uddin, "Design of a time-divided torque and suspension force control type bearingless motor," in *2011 IEEE Power and Energy Society General Meeting*. IEEE, 2011, pp. 1–4.

[14] M. Ooshima, T. Karasawa, and M. N. Uddin, "Stabilized control strategy under loaded conditions in a bearingless motor based on dq axis current control," in *2013 IEEE Industry Applications Society Annual Meeting*. IEEE, 2013, pp. 1–7.

[15] G. Valente, L. Papini, A. Formentini, C. Gerada, and P. Zanchetta, "Radial force control of multisector permanent-magnet machines for vibration suppression," *IEEE Transactions on Industrial Electronics*, vol. 65, no. 7, pp. 5395–5405, 2017.

[16] G. Sala, G. Valente, A. Formentini, L. Papini, D. Gerada, P. Zanchetta, A. Tani, and C. Gerada, "Space vectors and pseudoinverse matrix methods for the radial force control in bearingless multisector permanent magnet machines," *IEEE Transactions on Industrial Electronics*, vol. 65, no. 9, pp. 6912–6922, 2018.

[17] D. Meeker, *FEMM: Finite Element Method Magnetics User Manual*, FEMM Project, 2022, available at http://www.femm.info.

[18] T. Spadi, "Modelling and analysis of multi-three-phase drives for radial force control."

[19] K. Imai, G. Valente, and D. Gerada, "Initial position estimation method based on inductance spatial harmonic components for triple three-phase surface-mounted permanent magnet synchronous motor," in *IECON 2020 The 46th Annual Conference of the IEEE Industrial Electronics Society*. IEEE, 2020, pp. 4845–4850.